Hydro-morphological behaviour around erosion protective structure with downward seepage

A Thesis Submitted

In partial fulfilment of the requirement for the degree of

Doctor of Philosophy

Submitted By

Harish Kumar Patel

(206104008)

DEPARTMENT OF CIVIL ENGINEERING

INDIAN INSTITUTE OF TECHNOLOGY GUWAHATI

GUWAHATI – 781039, INDIA

September 2024

Dedicated to

my Family

DECLARATION

I, Harish Kumar Patel, declare that this thesis titled, "Hydro-morphological behaviour around erosion protective structure with downward seepage" is part of my research for the degree of Doctor of Philosophy. All the work presented in this thesis is my own, and the results generated are of the original research.

I confirm that

- The work contained in this thesis is original and was done wholly or mainly while in candidature for the research degree at this institute under the guidance of my supervisor.
- The work reported herein has not been submitted to any other Institute for any degree or diploma.
- Wherever I reported material from other sources, I have duly cited and acknowledged their respective authors and sources.
- I also affirm that no part of the thesis is plagiarised to the best of my knowledge.
- I take complete responsibility for the results and inferences reported in the thesis.

Date: Harish Kumar Patel

Department of Civil Engineering

Indian Institute of Technology Guwahati

Guwahati – 781039, Assam, India

Dr. Bimlesh Kumar

Professor

bimk@iitg.ac.in

0361-258 2420

CERTIFICATE

This is to certify that the thesis entitled "Hydro-morphological behaviour around erosion protective structure with downward seepage", submitted by Harish Kumar Patel, in partial fulfilment of the requirements for the award of the degree of Doctor of Philosophy to the Indian Institute of Technology Guwahati, is a record of bonafide research work under my supervision. I certify that this thesis is worthy of consideration for the award of the degree of Doctor of Philosophy of the Institute. To the best of my knowledge, no part of the work reported in this thesis has been presented for the award of any degree at any other institution.

Date:

Place: IIT Guwahati

24/04/25

(Dr. Bimlesh Kumar)

PUBLICATIONS

JOURNALS

1. Patel, H.K., Arora, S., Lade, A.D., & Kumar, B. (2022). Flow behavior concerning bank stability in the presence of spur dike- A review. Journal of water supply, 23(1), 237-258. https://doi.org/10.2166/ws.2022.418
2. Chakravarty, S., Patel, H.K., Mohanty, B., & Kumar, B. (2023). Review on different shapes of spurs and their effects on channel morphology. Water Practice & Technology, 19(1), 241-262. doi.org/10.2166/wpt.2023.221
3. Patel, H. K., & Kumar, B. (2023). Hydro-morphological behavior around T-shaped spur dikes with downward seepage. Scientific Reports, 13(1), 10454. https://doi.org/10.1038/s41598-023-37694-w
4. Patel, H. K., Arora, S., Chavan, R., & Kumar, B. (2024). Migrating Scour Depth around a Spur Dike with Downward Seepage Using Multiscale Characterizations. Experimental Thermal and Fluid Science, 151, 111071. doi.org/10.1016/j.expthermflusci.2023.111071
5. Patel, H. K., Qi, M., & Kumar, B. (2023). Downward seepage effects on flow near a L-shape spur dike and bed morphology. International Journal of Sediment Research, 39(2), 194-208. doi.org/10.1016/j.ijsrc.2023.11.005
6. Patel, H. K., & Kumar, B. (2023). Experimental Study on the Optimal Spur Dike Shape under Downward Seepage. Water Science, 38(1), 172-191. doi.org/10.1080/23570008.2024.2321423
7. Patel, H.K., & Kumar, B. (2024). Optimal Spur Dike Orientation for Scour Mitigation under Downward Seepage Conditions. Journal of Hydrology and Hydromechanics, 72(2), doi.org/10.2478/johh-2024-0019

8. Patel, H.K., & Kumar, B. (2024). Channel Morphology with Permeable Spur Dike under Downward Seepage. (Under review)

CONFERENCES

1. Patel, H.K., & Kumar, B. (2022). Effect of seepage on alluvial channel's morphology. Research and Innovations for Sustainable Development Goals. NERC Springer Conference. Doi: 10.1007/978-981-97-5870-8
2. Patel, H.K., Shah, C., Kenglang, J & Kumar, B. (2023). Evolution of scour depth around oriented spur dikes, Research and Industrial Conclave-Integration'23, IIT, Guwahati (Poster Presentation)
3. Patel, H.K., & Kumar, B. (2023). Optimizing Spur Dike Orientation for Scour Control in Downward Seepage Scenarios. EGU 24, Vienna, Austria 14–19 April 2024. https://doi.org/10.5194/egusphere-egu24-2704 (Online Poster Presentation)

ACKNOWLEDGEMENTS

The journey of completing my Doctoral Dissertation has been a bitter sweet experience, with lots of highs and lows. It would have been impossible without the support and guidance of several people. They gave me the motivation I needed to keep going, and without their support, I would not have succeeded.

First of all, I am highly indebted to my supervisor, Prof. Bimlesh Kumar, for his guidance and supervision in completing my research work. During my PhD, he gave me the freedom to work and engaged me in new ideas. His unconditional support and motivation gave me strength and lifted my spirit whenever I got stuck. And thus, I am looking forward to work with him in the future.

I would also like to thank members of my doctoral committee; Prof. Ajay Kalamdhad (chairman), Prof. Sisir K Nayak and Dr. Rishikesh Bharti for their insightful comments, encouragement, and valuable time throughout the research. I would like to acknowledge the Department of Civil Engineering at IIT Guwahati for providing me with the required resources and a fruitful work environment.

I would like to express my sincere gratitude to Dr Mahesh Patel, Dr Rutuja Chavan, Dr Abhijit Lade, and Dr Jyotirmoy Barman for their valuable input on various complex topics. I will always cherish the time I spent in the laboratory with Dr. Jyotirmoy Barman, Sukhjeet Arora, Waseem Ghani, and Shovit Kumar during my PhD days. I would also like to thank Kumar Chandramauli Shah, Joychen Kenglang, Mrinal Roy, Pradumna and Bazal Da (Bazal Hoque) who generously gave their time to assist me in my experiments.

A special thanks to Sukhjeet Arora for his support throughout my PhD journey, including experimental work, analysis and article revision. I sincerely appreciate his tremendous assistance, which was made possible by his impulsive and consistent support.

I owe a debt of gratitude to my parents, my mother, my father and my entire family; their love and support made this journey possible. I want to give special thanks to my wife, Sonam Patel, and my daughter, Siyaa, for their unwavering love, support, and sacrifices during my PhD. I am grateful for the selfless support from my extended family and all those who, directly or indirectly, helped me complete this journey.

My 4-year PhD journey wouldn't have been possible without the support of my friends, who stood by me through the highs and lows. I am grateful to Dr Uttam Puri Goswami, Dr Bhagwan Das Mehra, Dr Shailendra Kumre, Prashant Kori, and Prabhat Kewat for their motivation and support during challenging times. I also want to thank my school, BTech, and MTech friends for their help and encouragement.

Finally, I bow my head to the Supreme Lord in deepest gratitude and seek blessings.

ABSTRACT

River bank protection is crucial in hydraulic river engineering to safeguard natural rivers, lands, and critical structures like bridges. Spur dikes, aimed at diverting flow from the bank and decreasing velocity, are effective in preventing erosion. Achieving stable river banks and sustainable foundations necessitates an in-depth understanding of scour processes, precise scour depth assessment, and meticulous planning for spur dike installation. This study aimed to optimize spur dike shapes (T-shape, L-shape, and rectangular) for managing flow turbulence and reducing local scour, considering the effect of downward seepage. Results showed that T-shaped dikes had the lowest scour depths, both with and without seepage. Without seepage, L-shaped dikes had the greatest scour depth, but with seepage, rectangular dikes had the deepest scour. Maximum velocity was observed near the water surface around rectangular dikes, and this increased with seepage. T-shaped dikes, in contrast, exhibited weaker velocities. The negative impact on velocity and RSS magnitude was observed at the near channels bed at maximum scour depth and was linked to flow reversal, horseshoe vortices, and particle detachment, which was accelerated by downward seepage, deepening scour depressions.

The current work also uses an experimental method to analyse a multiscale statistical assessment of scour depth surrounding the T-shape spur dikes with downward seepage. Results indicated that the celerity of scour depth for both time and length scales depends on the downward seepage. Initially, the scour develops at a higher rate, but over time, this rate decreases until it becomes constant.

The study also examined the effects of different combinations of permeable and impermeable T-shaped spur dikes (Sets A, B, and C) on bed morphology and scour progression under downward seepage. Set-A (0%, 0%, 0%) consisted of three impermeable spur dikes (where 0% permeability provided) arranged in series, while Set-B (60%, 0%, 0%) included a 60%

permeable first spur dike with the other two remaining impermeable. In Set-C (60%, 30%, 0%), Spur-1 was 60% permeable, Spur-2 was 30% permeable, and Spur-3 remained impermeable. Results showed that permeable Sets B and C significantly reduced maximum scour depth at the initial spur dike without seepage by 37.6% and 55.2%, respectively, compared to impermeable Set-A. This reduction trend continued under seepage conditions, V_{S1} and V_{S2}. Set-B reduced scour depth by 38.5% (V_{S1}) and 35.3% (V_{S2}), while Set-C achieved reductions of 42.4% (V_{S1}) and 47.4% (V_{S2}). Set-C was the most effective at reducing scour, while Set-A produced the deepest scour. Downward seepage increased sediment particle movement, leading to deeper scour formations beginning at the spur dike tip.

The experimental study also investigates how different orientations of spur dikes (60º, 90º, and 120º) affect bed morphology and scour development over time. It compares maximum scour depths with and without downward seepage. Results indicate that a 90º orientation produces the deepest scour, while 120º results in the least. Downward seepage exacerbates sediment motion, leading to increased particle detachment and deeper scour depressions.

Keywords: Downward seepage; Spur dike shapes; Celerity; Permeability; Orientation; Scour depth

CONTENTS

LIST OF FIGURES

LIST OF TABLES

NOTATIONS

ADV	Acoustic Doppler Velocimeter
B	Free surface width of the flow
BSS	Bed shear stress
C_d	Coefficient of discharge
CFD	Computational fluid dynamics
D_{50}	Median grain diameter
DES	Detached eddy simulation
EDM	Electronic Distance Meter
EVM	Electromagnetic velocity meter
Fr	Froude number
g	acceleration due to gravity
G_s	Specific gravity
h/y	mean depth of flow
h_S	Spur dike height
H	water head over the notch
k	turbulent kinetic energy
L	Length of the spur dike (Projected)
L'	Length of the spur dike wing
LES	Large-eddy simulation
L_n	Width of the notch
PIV	Particle image velocimetry
P	production (turbulent kinetic energy)
$\bar{p}$	mean total dynamic pressure
Q	Flow discharge
q_s	seepage discharge
Re	Reynolds number
RSS	Reynold's Shear Stress
S	magnitude of the vorticity

S_o	Channel bed slope
ΔS	Spacing between spur dikes
TKE	Turbulent kinetic energy
TI	Turbulent Intensity
U	Average velocity in the channel
URS	Ultrasonic Ranging System
$\bar{u}_i$	mean velocity
u_i'	fluctuation of turbulent velocity
u_{*c}	critical shear velocity
u, v, w	Instantaneous velocities in streamwise (X), transverse (Y), and vertical (Z) directions.
u', v', w'	Instantaneous fluctuations in streamwise (X), transverse (Y), and vertical (Z) directions.
$\overline{u}, \overline{v}, \overline{w}$	Average velocities in streamwise (X), transverse (Y), and vertical (Z) directions.
$\sqrt{\overline{u'u'}}$	Turbulence intensity in streamwise direction
V_{S1}, V_{S2}	Seepage velocities at lower and higher rates respectively
$\sqrt{\overline{v'v'}}$	Turbulence intensity in transverse direction
$\sqrt{\overline{w'w'}}$	Turbulence intensity in transverse direction
z	Vertical distance from the bed surface
$-\rho\overline{u'w'}$	Reynolds shear stress in streamwise direction
$-\rho\overline{u'v'}$	Reynolds shear stress in transverse direction
ε	rate of dissipation of turbulent kinetic energy
μ_0	viscosity of fluid
μ_t	turbulence viscosity
ν	Kinematic viscosity
ρ	density of water
σ_g	standard deviations

τ_c	critical bed shear stress
v_t	turbulent eddy viscosity $\left(C_\mu k^2/\varepsilon\right)$
Ω_{ij}	distribution of stresses due to rotation.
θ	Orientation of spur dike
θ_b	Bank angle
θ_r	Angle of repose

1 Introduction[1,2]

1.1 Overview

Rivers flow through various landform terrains, starting from the rocky, boulder, and alluvial stage to the delta stage. In the rocky and boulder stage, rivers flow through boulders and rocks, which are difficult to displace. However, in the alluvial stage, the river encounters various sediment particles ranging from coarse sand to clay and silt. These particles in the alluvial stage are susceptible to erosion and are transported downstream by the river flow, contributing to further erosion. The removal of bank soil particles by flow velocity generates shear in the bank, one of the primary mechanisms causing riverbank erosion (Gholami & Khaleghi, 2013).

Riverbank erosion is one of the most common causes of bank instability. While bank erosion increases the width of the channel, deposition decreases it. However, these processes do not occur simultaneously, causing the river width to constantly fluctuate. Various stream structures, such as levees, guide banks, and spur dikes, are constructed to maintain the channel's width and protect the riverbank from erosion. The preference for one structure over another depends on the specific conditions at the construction site. Each structure has its advantages and disadvantages, typically governed by factors such as bank condition, soil type, bank slope, and channel curvature. When compared to other riverbank erosion prevention techniques, spur dikes provide one of the best solutions (El-Rashedy et al., 2018).

---

[1] Patel, H.K., Arora, S., Lade, A.D., & Kumar, B. (2022). Flow behavior concerning bank stability in the presence of spur dike- A review. Journal of water supply, 23(1), 237-258. https://doi.org/10.2166/ws.2022.418

[2] Chakravarty, S., Patel, H.K., Mohanty, B., & Kumar, B. (2023). Review on different shapes of spurs and their effects on channel morphology. Water Practice & Technology, 19(1), 241-262. doi.org/10.2166/wpt.2023.221

A spur, spur dike, or groyne is a river training structure built on a riverbank at some angle, as shown in Figure 1.1. Spurs are typically designed to divert the flow away from the channel bank and protect it by controlling velocity and directing the flow toward the center of the channel. The primary purpose of spur dikes is to provide bank protection and guide river flow. Spur dikes also improve the hydraulic habitat, mainly when constructed with a barrage (Yang et al., 2022b).

Figure 1.1 Spur dike protects a bend in the Gamka River at Calitzdorp, South Africa (King, 2009)

Several researchers (van Balen et al., 2010; Blanckaert et al., 2012; Engel & Rhoads, 2017; Kumar Das et al., 2020) used an acoustic Doppler current profiler to investigate the impact of Reynolds stress at the outer bank zone. According to the findings, alterations in flow patterns, bed shear stress, sediment entrainment patterns, and the increased velocity gradient enhance the rate of bank erosion, leading to river bank collapse and land loss (Darby & Thorne, 1996; Chu-Agor et al., 2009). Recent studies suggest that fluctuating streamwise and transverse velocity components significantly impact the river bank in terms of sediment entrainment (Roy et al., 2019; Kumar Das et al., 2020). Furthermore, Barman et al. (2019) observed that significant momentum flux and coherent structures play an essential role in bank instability. King (2009) conducted field studies to illustrate the influence of spur presence in preventing

bank erosion. The analysis involved monitoring the downstream channel where the spur dike was located.

Figure 1.2 shows the results before, during, and after the floods in the Buffeljags River, South Africa. The presence of spurs along the bank effectively prevented further riverbank erosion during the 2008 flood.

Figure 1.2 Photos captured downstream of the spur dike before, during, and after the floods in 2008, showing the minimal damage caused by the flood (King, 2009).

Understanding the causes of riverbank erosion is essential for its prevention. Researchers have found that flow turbulence is the primary cause of bank erosion and sediment transport. The stability of the bed and banks is significantly influenced by turbulent flow factors, including the three-dimensional distribution of velocity, turbulent kinetic energy, Reynolds shear stress, turbulence intensity, and bed shear stress.

Turbulence significantly enhances sediment transport around structures, potentially leading to structural failure. To ensure structural safety and prevent bank erosion, it is imperative to study turbulent flow behavior around these structures. This study provides a comprehensive review of studies on several aspects associated with spur dikes and knowledge development.

The present study critically reviews the current state of research on how turbulent characteristics influence the bed and bank stability of spur dikes. Based on current knowledge, we identify and discuss key research areas that remain underexplored, such as the effects of seepage and vegetation within the channel.

1.1.1 Classification of spur dikes

Spur dikes can be classified based on:

- construction methods;
- submergence condition;
- geometry;
- interaction with the flow field.

Based on permeability, there are two types of spur dikes: permeable and impermeable spur dikes. Permeable spur dikes are often constructed using one or more rows of steel, bamboo, timber, or RCC piles. Permeable spur dikes are typically used as temporary structures and are more cost-effective. Impermeable spur dikes are generally built of readily available materials such as stones, gravel, rocks, and local materials. An impermeable spur dike typically restricts and diverts incoming flow. In contrast, a permeable spur dike allows flow to pass through at a reduced velocity (Shampa et al., 2020; Iqbal et al., 2021; Mirzaei et al., 2021; Tripathi & Pandey, 2021, 2022).

A submerged spur dike is fully immersed in water, whereas non-submerged spur dikes are partially submerged in water. Based on head shape, spur dikes can be classified into categories

such as straight, L-shaped (with the head-turning downstream parallel to the flow), T-shaped, hammer-head (with the head-turning both upstream and downstream), hockey, and molehead spur dikes.

Based on the alignment, spur dikes are categorized into three types: attracting, deflecting, and repelling spur dikes. An attracting spur dike inclines towards the downstream with the bank and tends to attract the flow toward the bank, but a repelling spur dike tilts the flow in the upstream direction itself, causing the flow to divert away from the bank. A deflecting spur dike or transverse dike is fixed perpendicular, extending from the bank into the river to deflect the current away from the bank as shown in Figure 1.3.

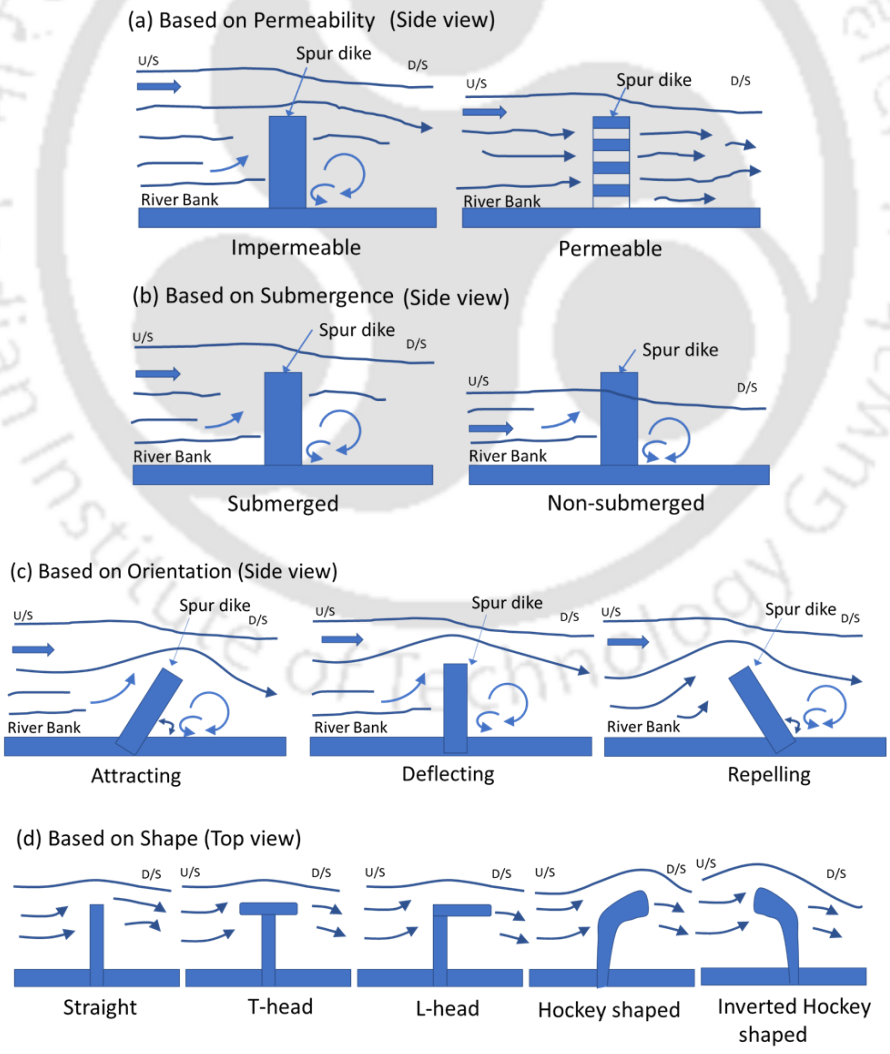

Figure 1.3 Classification of spur dikes (Zhang & Nakagawa, 2008).

1.1.2. General guidelines for spur design and Recommendations

Key elements frequently considered when designing spur dikes include plan view shape, length, spacing between adjacent spur dikes, orientation, channel cross-section, crest height, construction materials, and riprap size (Richardson et al., 1975; Brown, 1985; Yossef, 2002), as illustrated in **Figure 1.4.** Although design methods for spur dikes may vary, they all share the common goal of providing bank protection at specific channel sections. The most critical design characteristics are discussed below.

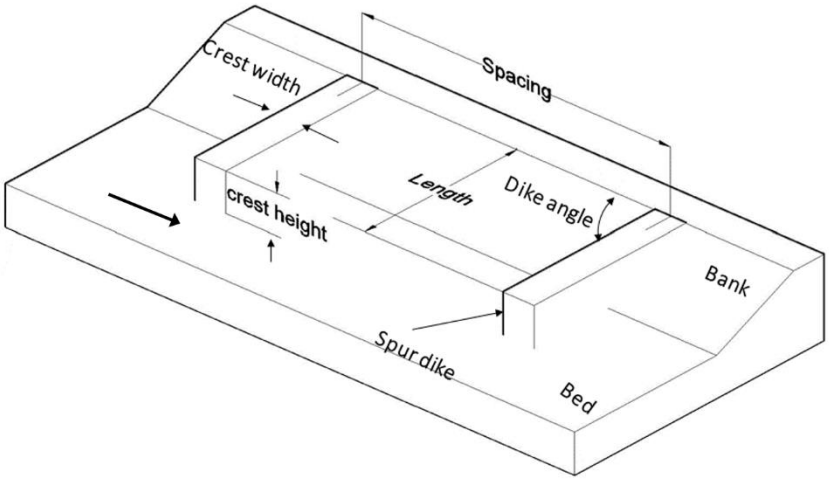

Figure 1.4 Schematic representation of a spur dike configuration displaying significant design criteria (USACE, 1980)

1.1.2.1 Plan view shape- Spur dikes can be constructed in various plan view shapes. Examples include straight (rectangular), hockey stick or curved, inverted hockey stick, L-head, straight with pier head, and T-head spur dikes. Among the various shapes, the rectangular spur dike is one of the most cost-effective designs. It has received significant attention from researchers due to its ease of installation in both field and laboratory. Consequently, researchers predominantly use rectangular spur dikes (summarized in Table 1.1) to study flow characteristics around them. Although other spur shapes have been explored, their implementation remains limited. Kuhnle et al. (2008) used a trapezoidal spur dike to observe flow velocities in a laboratory flume around a submerged structure. Hashemi et al. (2008)

confirmed that the scour depth around L-shaped spurs is less than that of other shapes. El-Rashedy et al. (2018) analyzed the effect of discharge and Froude number on the scouring process around the different shapes of spur dikes, such as straight, hockey, mole head, L-shape, and T-shape. Experiments suggest that a hockey-shaped spur dike is more effective at reducing scour depth. Kumar and Ojha (2019, 2021) investigated turbulent flow characteristics and equilibrium scour depths around an unsubmerged L-head spur dike using different structural compositions, groyne configurations, and constriction ratios. The flow patterns near in-stream rock structures were studied using single-arm rock vanes (at 20 and 30°), J-hook vane (at 30°), and bend way weirs (at 80 and 60°) with the help of large-eddy simulation along with the laboratory experiments (Kang et al., 2021a). Yu et al. (2020) analyzed the water surface profile and flow velocity around spur dikes of five distinct shapes, including trapezoidal section arc straight head, trapezoidal section arc hook head, trapezoid section fan straight head, trapezoidal section fan hook head, and arc section straight head. Recent studies suggest that T-shaped spur dikes have the least amount of scour among all geometric shapes (Vaghefi et al., 2012, 2015, 2016a, 2016b, 2018, 2019; Safarzadeh et al., 2016; Mehraein et al., 2017; Tripathi & Pandey, 2021). Furthermore, Bahrami-Yarahmadi et al. (2020) used a triangular spur dike to examine the scour pattern around it and suggested that it can reduce scouring at the tips.

1.1.2.2 Spur dike length- Spur dike length refers to the projection of the structure perpendicular to the streamflow direction. It is typically expressed as a percentage of the channel width at the bank-full stage. Literature suggests that the parameters for determining spur dike length are site-specific. For straight reaches, Alvarez (1989) proposed that the spur dike length should range between the mean depth (h) and 0.25 times the free surface width (B) of the flow. Richardson et al. (1975) recommended a minimum length of 15.24 m and a range of 10% to 15% of the bank-full channel width as the maximum length for straight reaches, large-radius bends, and braided channels. It has been observed that longer spur dikes are

associated with increased scour. Additionally, increasing the spur dike length shifts the maximum scour depth closer to the channel's outer wall (Vaghefi et al., 2009). Bed shear stress near the spur dike's tip increases significantly with longer spur dike lengths (Koken & Gogus, 2015).

1.1.2.3 Spur dikes spacing- Spur dikes are typically installed in series rather than as individual structures. When installed in series, the flow around spur dikes varies based on the spacing between them.

According to the literature, ideal spacing ratios (spacing of spurs/length of spur) range from 1 to 6, with less than 1 used for retardance spurs and 6 for impermeable diverter spurs. Several field experiments were conducted to study bank protection along the Sutlej River below the Panjnad Headwork. Experimental results indicate that an ideal spacing ratio of around 5 provides optimal bank protection. Ahmad (1951) found that when the spacing exceeds five, the bank between the spurs is vulnerable to erosion and degradation. Fenwick (1969) suggested that spur dike spacing be classified according to installation purpose, with spacing ratios of 2–2.5 for flow control and 3 for bank protection. Richardson et al. (1975) recommend spacing spur dikes 1.5 to 6 times their upstream projected length. An aspect ratio of 1.5–2.0 is recommended to maintain a distinct channel for navigation. For bank protection, a spacing ratio of 2–6 is typically used. Additionally, Garg et al. (1980) suggested that the spacing between multiple spurs should be determined by their angle and the flow curvature. Spurs are typically spaced 3–4 times their length apart.

For groyne installation and protection, considering transmissivity, angle, length, and channel curvature, Brown (1985) proposed an aspect ratio range of 1–6. Kim et al. (2014) proposed an installation spacing of 4 to 6 times the groyne length, accounting for reduced flow velocity and riverbed stability. Bahrami-Yarahmadi et al. (2020) used a triangular shape for their study.

They recommended that the spacing between them be restricted to 5.5 times the effective length of the structure. Hajibehzad et al. (2020) showed the maximum scour depth around the spur dikes as the distance between them increases. Hence, spur dike length and spacing between them are the significant design factors for bank protection.

1.1.2.4 Spur dike Orientation- Hydraulic structures like spur dikes or groynes extend from river or stream banks and are oriented either upstream, downstream, or perpendicular to the primary flow direction. The orientation of a spur dike affects flow patterns, scouring, and sedimentation processes near the structure. According to Richardson and Simons (1984), the recommended orientation for a spur dike ranges between 30° and 120° relative to the downstream direction. For navigation, downstream-inclined spur dikes are more effective as they create deeper flow conditions. Spur dikes with orientation angles exceeding 90° are particularly effective for bank protection. These spur dikes promote sediment deposition, enhancing bank stability (Brown, 1985; Kuhnle et al., 2002).

The United Nations (1953) guidelines recommend constructing spur dikes either perpendicular to the bank or inclined upstream. An upstream dike angle of 100–120° is suggested for optimal bank protection. Garde et al. (1961) proposed that the maximum scour depth occurs with spurs perpendicular to the bank, decreasing for other upstream or downstream orientations. Ezzeldin et al. (2007) noted that while spurs oriented at 135° produce wider scour holes, they also enhance aquatic habitats and reduce the risk of bank erosion. Krishna Prasad et al. (2016) recommended a 135° spur angle for effective erosion control and bank protection. Nath and Misra (2017) observed that as the spur dike's inclination decreases, the depth, length, and width of the scour hole also diminish.

1.1.2.5 Crest elevation - The crest elevation of spurs is determined by flow-induced alterations. Spurs can be designed to remain above water (non-submerged) or to be submerged during floods, emerging only after the floodwaters recede. For effective bank protection, the crest height of spurs should be at least equal to the bank height. Non-submerged spurs are typically impermeable, as submerged spurs may cause severe downstream erosion due to overtopping water. Conversely, submerged spurs are often permeable, allowing for smoother flow and reducing obstruction compared to solid spurs. Submerged spurs should ideally reach between one-third to half of the flow depth (Ji1a & Karmacharya, 2000).

1.1.2.6 Minimum number of spurs along the stream bank - The required number of spurs depends on the length of the stream bank needing protection and the spacing between spurs. Streamflow and bed scour patterns guide the selection of single or multiple spur dike arrangements for optimal bank protection and scour control. A minimum of three spurs is generally required for effective stream bank protection or flow contraction. For the protection of embankments across the stream, one or two spurs may be adequate (Richardson & Simons, 1984).

1.1.3 Flow pattern around spur dike

The flow can be divided into four zones as it passes through a spur dike. Fei-Yong and Ikeda (1997) classified the flow past a spur into four sub-zones: the main flow zone, shear layer, reattachment zone, and return flow zone. In contrast, Zhang and Nakagawa (2008) categorized the flow through a spur dike into three zones: the primary flow zone (main flow zone), extending from the spur dike's head to the opposite side of the channel; a wake zone behind the spur dike; and an intermediate mixing zone (Figure 1.5).

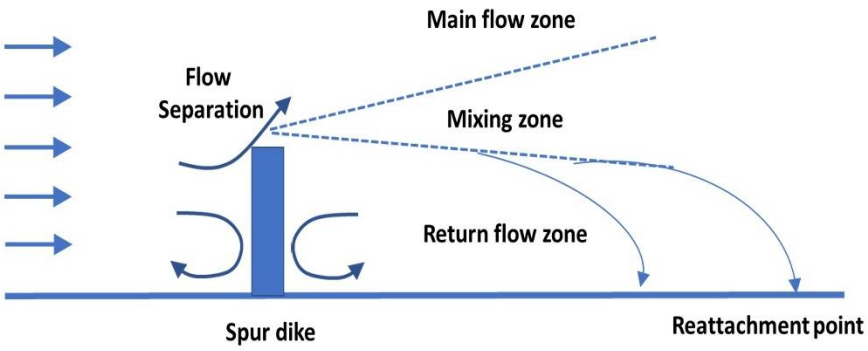

Figure 1.5 Typical flow around spur dike (Zhang & Nakagawa, 2008)

1.1.3.1 Main flow zone: In the main flow zone, the presence of a spur dike accelerates the flow. Molinas et al. (1998) observed that the velocity at the spur dike head can increase by up to 50% compared to the incoming flow velocity. Additionally, Ho et al. (2007) used experimental and computational methods to study flow around impermeable spur dikes, reaching similar conclusions.

1.1.3.2 Wake zone: The wake zone can be further divided into two sub-zones: return flow and reattachment.

***1.1.3.2.1 Return flow zone*:** Two eddies of different sizes and rotation directions typically form in the return flow zone. A small eddy forms near the spur dike, with its center located at a distance approximately equal to the length of the spur dike (L) downstream of the structure. Downstream of the small eddy, a larger eddy forms, with its center located approximately six times the spur dike's length downstream.

***1.1.3.2.2 Reattachment zone*:** The reattachment zone is located downstream of the spur dike, where the divided flow rejoins the channel bank. Fei-Yong and Ikeda (1997) proposed that the reattachment zone is located approximately six times the spur dike's length (L) downstream and extends between 11 and 17L. However, the reattachment zone is often simplified to a single point for easier analysis. The time-averaged velocity at this point is zero; however, it is

important to note that the instantaneous reattachment point varies. Ouillon and Dartus (1997) observed that the reattachment point for impermeable spur dikes occurred at 11.5L in experiments and 10.7L in numerical model analysis.

1.2 Scour around spur dike and their classification

The scouring in the vicinity of spur dike is usually categorised as:

(1) general scour;

(2) constriction scour; and

(3) local scour.

General scour occurs on the channel bed due to sediment movement, independent of the presence of a spur dike. The installation of the spur dike narrows the riverbed, resulting in constriction scour. The spur dike restricts flow and induces local scouring around the structure. The main function of a spur dike is to deflect the primary flow away from the bank. However, as with other hydraulic structures, the spur dike's performance is most threatened by excessive scouring. This scour, known as local scour, is often identified as a critical cause of structural failure. Accurate estimation of maximum local scour depth is crucial for the safe design of these structures.

Local scour is classified as either clear-water or live-bed scour, depending on the sediment transport mechanism of the incoming flow. Live-bed scour occurs when the mean flow velocity equals or exceeds the critical velocity. Conversely, when the mean velocity is less than the critical velocity, clear-water scour occurs. In general, clear-water scour may be divided into the following four stages: beginning, development, stabilization, and equilibrium stages. Scour develops rapidly during the initiation and development stages. The variation in scour depth is minimal during the stabilization stage. The equilibrium stage takes longer to reach than in live-bed scour. The onset of the equilibrium stage is marked by the scour depth stabilizing and

becoming nearly constant. In quantitative terms, the equilibrium stage in any morphodynamic process occurs when the slope of the scour depth vs. time plot (on a logarithmic scale) approaches zero (Ettema, 1980). In live-bed scour, the scour depth increases rapidly with time before fluctuating around a mean value due to the passage of bedforms. Figure 1.6 illustrates the temporal variation in maximum scour depth under live-bed and clear-water scour conditions.

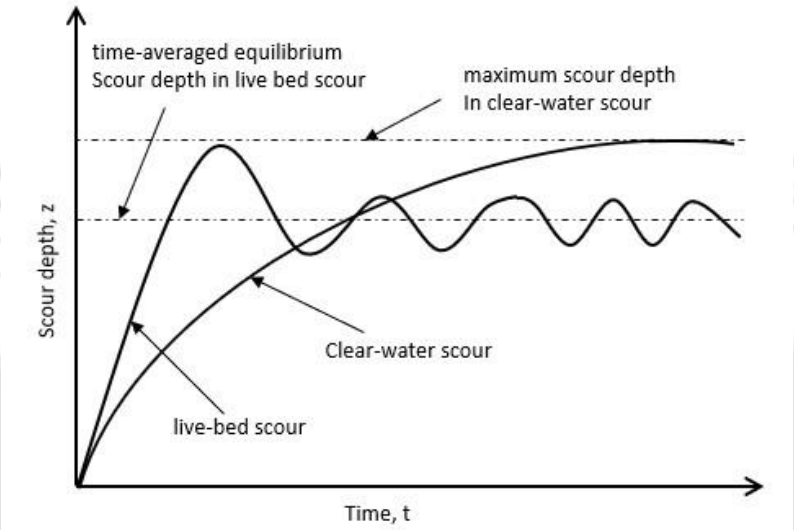

Figure 1.6 Scour Depth as a function of Time (Chabert, 1956)

1.2.1 Flow structure in the scour (local) area

Obstructions such as spur dikes or groynes significantly affect river flow patterns. These structures alter sediment transport, deposition, and both general and local scour near the spur dike. The presence of a spur dike or groyne generates a complex system of vortices. Vortices remove sediments from the base of the structure, driven by enhanced lateral flow passing through the obstruction. The eroded sediments are carried downstream by wake vortices, following the main flow direction, and eventually settle in aggrading sections of the river.

In front of the spur dike, the stagnation of incoming flow leads to the formation of bow waves at the water surface, with downflow occurring near the channel bed. Flow separation causes a

horseshoe vortex to form in the local scour hole, while a wake vortex system develops behind the spur dike. Figure 1.7 illustrates the generation of vortices around the spur dike in the local scour area.

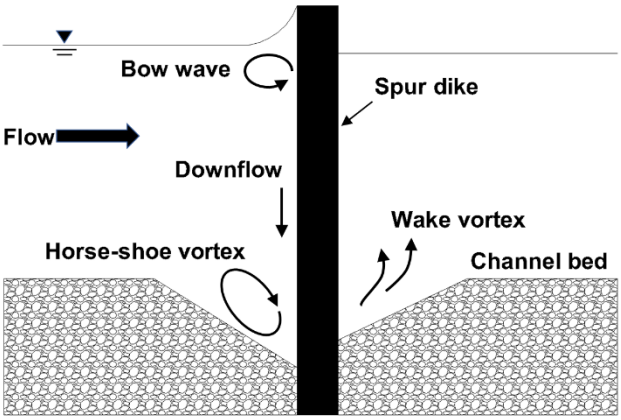

Figure 1.7 Flow pattern around a spur dike (Zhang & Nakagawa, 2008)

1.3 Effect on morphology due to spur installation

Flow characteristics within the channel significantly impact bed morphology. Installing a spur dike along the channel bank further increases flow complexity. The projection of a structure like a spur dike outward from the bank alters flow patterns and bed morphology. These changes typically initiate the scouring process. Studying morphology changes with and without a spur dike is essential to evaluating how erosion affects the channel bank and bed. Channel scouring impacts the strength of spur dikes and is a primary cause of their failure. The maximum expected scour depth must be accounted for in the structure's foundation design to prevent failure. Therefore, investigating the causes of scouring and methods for estimating the maximum scour depth around spur dikes are critical research challenges. Although several studies have been conducted, significant uncertainty remains in predicting scour depth. Scour at spurs is often predicted using either river-specific experience or case-specific physical models. Key factors influencing the scouring process include spur dike shape, projected and wing lengths, orientation, spacing between adjacent spur dikes, channel cross-section, crest

height, construction materials, permeability, and sediment and riprap sizes. Researchers have explored the influence of these factors both independently and in combination to determine which factors or combinations contribute most to the scouring process.

Ezzeldin et al. (2007) studied the local scour around a single straight impermeable submerged spur installed in a channel with different angles relative to the flow direction. Scour depth was found to be more due to greater resistance to the flow made by the spurs. Scour depth increases with an increase in the Froude number and the angle of inclination of the spur with respect to the flow direction. The maximum width of the scour hole was found at the orientation, with a spur angle of 135°.

Atarodi et al. (2021) performed experiments on spurs placed in a series and introduced a protective spur to reduce the scouring of the downstream spurs. The experiments investigated each spur's effect on other spurs of the series, highlighting the protective spur's influence in reducing the scour around other spurs. The introduced protective spur was shown to effectively decrease the scour around the spurs placed sequentially.

Vaghefi et al. (2009) investigated scouring near a T-shaped spur dike at a 90° bend channel. The different lengths of spur dike at various aspects of scour depth characteristics such as amount, volume, and dimensions were analyzed. It was found that these parameters increased as the length of spur dike from the bank increased. The maximum scour depth was obtained at the upstream side just near the spur dike.

Alauddin and Tsujimoto (2012) installed groynes in a series with different configurations. They conducted experiments to find which is more effective at high and low flow conditions. The results demonstrated that modified groynes are more effective than conventional ones for navigation channel maintenance at low-flow fields and bank protection at high-flow.

Vaghefi et al. (2012) experimentally investigated the scouring near the T-shaped spur dike at 90° bends. They studied two scour holes: one developed near the nose of the spur dike at the

upstream section, and the other developed at some distance from the spur at the downstream section. The scour volume upstream is much higher compared to downstream. Researchers also reported that the maximum scour depth increases as the spur dike length decreases (Ezzeldin et al. 2007).

Dawood (2013) conducted laboratory experiments with three different shapes of impermeable spurs in a straight channel: straight, T-head, and L-head. They observed an indirect relationship between the effect of spur numbers and the shape of spurs on the maximum scouring depth. In their experiments, the distance considered between the spurs was 1, 1.5, and 2 times the length of the spurs. The researcher reported an increase in scour depth by nearly 20% when the spurs' distance increased to 0.5 times the length of the spur.

Pandey (2014) reported that in the case of two subsequent groins in a rectangular straight channel, the maximum scour depth always developed at the upstream side of the first groin with its location near the nose of the groin on the upstream side. The scour hole size increases as the radius of the channel bend to channel width ratio increases (Mehraein & Ghodsian, 2017). The formation of scour around the spur dike projected at the bend is caused due to cross-current and vortices formed around the structure (Pandey et al., 2019). Scour patterns around triangular and rectangular spur dikes were compared at different hydraulic conditions. The result revealed that scour hole dimensions, such as maximum scour depth and volume, were smaller than rectangular spur dikes in triangular spur dikes (Bahrami-Yarahmadi et al., 2020). A study of the erosion and sedimentation patterns reveals that scour would occur at the tip and near the triangular and rectangular spur dike.

Akbari et al. (2021) studied the flow patterns around T-shaped spurs to determine the most effective geometric shapes. They found that the length of the spur dike web and its wing shape affected the flow characteristics. An increase in the web length and spur dike size can increase

the flow velocity by 77% at the bed, and 38% near the water surface, when the length of the spur installed is about 25% of the channel width.

Tripathi and Pandey (2021) examined the local scour and general scour in the vicinity of a T-shaped spur organized at different locations on the bank of a reverse meander channel. It was noticed that with an increase in the Froude number, the flow moves towards the spur dike to form a local scour and reduces the general scour in the vicinity of the spur dike while the depth of scour hole increases.

Pandey et al. (2021b) investigated temporal scour depth variation in the spur dike (vertical wall) to identify the most prominent parameters affecting the performance of the spur dike with non-uniform sediment. They proposed a new temporal scour depth equation for calculating maximum scour depth around spur dikes in the presence of non-uniform sediment. It was observed that the variation of temporal scour depth increases with an increase in parameters such as the threshold velocity ratio, Froude number, flow depth-particle size ratio, and flow shallowness and reduces as the non-uniformity of the sediment increases. Flume experiments conducted by Farshad et al. (2022) revealed significant attenuation to maximum scour depth in the case of permeable spur dike, as compared to the impermeable dike. Also, minimum bank retreat in a meandering channel was observed in the case of permeable spur dikes (Esmaeli et al., 2022). Similar observations were reported by Khajavi et al. (2022) and Hakim et al. (2022), wherein permeable spurs considerably eliminated the scour at bridge abutments in both steady and unsteady flow conditions.

Tripathi and Pandey (2022) reviewed previous research on flow patterns and prediction of temporal and maximum scour depth around spur dikes formed by straight, L-shaped, and T-shaped spurs placed at 90 and 180° curved channels. A detailed review of the numerical and experimental study suggests that the data and associated results are inadequate for the construction of spurs employed as river structures in curved channels.

The knowledge of how different shapes and orientations of spur dikes in the channel contribute to erosion processes was investigated to propose the most efficient and cost-effective spur dikes out of the numerous potential shapes. However, most researchers have not considered one of the primary factors present in the channel that impacts the bank and bed load transport process, even in the presence of spur dikes, which is seepage. In natural channels, along with the main flow, there is significant seepage flow from the channel bed and banks. The interaction of seepage will affect the flow structure, consequently affecting the scour patterns around the spur dikes. Future studies in this direction are needed for a more realistic prediction of hydro-morphology around spur dikes for field conditions.

1.4 Turbulence characteristics due to spur installation

The presence of a spur dike affects the flow, especially near the banks of the channel, and modifies the turbulent characteristics associated with the flow. The nature of turbulence in a flow is studied by measurement and analysis of instantaneous flow velocities in cartesian coordinates. The analysis provides various turbulent parameters of the flow, which include Reynolds shear stress, turbulent intensity, turbulent kinetic energy, bed shear stress, etc. The morphology around spur dikes is governed by turbulent flow parameters around the spur dikes. These characteristics are statistically estimated using the root-mean-square (RMS) of the turbulent velocity fluctuation and covariances for all three velocity combinations. Researchers have analyzed the flow pattern around spur dikes and determined mean velocity and turbulent flow characteristics, local scour, riverbank stabilization, and scour reduction by conducting laboratory tests and numerical simulations. The process understanding gained from these studies and our current knowledge about flow structure and morphological interactions around spur dikes is explicated in the following section.

1.4.1 Based on Experimental Results

Physical-model experiments are an effective way to learn about critical flow characteristics. Researchers experimentally studied how bed and bank stability is affected due to the influence of turbulent characteristics in the vicinity of spur dikes. As a research objective, different shapes of spur dikes are employed in various locations, with varying orientations and spur lengths, to provide suitable arrangements. An experimental flume with a fixed bed was used by Duan (2009) to analyze the three-dimensional turbulent flow zone near a spur dike. Results show that the maximum bed-shear stress was estimated at around 2–3 times the approaching flow of the mean bed-shear stress, which is located just upstream of the tip of the spur.

Furthermore, turbulence intensities were high as the flow moved downstream, the mean downstream velocity was nearly zero, and the mean kinetic energy declined, whereas the turbulent kinetic energy increased.

Duan et al. (2011) investigated the mean flow and turbulence patterns with scoured and flatbed surface around a spur dike. They concluded that the turbulence intensities in the longitudinal (u') and transverse (v') components are significantly higher, while the vertical component (w') is significantly smaller than the flatbed. Furthermore, the estimated maximum bed shear stress is approximately 6-8 times the incoming flow for non-erodible and erodible bed surfaces.

Safarzadeh et al. (2016) investigated the 3D turbulent flow field near straight and T-shape spurs under a smooth flatbed. According to the experiment results, the presence of the spurs enhanced the turbulent kinetic energy (TKE) by 10 times. In addition, TKE was observed to be higher and more extended in the upstream region of the T-shape spur than in the straight spur. Circular 3D flow structures just upstream of the T-shape spur dike are considered responsible for this phenomenon.

Mehraein et al. (2017) studied the mean and turbulent flow fields experimentally and measured scour holes around a submerged and emerged spur dike in a 90° bend. They found that TKE reaches its highest value near the spur dikes at the upstream tip and elongates as it approaches the downstream border between the approach and recirculating flow. They also showed that TKE-predicted bed shear stress shows a good association between scour and bed shear stress.

Kumar and Ojha (2021) used an unsubmerged L-head spur dike to investigate mean and turbulent flow characteristics. They observed that the magnitude of the bed shear stress, vertical Reynolds stress, and turbulent kinetic energy decreases in the wake zone as groyne's configuration and constriction ratio increases. In another study, they found that as the flow approaches the spur dike, the magnitude of turbulent kinetic energy increases; however, this decreases significantly in the confined region of the groyne faces inside the wake zone. They also found that bed shear stress increases considerably (by 4.78 times the approaching bed shear stress) within the inner wake zone at the groyne faces and near the submerged dike. The effects of the spur dike on turbulent properties under ice cover circumstances were evaluated by Jafari and Sui (2021). The most significant velocity fluctuations were observed above the scour hole and near the spur wing. In addition, ice on the water surface alters the bed shear stress and increases turbulence intensities inside the scour holes, which can substantially impact sediment movement. They also observed Reynolds shear stress and found it is negative inside the scour holes, but it becomes positive as it approaches the flow surface and reaches its maximum just above the scour holes.

Lodhi et al. (2021) explored turbulent characteristics near spur dikes. According to their findings, higher longitudinal velocity values were going beyond the scour hole zone and were lower within the scour hole region. The Reynolds stresses and turbulence intensities were greater in the scour hole in the spur dike's wake zone, and the wake zone had the greatest TKE value. Due to an increase in the degree of submergence, the TKE increases in front of the spur

dike and decreases at the axis as well as at the rear side of the dike (Yu et al., 2022). Physical model studies were conducted by Wang et al. (2022) on the spur dikes in the Three Gorges Reservoir area of the Yangtze River due to the action of landslide surge. The results show significant effects on the circumferential wave pressure upstream and downstream of the spur dike due to landslide surge.

1.4.2 Based on Numerical Simulations

Many researchers studied the flow and turbulence characteristics in the zone of spur dike that extends over the straight channel by using different numerical simulation models based on their performance, such as large-eddy simulation (LES), detached eddy simulation (DES), etc. These models were validated or compared with the measured experimental work.

Giri et al. (2004) employed a 2D numerical model to simulate the mean flow field, vorticity, and turbulence intensity and validated it with the experimental data using an acoustic Doppler velocimeter. Unsubmerged spur dikes with different orientations were placed along the bank of the meandering experimental flume.

An ADV was used by Kuhnle et al. (2008) to monitor flow velocities in a laboratory flume around a submerged, trapezoidal-shaped spur dike, and the numerical simulation model employs the finite element method to solve the following equations: Reynolds stress equations and the *k-e* turbulence closure scheme:

$$\bar{u}_{i,i} = 0 \tag{1.1}$$

$$\bar{u}_{i,t} + u_j u_{i,j} + (\overline{u_i' u_j'})_{,j} + \frac{\bar{p}_{,i}}{\rho} + f_i = 0 \tag{1.2}$$

$$k_{,t} + \bar{u}_j k_{,j} - \left(\frac{\nu_t}{\sigma_k} k_{,j}\right)_{,j} = P - \varepsilon \tag{1.3}$$

$$\varepsilon_{,t} + \bar{u}_j \varepsilon_{,j} - \left(\frac{v_t}{\sigma_\varepsilon}\varepsilon_{,j}\right)_{,j} = C_{1\varepsilon} P \frac{\varepsilon}{k} - C_{2\varepsilon}\frac{\varepsilon^2}{k} \quad (1.4)$$

Where $\bar{u}_i$ = mean velocity; u_i' = fluctuation of turbulent velocity; t =time; P = production (turbulent kinetic energy); $\bar{p}$ = mean total dynamic pressure; k = turbulent kinetic energy; ε = rate of dissipation of turbulent kinetic energy; v_t = turbulent eddy viscosity $\left(C_\mu k^2/\varepsilon\right)$; f_i = forcing term and ρ =density of water. Constant of $k-\varepsilon$ model were assigned from standard values recommended by Launder and Sharma (1974).

The mean velocity profiles and bed shear stress were obtained at various places near the spur dike. They found that the maximum bed shear stress near the trapezoidal-shaped spur dike was estimated at 2.7 times the approach flow value. Moreover, this value is significantly smaller than the maximum bed shear stress observed for flat plates.

Yazdi et al. (2010) used a numerical model, Fluent $(k-\omega)$, to predict flow patterns in the zone of spur dike. In this research, the objective was to determine $\mu_t = C_\mu \rho(k/\omega)$, and following transport equations (Launder & Spalding, 1983) were used to obtained k and ω:

$$\rho\frac{Dk}{Dt} + \rho u_j k_j = \left(\mu + \frac{\mu_t}{\sigma_k}k_j\right) + G_k - \rho\omega k \quad (1.5)$$

$$\rho\frac{D\omega}{Dt} + \rho u_j \omega_j = \left(\mu + \frac{\mu_t}{\sigma_\varepsilon}\omega_j\right) + C_1\frac{\omega}{k}G_k - C_2\rho\omega^2 \quad (1.6)$$

where $C_\mu = 0.09$ is an empirical constant; $\mu = \mu_0 + \mu_t$ where μ_0 is viscosity of fluid, μ_t the turbulence viscosity; G_k represents the generation of turbulent kinetic energy due to the mean velocity gradients, C_1 and C_2 are constants, σ_k and σ_ε are the turbulent Prandtl numbers and other standard constant used in this model recommended by Launder and Spalding (1983).

The impacts of flow discharge, spur dike length, and orientation on the bed shear stress distribution were also investigated. They concluded that vertical spur experiences higher bed-shear stress than the stream's spur dikes-oriented upside or downside. Also, the Shear stress

increases for longer spur dikes as the higher velocities flow through, the narrower the flow cross-section.

Koken and Gogus (2015) studied the turbulent flow pattern by using DES (detached eddy simulation) model around isolated spur dikes of three different lengths. The investigations revealed that as the spur dike length increased, the substantial bed shear stress values near the tip of the spur dike increased. Additionally, the upstream sections of the separated shear layers and the upstream regions of the primary horseshoe vortex increased. To determine the modified eddy viscosity following transport equation is solved:

$$\frac{\partial \tilde{v}}{\partial t} + u^j \frac{\partial \tilde{v}}{\partial \xi^j} = C_{b1}\tilde{S}\tilde{v} + \frac{1}{\sigma}\left[\nabla\left((v - \tilde{v})\nabla\tilde{v}\right) + C_{b2}(\nabla\tilde{v})^2\right]C_{w1}f_w\left[\frac{\tilde{v}}{d}\right]^2 \quad (1.7)$$

Where, v is the kinematic viscosity, u^j is the contravariant resolved velocity, t is time, d is the turbulence length scale, and ξ^j is the curvilinear coordinate in the j direction. The other variables and parameters are:

$$\tilde{S} = S + (\tilde{v}/k^2 d^2) f_{v2} \quad (1.8)$$

where S is the magnitude of the vorticity, k is the Von Karman constant, which is 0.41 and

$$f_{v2} = 1 - \tilde{v}/\left(\frac{1}{R} + \tilde{v}f_{v1}\right) \quad (1.9)$$

The eddy viscosity v_t is obtained from

$$v_t = \tilde{v} f_{v1} \quad (1.10)$$

Where:

$$f_{v1} = X^3/(X^3 + C_{v1}^3) \quad (1.11)$$

$$X = \frac{\tilde{v}}{v} + 0.5\frac{k_s}{d} \quad (1.12)$$

$$f_w = g\left(\frac{1 + C_{w3}^6}{g^6 + C_{w3}^6}\right)^{1/6} \tag{1.13}$$

$$g = r + C_{w2}(r^6 - r) \tag{1.14}$$

$$r = \frac{\tilde{\nu}}{\tilde{S}k^2d^2} \tag{1.15}$$

The model constants in the above equations are: C_{b1} = 0.135, C_{b2} = 0.622, σ = 0.67, C_{v1} = 0.71, C_{w2} = 0.3, C_{w3} = 2.0 and $C_{w1} = C_{b1}/k^2 + (1 + C_{b2})/\sigma$.

Kang et al. (2021a) examined flow patterns and turbulence characteristics in an open-channel flume around three commonly utilized instream rock constructions. ADV was used to detect velocity fields in the wake of these instream objects, and the findings were compared to large-eddy modeling results. To perform LES, a numerical model created by Kang and Sotiropoulos (2011) was used. Results showed that the estimated three-dimensional velocity components and Reynolds shear stress at different sites agreed perfectly. The numerical model, Fluent, was used by Indulekha et al. (2021) to simulate the flow pattern and identify an appropriate spur dikes orientation by comparing and analyzing pressure, velocity, streamlines, and turbulent kinetic energy for different spur orientations. The maximum variation in the properties, such as pressure and turbulent kinetic energy, was observed inside the contours with an orientation of 90°. The maximum pressure, velocity, and turbulent kinetic energy values were experienced near the spur dike's tip. Solution of Navier Stokes equation used for numerical simulation is based on conservation of mass and momentum. The model transport equation, standard $k - \omega$ model was employed for this modelling. Equations are expressed as:

$$\nabla\bar{U} = 0 \tag{1.16}$$

$$\frac{\partial\bar{U}}{\partial t} + \bar{U}.\nabla\bar{U} = \frac{-1}{\rho}\nabla P + \nu\nabla^2\bar{U} + fb \tag{1.17}$$

$$\frac{\partial}{\partial t}(\rho k) + \frac{\partial}{\partial x_i}\rho k U_i = \frac{\partial}{\partial x_j}\left(\Gamma_k \frac{\partial k}{\partial x_j}\right) + G_k - y_k + S_k \quad (1.18)$$

$$\frac{\partial}{\partial t}(\rho \omega) + \frac{\partial}{\partial x_i}\rho \omega U_i = \frac{\partial}{\partial x_j}\left(\Gamma_\omega \frac{\partial \omega}{\partial x_j}\right) + G_\omega - y_\omega + S_\omega \quad (1.19)$$

Where $\overline{U}$ is the velocity, P is pressure and fb is body force, Γ_k and Γ_ω represent the effective diffusivity of k and ω, respectively. y_k and y_ω are the dissipation of k and ω due to turbulence. S_k and S_ω are the user-defined source terms.

Mulahasan et al. (2021) employed (k–ε) and (k–ω), Reynolds Stress Model (RSM) turbulence models to study the flow properties around a vertical emergent sidewall abutment and compared the results with the experimental data. The result showed that the highest turbulent kinetic energy was observed at high velocity in the separation zone, and the bed shear stress was reduced in the recirculation zone. This study also observed that bed shear stresses are 2–3 times the approaching flow of the mean bed shear stress.

Iqbal et al. (2021) used the Reynolds stress turbulence model built using the three-dimensional numerical code FLUENT (ANSYS) to investigate the flow and turbulence characteristics of rectangular spur dikes with varying permeability. They found that the turbulent intensity and turbulent kinetic energy were significantly lower in the permeable spur dike than in the impermeable spur dike. As a result, they recommended that a permeable spur dike be used to prevent the spur dike head from strong turbulent flow during floods and to minimize the recirculation zone of the spur dike field. Reynolds averaged equations (governing equations) for continuity and momentum are given below:

Continuity equation as:

$$\frac{\partial U_i}{\partial x_i} = 0 \quad (1.20)$$

Momentum equation as:

$$U_j \frac{\partial}{\partial x_j}(U_i) = \frac{v}{\rho}\frac{\partial}{\partial x_j}\left(\frac{\partial U_i}{\partial x_j} + \frac{\partial U_j}{\partial x_i}\right) - \frac{1}{\rho}\frac{\partial P}{\partial x_i} + \left(-\rho u_i u_j\right) \quad (1.21)$$

Where $-\rho u_i u_j$ are the Reynolds stresses.

General form of the Reynolds stresses transport equation describes as:

$$\frac{\partial R_{ij}}{\partial t} + C_{ij} = P_{ij} + D_{ij} + \varepsilon_{ij} + \prod_{ij} + \Omega_{ij} \quad (1.22)$$

Where $\partial R_{ij}/\partial t$ represent the rate of change of Reynolds stresses, C_{ij} is the convection transport, P_{ij} represent the rate of generation of Reynolds stresses due to diffusion, ε_{ij} represent dissipation rate of stresses, $\prod_{ij}$ represent the distribution of stresses to turbulent pressure-strain interactions, and Ω_{ij} is the distribution of stresses due to rotation.

Kang et al. (2021b) studied the mean flow and turbulence characteristics under a low length-to-depth ratio near a non-submerged rectangular spur. A large-eddy simulation model was employed for the studies, and the results were compared with experimental data (ADV). A numerical model developed by Kang and Sotiropoulos (2011) was employed to carry out LES. They noticed that the horseshoe vortex significantly increases bed shear stress under its trajectory and around the spur dike of its upstream corner. They also found that the maximum bed shear stress was almost 17 times the entering flow's mean bed shear stress. Permeable spur dikes placed in spillway bends were found effective in reducing velocities, as well as increasing the energy dissipation rate up to 21% (Yang et al., 2022a). Haider et al. (2022b) studied the flow turbulence around two spur dike patterns (L and T) using computational fluid dynamics (CFD) with a standard $k-\varepsilon$ model. Both the dike patterns were found effective in damping velocities and turbulence intensities in the riverbank flow, as compared to the conventional

spur dike. Chen et al. (2022) studied the turbulence statistics in the detached shear layer behind a spur dike using Large-Eddy Simulations.

Several investigations conducted to disclose the three-dimensional flow characteristics surrounding a spur dike are summarized in Table 1.1 and 1.2.

Table 1.1 A summary of the geometric and hydraulic conditions of previous experiments and simulations

S.no	Authors	Shape of spur	Single/ Series	Orientation angle (projected from upstream bank)	Experimental/ numerical	Model/method used	*Re* (Reynolds Number)	*Fr* (Froude number)
1	Giri et al. (2004)	Rectangular	SERIES (3)	90º	Numerical simulations were substantiated using the measured experimental data (ADV)	2-D numerical model	20,000	
2	Kuhnle et al. (2008)	Trapezoidal	SINGLE	90º	Simulated numerically & Compared with experimental data (ADV)	finite element method (k–ε turbulent model)		0.2
3	Duan (2009)	Rectangular	SINGLE	90º	Experimental (ADV)		48,483	
4	Yazdi et al. (2010)	Rectangular	SINGLE	70,90, 110-degree	Numerical results verified through the experimental data (ADV)	Fluent, (k–ε turbulent model)		
5	Duan et al. (2011)	Rectangular	SINGLE	90º	Experimental (ADV)		84,059 and 53,157	
6	Koken and Gogus. (2015)	Rectangular	SINGLE	90º	Numerical simulation (DES)	DES	45,000	
7	Safarzadeh et al. (2016)	Rectangular and T-shape	SINGLE	90º	Experimental (ADV)		60,000	0.35
8	Vaghefi et al. (2016b)	T-shape	SINGLE	60,90, 120-degree	Numerical results verified through the experimental data (ADV)	SSIIM CFD software, Navier–Stokes equation, and k–ε turbulence model		
9	Mehraein et al. (2017)	T-SHAPED	SINGLE	90º	Experimental (ADV)		34,000	0.38

10	Kang (2018)	Rectangular	SINGLE	90º	LES are compared with the experiment (ADV)	LES	3.00×10^4	0.1
11	Jeon and Lee (2018)	Rectangular	SINGLE	90º	Experimental (ADV)	LES	3.00×10^4 and 6.59×10^4	0.10 & 0.90
12	Vaghefi et al. (2018)	T-shape	SINGLE	(45-degree) attractive and repelling	Numerical simulation of the experimental model (ADV)	CFD-RNG *k-E* turbulent model		
13	Kumar and Ojha (2019)	L-head	SINGLE	90º	Experimental (ADV)		25,000 − 44,000,	0.34 − 0.39
14	Kumar and Ojha (2021)	L-head	SINGLE	90º	Experimental (ADV)		3.9×10^4	0.34
15	Bahrami-Yarahmadi et al. (2020)	Rectangular and Triangular	SERIES (4)	90º	Experimental (EVM)			0.176, 0.196, 0.216, and 0.235
16	Shampa et al. (2020)	slit-type permeable spur dike	series of slit-type spurs (5)	60,90, 120-degree	Numerical simulations (PIV) substantiated using the measured experimental data (EVM)	3D RANS; *k-ω* SST	34,430	0.71
17	Kang et al. (2021a)	J-hook vanes, Rock vanes, and bendway weirs	SINGLE	rock vanes-20,30-degree J-hook vane-30degree bendway weirs-60,80-degree	Large-eddy simulation (LES) and flume experiments (ADV)	LES	4.08×10^4	0.19
18	Mirzaei et al. (2021)		SINGLE	90º	Numerical simulation is compared with experimental results.	FLOW 3D-LES turbulence model		
19	Jafari and Sui (2021)	Rectangular	SERIES (2)	90º, 60º, and 45º	Experimental (ADV)			0.19,0.15,0.10
20	Akbari et al. (2021)	T-shape	SINGLE	60°, 89°, 91°, and 150°	Experimental (ADV)		67,857	0.34
21	Lodhi et al. (2021)	Rectangular	SINGLE	90º	Experimental (ADV)		87,474	0.65
22	Kang et al. (2021b)	Rectangular	SINGLE	90º	Numerical simulation & Experimental (ADV)	LES	3.00×10^4	0.1
23	Kafle (2021)	Rectangular	SERIES	90º	Numerical simulation	CFD-- model Nays 2D		
24	Iqbal et al. (2021)	Rectangular	SERIES	90º	Numerical simulation (PIV)	Reynolds stress model RSM	10,000	0.13

						[*FLUENT* (ANSYS)]		
25	Mulahasan et al. (2021)	Rectangular	SINGLE	90º	Simulated numerically & Compared with experimental data	*k-Ɛ,k-w*, RSM CFD-VOF-ANSYS FLUENT	(6,560), (9,930), (10,959)	(0.409) (0.334) (0.295)
26	Indulekha et al. (2021)	Rectangular	SERIES (6)	15,30,45,90,120, 150 degree	Simulated numerically & Compared with experimental data	ANSYS Fluent.		0.35
27	Yu et al. (2020)	Five different shapes	SINGLE	90º	Experimental (ADV)			
28	Pourshahbaz et al. (2022)	Rectangular	SERIES (3)	90º	Numerical simulations substantiated using the experimental data (ADV)	FLOW-3D and SSIIM 2.0		0.19, 0.25

CFD, Computational fluid dynamics; EVM, Electromagnetic velocity meter; PIV, Particle image velocimetry; DES, Detached eddy simulation; LES, Large-eddy simulation.

Table 1.2 A summary of the previous work related to turbulent characteristics

S.no	Authors	3D velocity	BSS	TKE	RSS	TI
1	Giri et al. (2004)	✓	✓	✓	✓	✓
2	Kuhnle et al. (2008)	✓	✓	▪	▪	▪
3	Duan (2009)	✓	✓	✓	✓	✓
4	Yazdi et al. (2010)	✓	✓	▪	▪	▪
5	Duan et al. (2011)	✓	✓	✓	✓	✓
6	Koken and Gogus (2015)	✓	✓	✓	▪	▪
7	Safarzadeh et al. (2016)	✓	▪	✓	▪	▪
8	Mehraein et al. (2017)	✓	✓	✓	▪	▪
9	Jeon and Lee (2018)	✓	▪	✓	✓	✓
10	Kumar and Ojha (2019)	✓	✓	✓	✓	✓
11	Kumar and Ojha (2021)	✓	✓	✓	✓	▪

12	Kang et al. (2021a)	✓	▪	✓	✓	✓
13	Indulekha et al. (2021)	✓	▪	✓	▪	▪
14	Mulahasan et al. (2021)	✓	✓	✓	▪	▪
15	Iqbal et al. (2021)	✓	▪	✓	▪	✓
16	Kang et al. (2021b)	✓	✓	✓	✓	▪
17	Lodhi et al. (2021)	✓	▪	✓	✓	✓
18	Jafari and Sui (2021)	✓	✓	✓	✓	✓

BSS, Bed shear stress; TKE, Turbulent kinetic energy; RSS, Reynold's Shear Stress; TI-Turbulent Intensity.

1.5 Effect of spur dike on aquatic ecosystem

Spur dikes significantly influence aquatic ecosystems by altering local hydraulics and habitat conditions. Their construction modifies flow patterns, creating velocity shelters that benefit juvenile and larval fish Niles and Hartman (2011). However, these structures also induce changes in sediment transport and water quality, potentially affecting fish spawning grounds and aquatic biodiversity Chen et al. (2013). During construction, the use of non-ecological materials, such as geotextile concrete mattresses, can cause temporary ecological disturbances Shiming et al. (2012). While habitat models have been employed to assess the physical suitability of these modified environments Yao and Rutschmann (2015), long-term ecological consequences, including impacts on migratory fish and biodiversity, remain underexplored. Incorporating habitat-based assessments and environmental flow considerations (Yi et al., 2010; Stamou et al., 2018) would provide a more comprehensive understanding of the ecological trade-offs associated with spur dike implementation.

1.6 Need for Research

River banks are susceptible to the displacement of soil particles, resulting in bank erosion. The eroded sediments get deposited along the river as they flow downstream, causing a change in

the bed level of the rivers. This deterioration of river banks and deposition along the river course can affect the natural equilibrium of rivers, lands, and control structures constructed over the river. Therefore, river bank stabilization is one of the major concerns in open channel flow for reclamation of the environment and to secure important structures. A spur dike is one of the best solutions to this challenging scenario. A spur dike or groyne is one of the most commonly used river training structures that stabilize the river bank by protecting it from erosion.

The scouring in the channel can affect the strength of the spur dike or any structure, making it prone to failure (Pandey et al., 2019; Mehta & Yadav, 2020; Zolghadr et al., 2023). To prevent this, engineers must consider the maximum expected scouring depth around the spur dike during construction. However, predicting the exact scour depth remains challenging (Pandey et al., 2021a). Predicting and estimating the maximum depth of scour around spur dikes, as well as understanding the factors contributing to it, are essential for the efficient and risk-free construction of spur dikes (Rahman & Muramoto, 1999; Mohammadpour et al., 2016; Pandey et al., 2016, 2018, 2021b; Wang et al., 2017; Tripathi & Pandey, 2022; Fuladipanah et al., 2023).

Many researchers studied and explored different factors influencing the flow behavior around spur dike. Discussion about various aspects during the implementation of this structure, such as spur dike design, alignment, length, spacing between the spurs, orientation, contraction ratio, permeability, appearances as a single spur dike or series of spur dike, etc., are evaluated. Researchers have been studying the influence of these factors independently and combined to determine which ones contribute more significantly to the scouring process.

Several previous researchers have explored this topic; however, they frequently missed an important factor that significantly impacts sediment movement along the channel bed and

banks, even in the presence of spur dikes, which is seepage. Natural channels typically have significant seepage flows from their bed and banks. Seepage interacting with the primary flow can change how the flow behaves, influencing how scour patterns form around spur dikes. Consequently, spur dikes become more susceptible to scouring, potentially leading to failure.

Seepage from a channel (Figure 1.8), whether downward (referred to as suction) or upward (referred to as injection), plays a crucial role in influencing bed deformation and altering the channel's hydrodynamic characteristics. Injection increases the water volume in the channel, whereas suction reduces it.

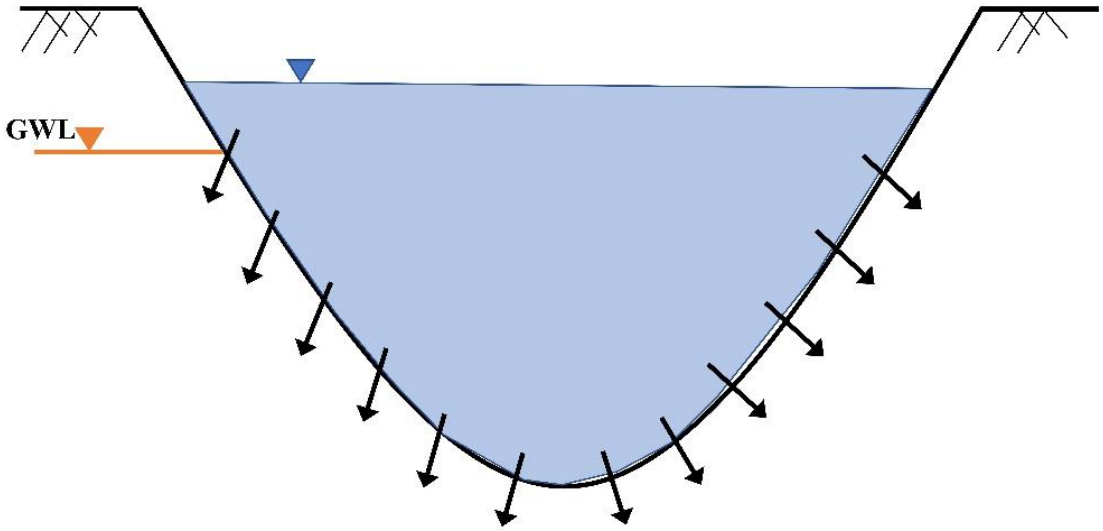

Figure 1.8 Downward seepage through boundaries of alluvial channels

Real-world studies across different regions have consistently highlighted the significant water losses caused by seepage in unlined irrigation canals, emphasizing its impact on water delivery efficiency and the sustainability of water resources. In Central Board of Irrigation and Power, New Delhi, India, seepage losses accounted for an estimated 45% of the total diverted flow rate, indicating the inefficiency of water delivery systems in unlined canals and the substantial loss of valuable water resources before they reach agricultural fields Sharma (1975). Similarly, in semi-arid regions, seepage losses in unlined earthen canals were found to range between

20% and 50% of the total flow volume. Such high losses exacerbate water scarcity issues in regions already facing significant water stress (Yussuff et al., 1994; Tanji & Kielen, 2002).

In the United States, the U.S. Geological Survey (Carr, J. E., 1990). reported that 17% of the irrigation water conveyed in 1985 was lost to seepage and evaporation, highlighting the inefficiency of water conveyance systems. In the Lower Rio Grande Valley of Texas, Fipps (2000) estimated a conveyance efficiency of 69.7%, implying that more than 30% of the diverted water was lost. This inefficiency underscores the need for improved canal designs and mitigation measures. In the Middle Rio Grande Valley, New Mexico, a study using Acoustic Doppler Current Profilers equipment revealed that over 40% of the diverted water volume in earthen canals was lost to seepage. This finding emphasized the importance of employing advanced monitoring techniques to accurately quantify seepage losses and improve water management strategies Kinzli et al. (2010).

Further studies on seepage losses in various conditions have revealed concerning findings. Such as, Van der Lely (1994) estimated seepage losses accounting for 15–25% of the total intake, while Berenbrock (1999) documented volumetric losses ranging between 12% and 20% in detailed case studies. Langhoff et al. (2006) reported that almost 50% of seepage flow was lost through the streambed, indicating significant inefficiencies in water conveyance. Martin and Gates (2014) highlighted that unlined canals could lose up to 15% of the upstream flow due to seepage, further emphasizing the vulnerability of such systems to water losses.

Previous research shows that downward seepage significantly impacts channel geometry, according to previous research (Deshpande & Kumar, 2017; Sharma et al., 2020; Taye et al., 2023). According to Cao and Chiew (2014) increasing downward seepage rates leads to increased bedload conveyance rates, which affect the channel's shape and the ecosystem's ecology. Sharma and Kumar (2018) also investigated how downward seepage affected a sand bed channel and found that it increased turbulence kinetic energy and turbulent intensity. In a

recent study, Taye et al. (2023) evaluated the impact of downward seepage on the flow through sinuous channels. The study found that trapezoidal channels experienced a velocity increase of 20%, while rectangular channels showed a 26% rise due to seepage effects.

Moreover, several other studies have also shown that downward seepage enhances the sediment transport rate and alters the hydrodynamic parameters of the channel. These studies include works (Lu et al., 2008; Rao et al., 2011; Sreenivasulu et al., 2011; Liu & Chiew, 2012; Devi & Kumar, 2016; Deshpande & Kumar, 2017; Sharma et al., 2021; Taye & Kumar, 2021). In contrast, certain studies have examined how downward seepage impacts scour depth around different hydraulic structures. For instance, researchers (Qi et al., 2013; Chavan & Kumar, 2017) reported a reduction in scour depth at the bottom of the pier with downward seepage. However, other studies, such as those by Francalanci et al. (2008) and Patel and Kumar (2023) have shown that downward seepage can lead to scouring. Prinos (1995) found that downward seepage leads to significant modifications in flowing water near the channel bed when associated with a river intake structure, causing increased boundary shear stress and potential localized erosion and damage to the intake structure. Jahan (2014) conducted a study on circular bridge piers to investigate the impact of downward seepage on scour depth. The research revealed that 2% seepage reduced the scour depth, while 5–10% seepage increased it. Furthermore, when there was 5–10% suction, approach velocities near the bed increased but decreased near the water's surface. The research also observed that under 5% suction, the equilibrium scour depth increased by approximately 23%, and under 10% suction, it increased by about 42%, compared to conditions without suction.

Researchers have recently highlighted the need to consider seepage (downward) effects when constructing and analyzing flow around spur dikes (Naranjo et al., 2023; Patel & Kumar, 2023; Patel et al., 2023a).

1.7 Objectives of the study

Based on the study, the following are the objectives of the present research work:

1) Experimental Study on the Optimal Spur Dike Shape under Downward Seepage
    - Scour depth evolution and bed morphological changes around these spur dike shape
    - Turbulent characteristics around T-shape, L-shape and Rectangular shape spur dike
    - Migrating scour depth around an optimised T-shape spur dike with downward seepage using multiscale characterizations
2) Channel Morphology with Permeable Spur Dikes under Downward Seepage
    - Study the effects of varying permeable and impermeable spur dike combinations on scouring under downward seepage.
    - Study the flow pattern around these permeable spur dikes with seepage.
3) Optimal Spur Dike Orientation for Scour Mitigation under Downward Seepage Conditions
    - Assessment of temporal variation in bed morphology and scour patterns with seepage.
    - Study how different orientations of spur dikes (60º, 90º, and 120º) affect local scouring and compare the formation with downward seepage.
    - To optimise spur dike orientation for managing flow turbulence and reducing local scouring under downward seepage.

A schematic view of the objectives outlined in the present research work is shown below (Figure 1.9):

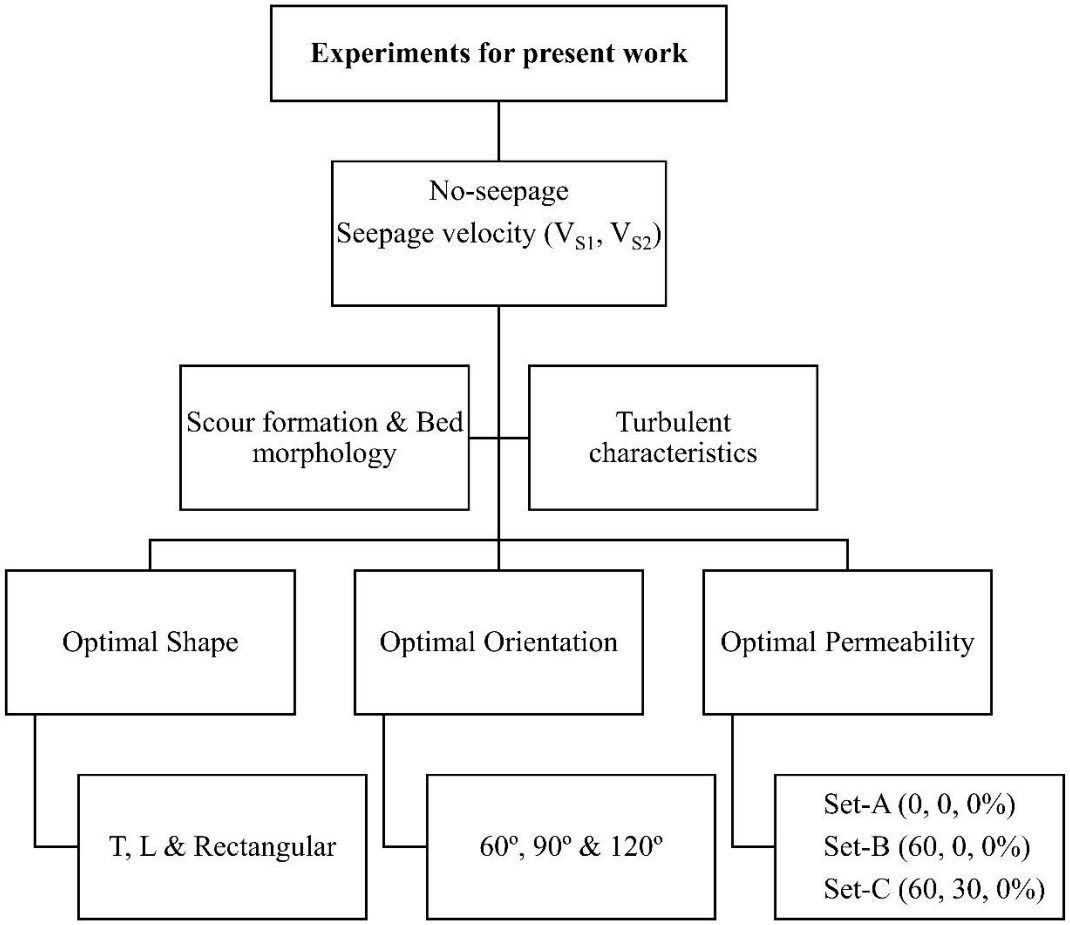

Figure 1.9 Experimental program in the present research work

1.8 Thesis Organization

The thesis has been organised into six chapters. A brief introduction to the chapters is given below:

Chapter 1 "Introduction" presents an introduction to spur dike, scour and related problems. Review of the literature of various pioneering researchers on scouring around spur dikes is carried out, and the effect of downward seepage on the transportation of sediments is discussed. After a critical review, various objectives of the present study are outlined in this chapter.

Chapter 2 "Experimental Setup and Methodology" gives a detailed description of the facilities and equipment used for experimental tests. Additionally, this chapter presents the

development of the flume, the design of the physical model, the bed material, the spur dike arrangement, data collection and its processing with the results given.

Chapter 3 "Experimental Study on the Optimal Spur Dike Shape under Downward Seepage" aims to investigate how various shapes of spur dikes in a channel influence scouring processes, with the ultimate goal of identifying the most efficient spur dike designs from many potential options. The investigation concentrated on three distinct spur dike shapes (T, L, and rectangular) under different seepage velocities (V_{S1} and V_{S2}) and a no-seepage condition. The current study also illustrates changes in bed morphology, multiscale characterizations of migrating scour depth, and temporal and longitudinal evolution of scour depth with and without downward seepage.

Chapter 4 is concerned with the experimental study to investigates permeable spur dikes and their effect on managing flow turbulence, reducing local scour around T-shaped spur dikes when subjected to downward seepage.

Chapter 5 provides insight into the temporal variation in bed morphology and scours around rectangular-shaped spur dikes with different orientations such as 60º, 90º, and 120º. Also, maximum scour depth is developed compared to the condition when downward seepage is applied. The experiments examined the suitability of various spur dike orientation configurations and the scour development over time, specifically at intervals of 2, 12, and 24 hours and compared with 24 hours (Seepage).

Chapter 6 "Conclusion and Recommendations" summarizes the key findings from the current research work. Additionally, this chapter offers recommendations based on these findings and explores potential future scope of the work.

2 Experimental Setup and Methodology

2.1 Overview

The study involved conducting experiments in an experimental flume to understand the flow pattern around different spur dike designs, geometry, and the projection in alluvial channels. We performed laboratory experiments as it allowed us to adjust the experimental conditions to match our research needs. Our main goal was to explore the complex flow characteristics near these structures.

This chapter details the equipment and laboratory methods used for conducting our experiments. The experiments were designed to make the most of the available equipment while minimizing issues such as channel wall effects. The study also provides all the relevant details about how this equipment was operated. The chapter starts with a description of the available apparatus and then explains how it was used to obtain various results. Finally, it provides a detailed description of the different series of experiments that were planned and carried out during the research.

2.2 Experimental flume

Experiments were carried out in a glass-sided transparent tilting flume, which allowed for easy observation and monitoring. The flume's dimensions are 17.2 m long, 1 m wide, and 0.72 m deep. The Schematic diagram and the photograph of the tilting flume are shown in Figures 2.1 and 2.2, respectively. A tank of dimensions 2.8 m long, 1.5 m wide and 1.5 m deep was provided upstream of the flume to straighten the flow prior to its introduction into the flume. The flow rate was controlled using a valve, which is present in the upstream tank. The downstream collection tank is 1.7 m long, 1.9 m wide and 1.08 m deep. The flume is designed

for hydraulics studies (for research and training purposes) concerning sediment transport phenomena, and it is capable of re-circulating water.

One gate installed at the downstream end of the flume allows the control of the water level in the flume under subcritical flow conditions. The flume is mainly used for regime and other sediment transport experiments.

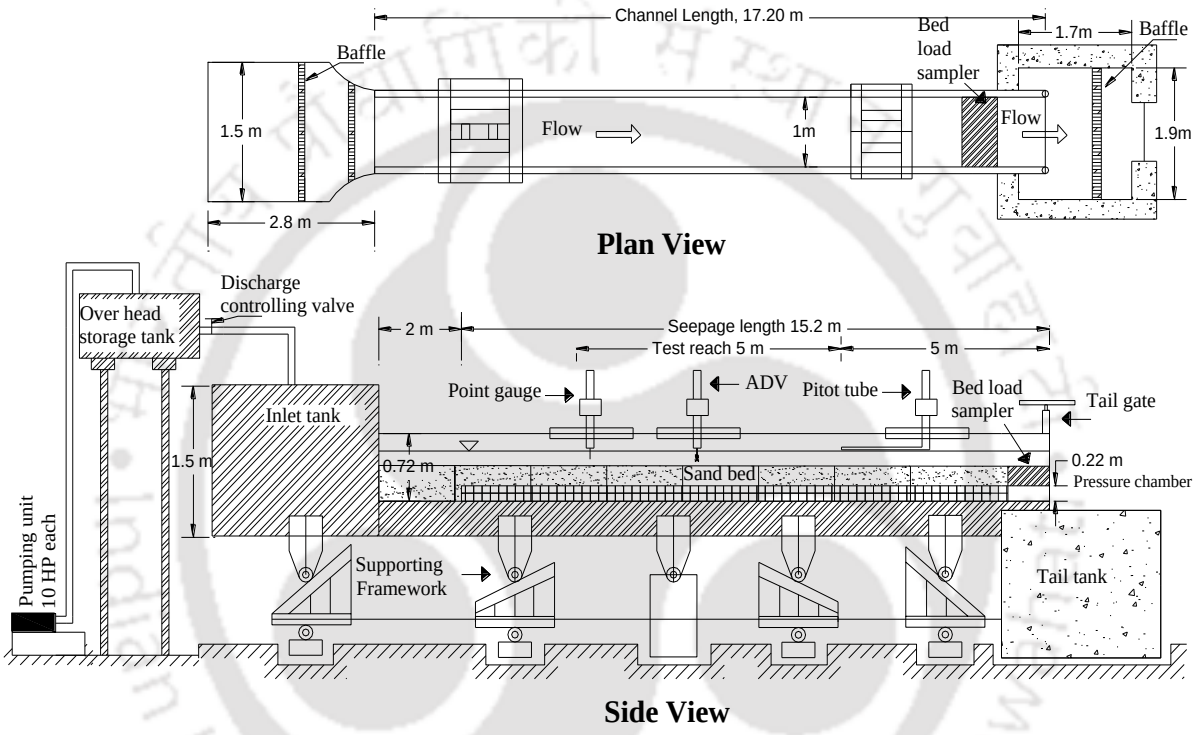

Figure 2.1 Schematic diagram of tilting flume used for studying flow behaviour around spur dikes.

Figure 2.2 Photograph of the tilting flume showing spur dike setup

2.3 Bed material

The river sands utilized for the experiment were carefully sieved to determine the median sand size *(d_{50})* from the grain size distribution curves depicted in Figure 2.3. The median sand diameters were found to be 1.1 mm and 0.23 mm, with standard deviations (σ_g) of 1.03 and 0.79, respectively. The particle size distribution for the sand was confirmed to be uniform, as

indicated by a geometric standard deviation less than 1.4 (Marsh et al., 2004). The geometric standard deviation is calculated as:

$$\sigma_g = \sqrt{d_{84}/d_{16}} \tag{2.1}$$

Where d_{84} and d_{16} are defined as the grain for which 84% and 16% of the sample is finer by weight.

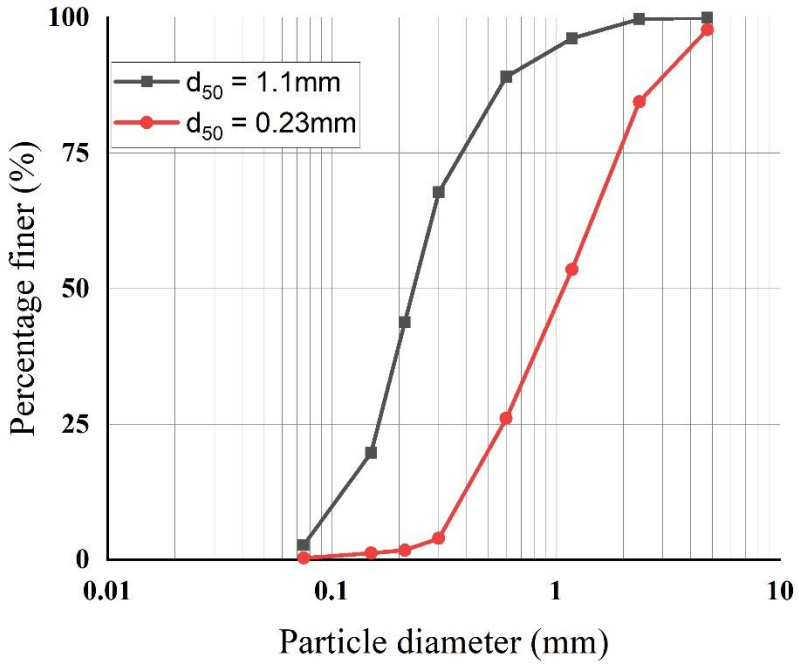

Figure 2.3 Particle size distribution curve

2.4 Bed slope

The bed slope (S_0) of the flume was measured carefully and precisely using a device known as a Total Station. This electronic device is equipped with capabilities that enable it to measure horizontal and vertical positions simultaneously with accuracy. The Total Station is composed of two main components: a precisely calibrated machine mounted on a stable tripod and a 'target' prism affixed to a metal staff. During the measurement process, the machine part of the total station, resembling a telescopic rifle sight with crosshairs, is carefully adjusted to focus on the prism. This instrument is designed to rotate horizontally and swivel vertically, allowing

for the collection of highly precise measurements. The Total Station's functionality is based on the principles used in traditional theodolites, integrating calculations derived from vertical and horizontal 360-degree scales and enhanced with an Electronic Distance Measurer (EDM) device.

2.5 Test Section

The way flow enters and exits a flume significantly affects its behavior. Directly delivering flow to the flume through pipes causes intense swirling. In our experiments, we set up the pipes to prevent these swirls. We first collect water in an upstream tank using a valve from an overhead tank. The water level rises slowly in this upstream tank before entering the channel. To ensure smooth entry into the channel, we installed baffles in the tank just before the channel. When flow spills freely over the tailgate, it speeds up near the bottom just before the gate. In the present experiments, the test section in the channel was 5 meters long and located in the middle of the flume (5-10 meters from the tailgate). The length of the flume was sufficient for fully developed flow in all the runs. The boundary layer development criteria, equal to 56 times the flow depth (Kirkgoz & Ardiclioglu, 1997; Ardiclioglu & Ozturk, 2006), were satisfied.

2.6 Seepage facility

A seepage chamber was combined with a flume with specific measurements: 15.2 m long, 1 m wide, and 0.22 m deep. The cross-sectional view of the experimental setup with a seepage chamber in section A-A is shown in Figure 2.4. This experimental setup involves placing the seepage chamber under the sediment bed and keeping them separate using a fine mesh. The mesh contains 0.1 mm holes that efficiently block silt particles, allowing water to flow freely into the seepage chamber. An evenly dispersed sand layer covers this mesh to provide a consistent bed surface.

The primary purpose of this seepage chamber is to assess the occurrence of downward seepage in the sediment bed. It achieves this by using two connected pipes at its end, through which water flows. A magnetic flow meter measures liquid flow within these pipes precisely. There are also adjustable valves in the system for controlling the seepage rate. By closing the valve connected to the flow meter, the seepage in the channel can be stopped immediately. In this study, we injected downward water seepage across the flume's alluvial streambed to simulate natural suction action. The method is consistent with the findings of Cao and Chiew (2014), who found a direct correlation between bed movement and suction zone extent. Studies and recommendations for seepage losses are presented in Table 2.1.

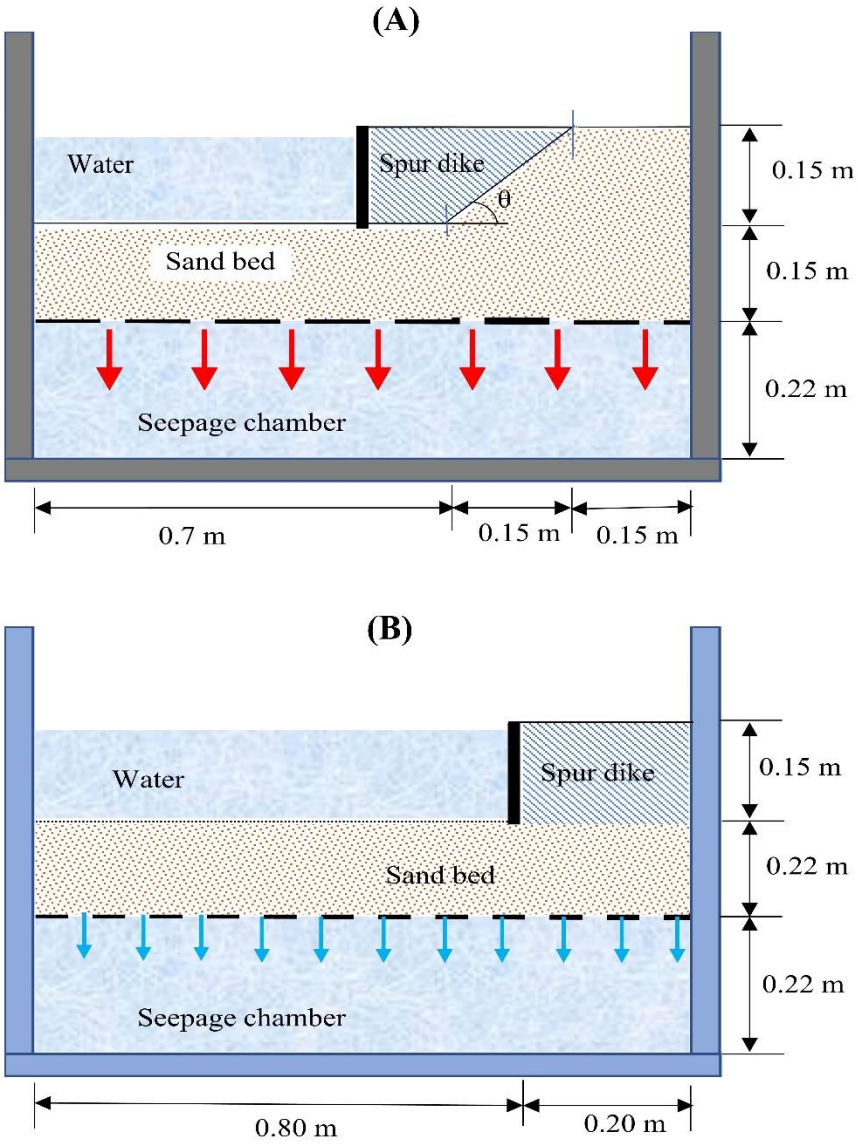

Figure 2.4 A schematic of the detailed cross-sectional view of the seepage chamber setup in sections A-A with (A) and without (B) bank.

Table 2.1 Studies and recommendations for seepage losses

Study	Key Findings/Remarks
Richardson & Simons (1984)	Investigated seepage velocities ranging from 0.0 to 0.88 mm/s
Faruque and Balachandar (2011)	Examined velocities ranging from 0.55 mm/s to 1.5 mm/s.
Dey et al. (2011)	Suggested seepage velocity should not exceed 1% of the average flow velocity in the lab.

Liu and Chiew (2012)	Examined velocities ranging from 0.0 mm/s to 3.14 mm/s.
Cao and Chiew (2014)	Explored a broader range extending from 0.4 mm/s to 7.3 mm/s.
Herrera-Granados and Kostecki (2017)	Examined velocities ranging from 0.0 mm/s to 0.05 mm/s.
Van der Lely (1994)	Estimated seepage losses accounting for 15% to 25% of the total intake
Berenbrock (1999)	Reported 12% and 20% volumetric losses in detailed case studies
Yussuff et al. (1994)	Revealed 20% to 50% water losses in semiarid earthen channels
Langhoff et al. (2006)	Found that almost half of the seepage flow was lost through the streambed
Kinzli et al. (2010)	Concluded that 40% of water was lost due to downhill seepage in New Mexico's earthen canals
Martin and Gates (2014)	Highlighted that unlined canals are susceptible to a 15% loss of initial upstream flow due to seepage

Based on available research, we calculated that downward seepage accounting for 5% to 10% of the main channel flow would be adequate. Seepage velocities of (V_S) 0.071 mm/s to 0.18 mm/s matched the mandated thresholds of volumetric losses observed in the previous study.

2.7 Data collection

2.7.1 Main Channel Discharge

A regulating valve has been connected to the overhead tank to ensure a precise and controlled supply of water to the main channel. To accurately measure the discharge in the main channel, a specifically designed rectangular notch has been strategically placed downstream of the flume (Figure 2.5). The coefficient of discharge was calculated by using the following equation:

$$Q = \frac{2}{3} C_d L \sqrt{2g}\,(h)^{3/2} \tag{2.2}$$

Where: L = length of the notch (L = 0.5 m); g = gravitational acceleration; h = height of the flow above the notch; C_d = coefficient of discharge for the rectangular notch, which was obtained to be 0.82.

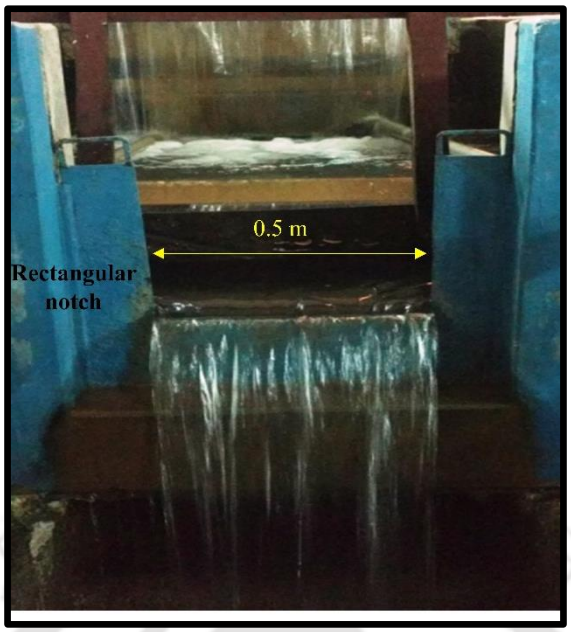

Figure 2.5 Discharge measurement at rectangular notch

2.7.2 Seepage Discharge

Two advanced electromagnetic flow meters were strategically installed at the downstream section of the flume (Figure 2.6). These meters play a crucial role in precisely measuring and controlling the desired seepage discharge. The flow meters are intricately connected to the seepage chamber through a network of pipes, ensuring seamless operation.

Figure 2.6 Electromagnetic flow meters for seepage discharge measurements

The electromagnetic flow meters work based on Faraday's law of electromagnetic induction. According to this principle, when a conductive liquid passes through a magnetic field (B), it generates a voltage (E) that is proportional to the liquid's velocity (U_c), the strength of the magnetic field (B), and the length of the conductor (X). In a flow meter, wire coils on the meter body produce a magnetic field when a current is applied. The liquid flowing through the pipe acts as the conductor and induces a voltage proportional to the average flow velocity. This induced voltage is detected by sensing electrodes mounted in the flow meter body and sent to a transmitter, which calculates the volumetric flow rate based on the pipe dimensions. Mathematically, Faraday's law can be stated as:

$$E \propto U_c B X \tag{2.3}$$

The flow meters were equipped with a control valve and a digital display used to set the desired percentage of seepage discharge. The seepage discharge can be calculated using the following equation:

$$q_s = A_p U_c \tag{2.4}$$

Where: q_s is the seepage discharge in m^3/s, A_p is the area of pipe in m^2, and U_c is the fluid velocity through the flow meter.

2.7.3 Flow Depth

The depth of the water flow was determined by utilizing a digital point gauge that was set up on a mobile trolley, as illustrated in Figure 2.7. This setup could cover the entire cross-sectional area by moving laterally and longitudinally. The gauge displayed the flow depth directly and eliminated errors caused by reading scales. It could be adjusted to zero at any point within its range to provide relative measurements. The digital display showed the flow depth in different units, with a resolution of ±0.1 mm. A quick release mechanism allowed for easy position changes. The flow depth was defined as the difference between the water surface level and the bed level.

Figure 2.7 Digital point gauge mounted on moving trolley

2.7.4 Flow Velocity and Turbulent Characteristics

A Nortek Acoustic Doppler Velocimeter (ADV) with four beams facing downward was utilized to measure three-dimensional velocities in the *X*, *Y*, and *Z* directions (streamwise, transverse, and vertical components, respectively), as shown in Figure 2.8. About 20 readings were gathered at each location's depth, and 2 min of velocity data were collected for each reading point. For data collection, a sampling frequency of 100 Hz was used. An ADV probe featuring a cylindrical remote sampling volume that could be adjusted in height. Positioned 5 cm below the central transmitter, the sampling volume's height was 4 mm when positioned away from the bed and 1 mm near the bed, ensuring no interaction with bed particles. The Acoustic Doppler Velocimeter (ADV) gathered detailed velocity data, which was then processed and stored in the computer using Vectrino+ software developed by Nortek (Figure 2.9). Data acquisition occurred over a 2-minute duration, resulting in the collection of 12,000 samples. The obtained velocity data were filtered using the Goring and Nikora (2002) acceleration threshold to ensure our velocity data was accurate and had no unwanted noise or

motion-related issues. The aim was to obtain accurate velocity data that reflects the fluid's true velocity at a particular depth. After filtration, the velocity power spectra (Figure 2.10) were analyzed to ensure compliance with the Kolmogorov −5/3 law (Devi et al., 2016).

Uncertainty analysis

The filtered data were then analyzed to examine various turbulent characteristics. Standard deviation and uncertainty measurements were conducted for average mean velocities to assess the accuracy of the Acoustic Doppler Velocimeter (ADV).

Uncertainty refers to the expected range of variation or error in the measured velocity data due to factors such as instrument precision, flow fluctuations, and sampling limitations. It provides an estimate of how much the measured value may deviate from the true value and is expressed as a percentage of the measured value.

To quantify uncertainty, fifteen repeat measurements of velocity were conducted using an Acoustic Doppler Velocimeter (ADV) at a fixed depth (z/h = 0.11) within the test section. The standard deviation and associated uncertainty were computed for each velocity component (streamwise, transverse, and vertical) using the standard error propagation method, which accounts for both systematic and random errors in repeated measurements.

For each velocity component, both time-averaged (first-order) and RMS of fluctuations (second-order), the standard deviation was calculated from the sample set. The percentage uncertainty and standard deviation was then derived using:

$$\text{Standard Deviation} = \sqrt{\frac{\sum_{i=1}^{n}(\text{observed value - mean value})^2}{n}} \tag{2.5}$$

$$\text{Uncertainity (\%)} = \left(\sqrt{\frac{\sum_{i=1}^{n}(\text{observed value - mean value})^2}{n \times (n-1)}} \right) \times 100 \tag{2.6}$$

Where, *n* is the number of measurements carried out with ADV to evaluate the standard deviation and uncertainty associated with ADV measurements.

The uncertainty analysis confirmed the validation of the measurements presented in Table 2.2. The results indicate that the ADV is a precise instrument, as the flow characteristics exhibit minimal uncertainty.

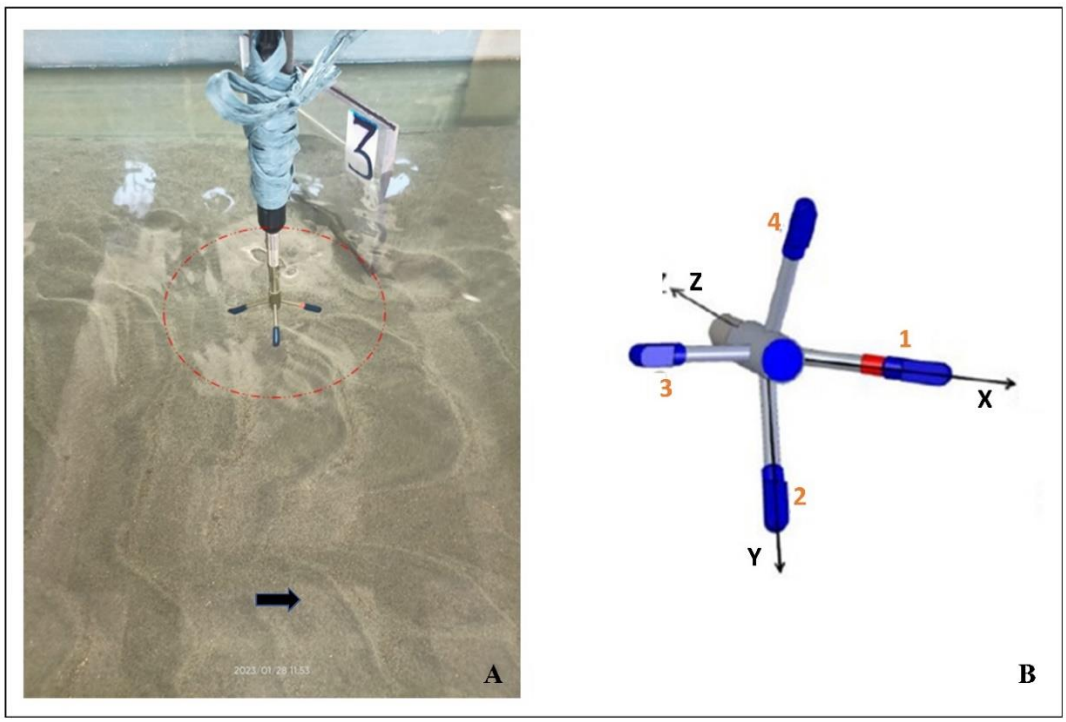

Figure 2.8 Acoustic Doppler Velocimeter for measuring instantaneous velocities

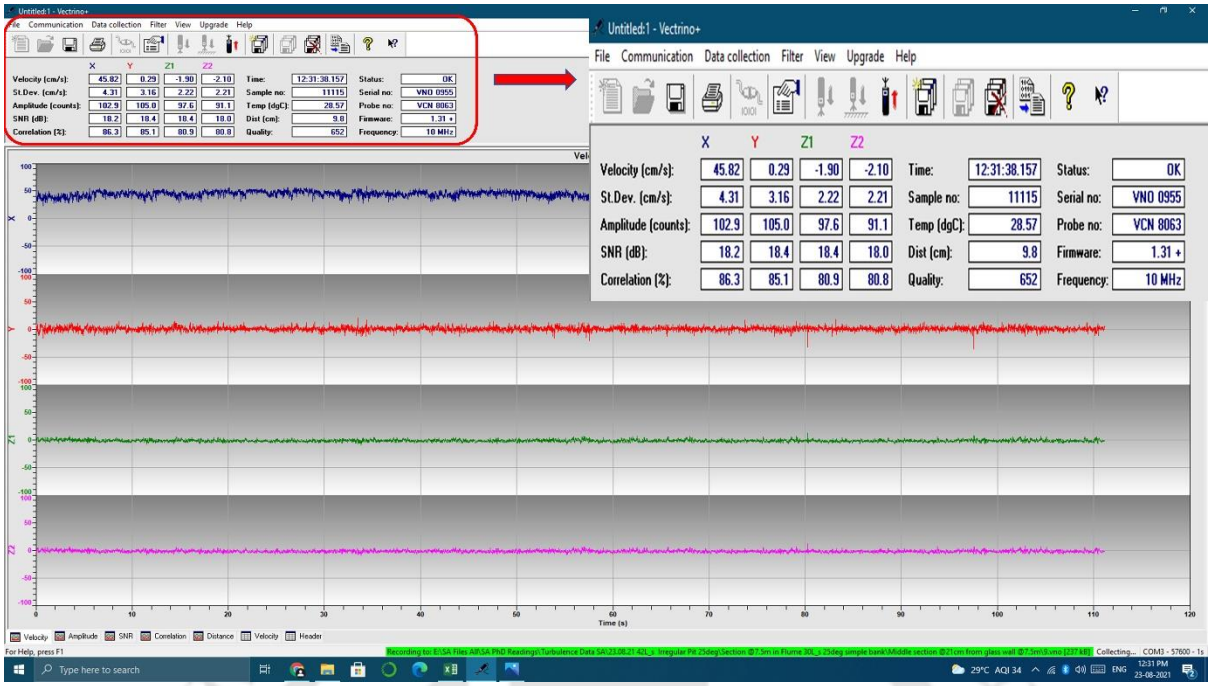

Figure 2.9 Vectrino + software for velocity data collection

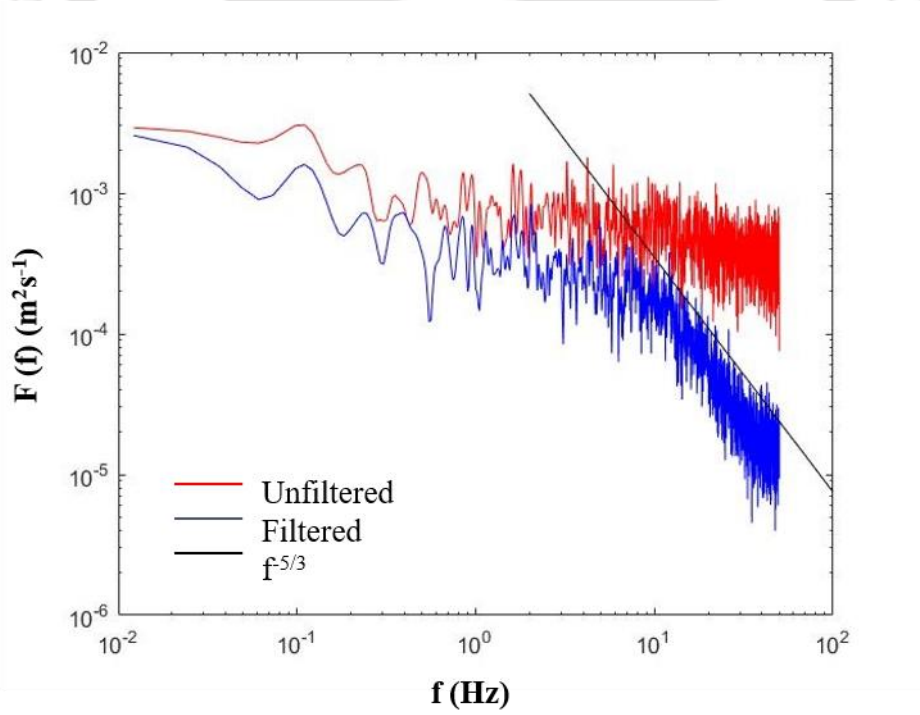

Figure 2.10 Velocity power spectra showing the fit of Kolmogorov's -5/3 scaling law

Time-averaged (mean) velocities

The time-averaged velocities in the streamwise, transverse, and vertical directions given as:

$$\bar{u} = \frac{1}{n}\sum_{i=1}^{n} u_i \; ; \; \bar{v} = \frac{1}{n}\sum_{i=1}^{n} v_i \; ; \; \bar{w} = \frac{1}{n}\sum_{i=1}^{n} w_i \tag{2.7}$$

where:

$(\bar{u}, \bar{v}, \bar{w})$ are the time-averaged velocities in the respective directions,

(u_i, v_i, w_i) are the instantaneous velocity components in the respective directions

(n) is the total number of velocity samples collected.

According to Reynolds decomposition, turbulent velocities are the sum of two components, i.e., mean $(\bar{u}, \bar{v}, \bar{w})$ and fluctuating velocity components (u', v', w') such that streamwise, transverse, and vertical velocities are defined as $u_i = \bar{u} + u'$, $v_i = \bar{v} + v'$, and $w_i = \bar{w} + w'$, respectively.

Table 2.2 Uncertainty analysis of velocity data.

	Time-Averaged Velocities			RMS (root mean square) of velocity fluctuations		
Directions	Streamwise	Transverse	Vertical	Streamwise	Transverse	Vertical
Components	$\bar{u}$ (m/s)	$\bar{v}$ (m/s)	$\bar{w}$ (m/s)	$\left(\overline{u'u'}\right)^{0.5}$ (m/s)	$\left(\overline{v'v'}\right)^{0.5}$ (m/s)	$\left(\overline{w'w'}\right)^{0.5}$ (m/s)
Standard deviation	3.8×10^{-3}	3.4×10^{-5}	2.7×10^{-5}	3.94×10^{-4}	3.26×10^{-4}	1.6×10^{-5}
Uncertainty (%)	0.201	0.144	0.126	0.074	0.032	0.101

2.7.5 Temperature and Kinematic Viscosity

We measured the average water temperature during the experiments using a Vectrino+ ADV. This device has a temperature sensor (thermistor) inside the probe head. We then determined the corresponding value of kinematic viscosity (in cm^2/s) from standard tables.

2.7.6 Bed morphology

The digital point gauge, which had a least count of 0.01 mm, was employed to capture the modification in bed morphology after the experimental run. Moreover, the temporal scour formation is captured through a laser distance meter with an accuracy of ±1 mm (Figure 2.11). Measurements were taken until the scour depth reached equilibrium. Both instruments were attached to a mobile trolley, making it easy to measure. To create a 3D picture of the bed surface, elevation data were recorded every 5 cm along the length up to 1.5-2.5 m and every 2–5 cm across the width up to 1 m, depending on the bed undulations.

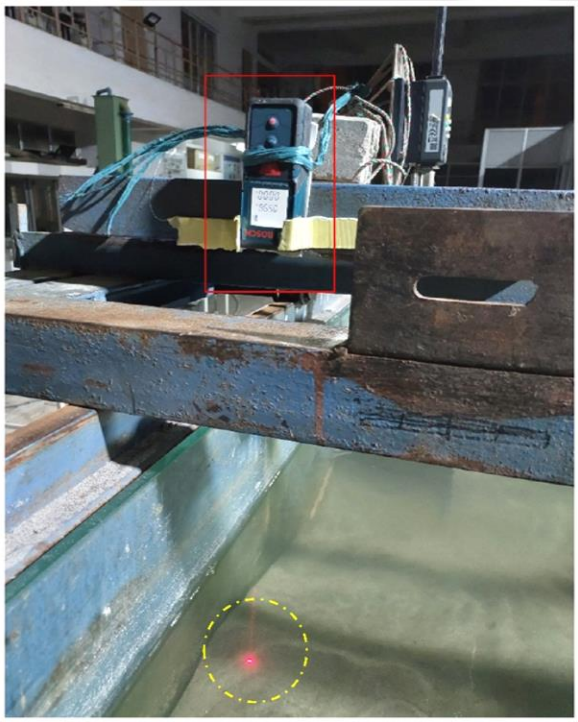

Figure 2.11 Laser distance meter mounted on moving trolley

2.7.7 Ultrasonic Ranging System (URS)

To monitor bed morphological modifications during the experiments over time and the rate of scour development, the Sea Tek 5 MHz Ultrasonic Ranging System (URS) was utilised. The ultrasonic ranging system used for measuring water surface elevation has an accuracy of **±1 mm** under laboratory conditions. This level of precision is suitable for detecting small variations in flow depth and surface fluctuations within the experimental flume. The system was regularly calibrated and positioned vertically above the flow to minimize angular error and ensure reliable measurements.

This system employed eight transducers attached to a movable trolley; out of those, we utilised five, as shown in Figure 2.12, which emitted a 10-second pulse that travelled through the water and was reflected to the transducer after hitting a target. The distance to the object was then calculated using the returned signal, and data were gathered from different sections of the bed using this method. The collected data was then analysed to investigate the temporal variations in bed morphology.

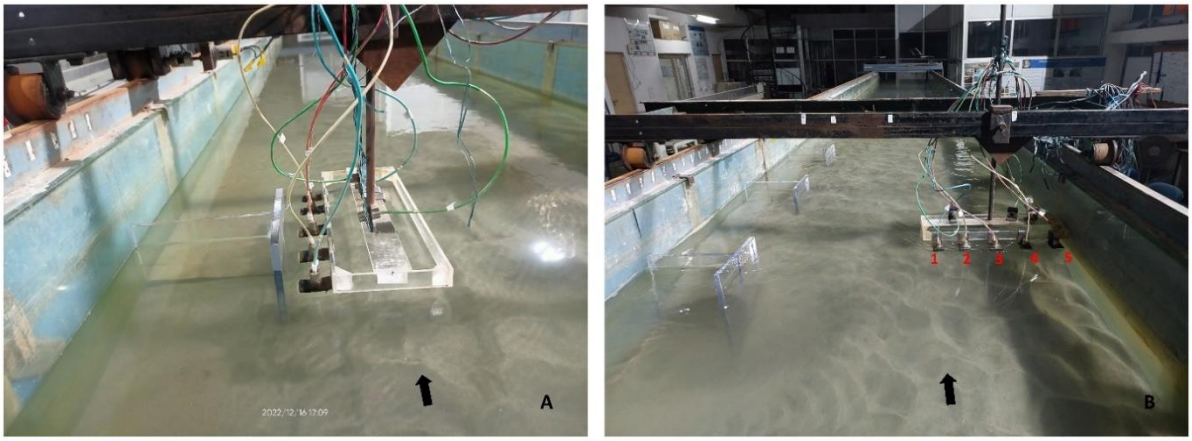

Figure 2.12 Temporal variation of bed morphology using URS

2.8 Scale effect

In this study, we did not consider the impact of the thickness of the spur dike. Instead, we used a wooden plywood and an acrylic sheet, both with a 10 mm thickness, and a width (*b*) of 0.126

m and 0.20 m, respectively, as spur dikes. This approach aligns with standard experimental practices. For example, in a recent study, Aung et al. (2023) used a plexiglass plate as a spur dike with a thickness of 10 mm and a width of 0.25 m. Pandey et al. (2016) used a rectangular plate with a thickness of 2 mm and various widths, and Gisonni and Hager (2008) examined impermeable plates with a thickness of 5 mm and different widths. Moreover, Oliveto and Hager (2005) pointed out that the effect of the thickness of an abutment on the processes of local scour is considered relatively insignificant.

Regarding approach flow, it is crucial to highlight that the Reynolds number in our study was significantly high, surpassing 10^4, indicating turbulent flow conditions. Furthermore, we maintained a distance of 8.5 m between the initial spur dike and the channel inlet, ensuring sufficient space to develop a fully turbulent flow.

To minimise sidewall effects, the study consistently maintained a channel width to approaching flow depth ratio above five, in accordance with recommendations (Aung et al., 2023; Dey & Raikar, 2005). Specifically, the determined ratio in our study was 5.4 (with bank) and 7.4 (without bank), demonstrating a careful alignment with established guidelines.

In terms of contraction scour effects, another critical consideration was maintaining the width of the element in comparison to the undisturbed channel width within the range of 10% to 20% to prevent contraction scour (Oliveto and Hager, 2002). While this study had a slightly larger ratio of 21.9% (with bank) and 20% (without bank), it is noteworthy that no observable contraction-scour effects were encountered.

2.9 Experimental programme and spur dikes Arrangement

The experimental program consisted of a series of experiments in an experimental flume to understand the flow pattern and bed morphology around different shapes of spur dikes, as well as their permeability and orientations in alluvial channels. For each experimental objective, a

series of three experiment sets (no-seepage, Seepage velocities V_{S1} and V_{S2}) were conducted with constant discharge and flow depth. Experimental details and flow properties are given in Table 2.4.

2.9.1 Experimental Study on the Optimal Spur Dike Shape under Downward Seepage

Three shapes of spur dikes, namely T-shape, L-shape, and Rectangular-shape, were individually installed, as shown in Figure 2.13. Each experimental setup for a specific shape of spur dike consisted of three spur dikes arranged in series, creating a field of spur dikes within the test section. While previous studies have primarily examined single spur dikes, combining multiple spur dikes holds greater promise for river protection (Nayyer et al., 2019).

Each spur dike in this study had a projected length of 12.6 cm, with its wing length matching the projected length (L/L' = 1). Spur dikes were spaced in series with a spacing factor of 3.96, representing the ratio of the spacing between spurs to the extended length of the spur (Richardson et al., 1975). The channel in this research had a single-sided bank inclined at a 45-degree angle. The non-submerged spur dikes were positioned perpendicular to the bank and projected outward in various shapes and configurations. These spur dikes possessed an overall height of 28 cm; 15 cm extended above the sediment bed, while the remaining 13 cm submerged beneath it. Figure 2.14 displays the test section of the experimental bed before the experimental run.

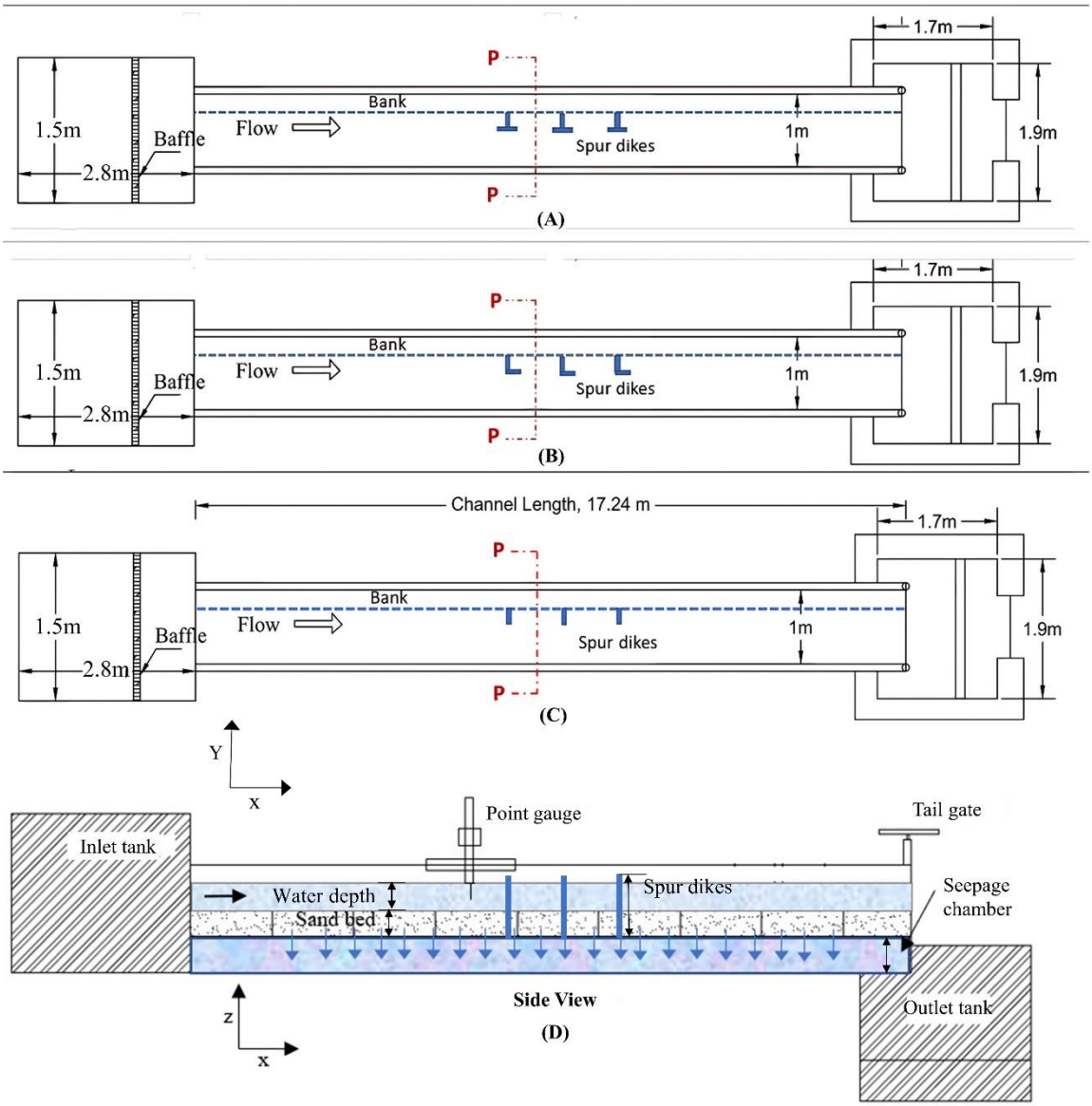

Figure 2.13 The experimental setup with different shapes of spur dikes in plan view projection: T-shape (a), L-shape (b), and Rectangular-shape (c), along with side view (d).

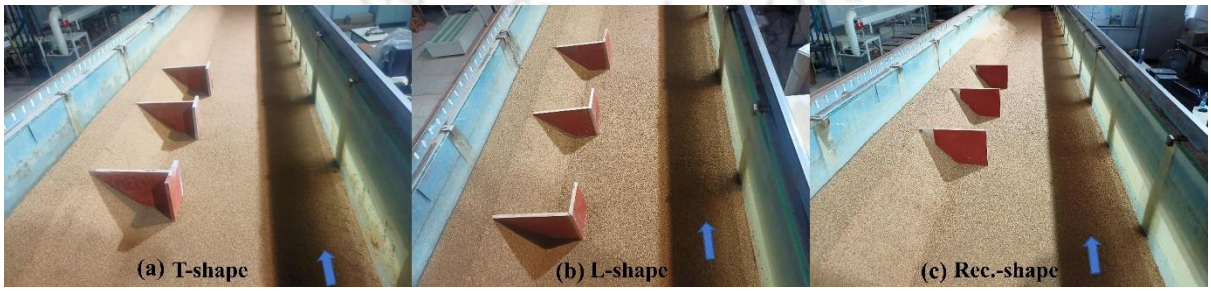

Figure 2.14. Experimental bed conditions before run with different spur dike shapes, T-shape (a), L-shape (b), and rectangular shape (c).

2.9.1.1 Velocity measurement around different shapes of spur dikes

The study measured instantaneous velocity at 25 specific locations with the grid of 7 different longitudinal sections (*A*-*G*) and four different transverse sections (1–4), as depicted in Figure 2.15. At every transverse section, 3–4 locations were chosen. For the longitudinal section *A*, the position is marked as *A*1, *A*2, *A*3, and *A*4. Similarly, it is marked for other section points. Section 1 is fixed near the edge of the left-sided bank (at 0.68 m from the right bank), section 2 (at 0.56 m from the right bank), Section 3 (at 0.42 m from the right bank), and section 4 (at 0.20 m from the right bank). Whereas three crucial points, *B*2, *D*2, and *F*2, were fixed at the wing edge of the spur dike, these locations were chosen due to previous research identifying the maximum scour depth variation (Vaghefi et al., 2009).

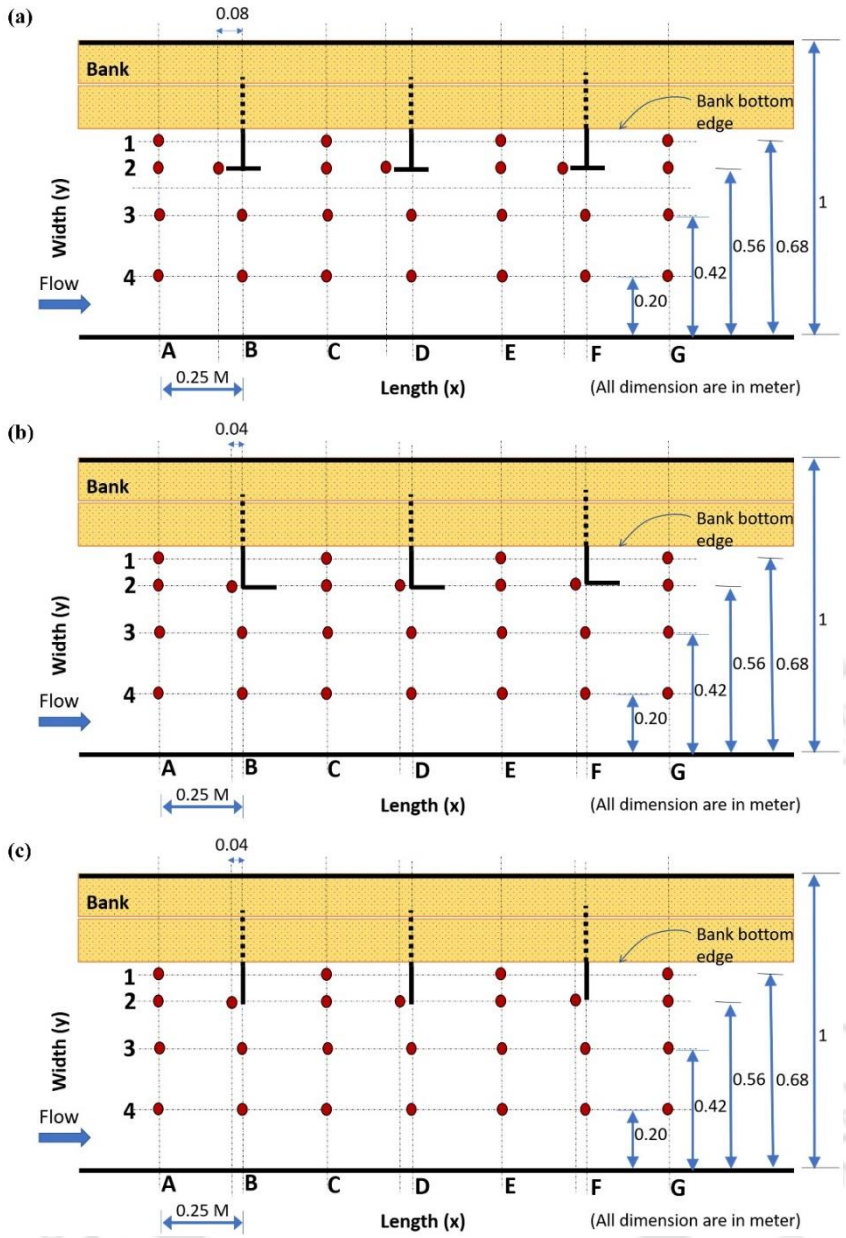

Figure 2.15 Velocity measurement points locations in the test section under various spur dike shapes.

2.9.2 Channel Morphology with Permeable Spur Dikes under Downward Seepage

Three sets of experiments, Set-A, Set-B, and Set-C, were utilised to investigate the impact of permeability on scour formation, bed morphology, and flow pattern (Figure 2.16). These spur dikes were placed on the one-sided wall, extending outward. For each set, different combinations of permeable and impermeable spur dikes were used, as shown in Figure 2.17. Set-A included three impermeable spur dikes arranged in series. Set-B had the first spur dike

with 60% permeability, while the others remained impermeable. Set-C combined 60% permeability for the first spur dike and 30% for the second and third spur dikes, which were arranged as impermeable. Each experimental set is analyzed under three different seepage conditions, i.e., seepage velocities V_{S1} and V_{S2} and a no-seepage condition. Figure 2.18 displays the test section of the experimental bed before the experimental run.

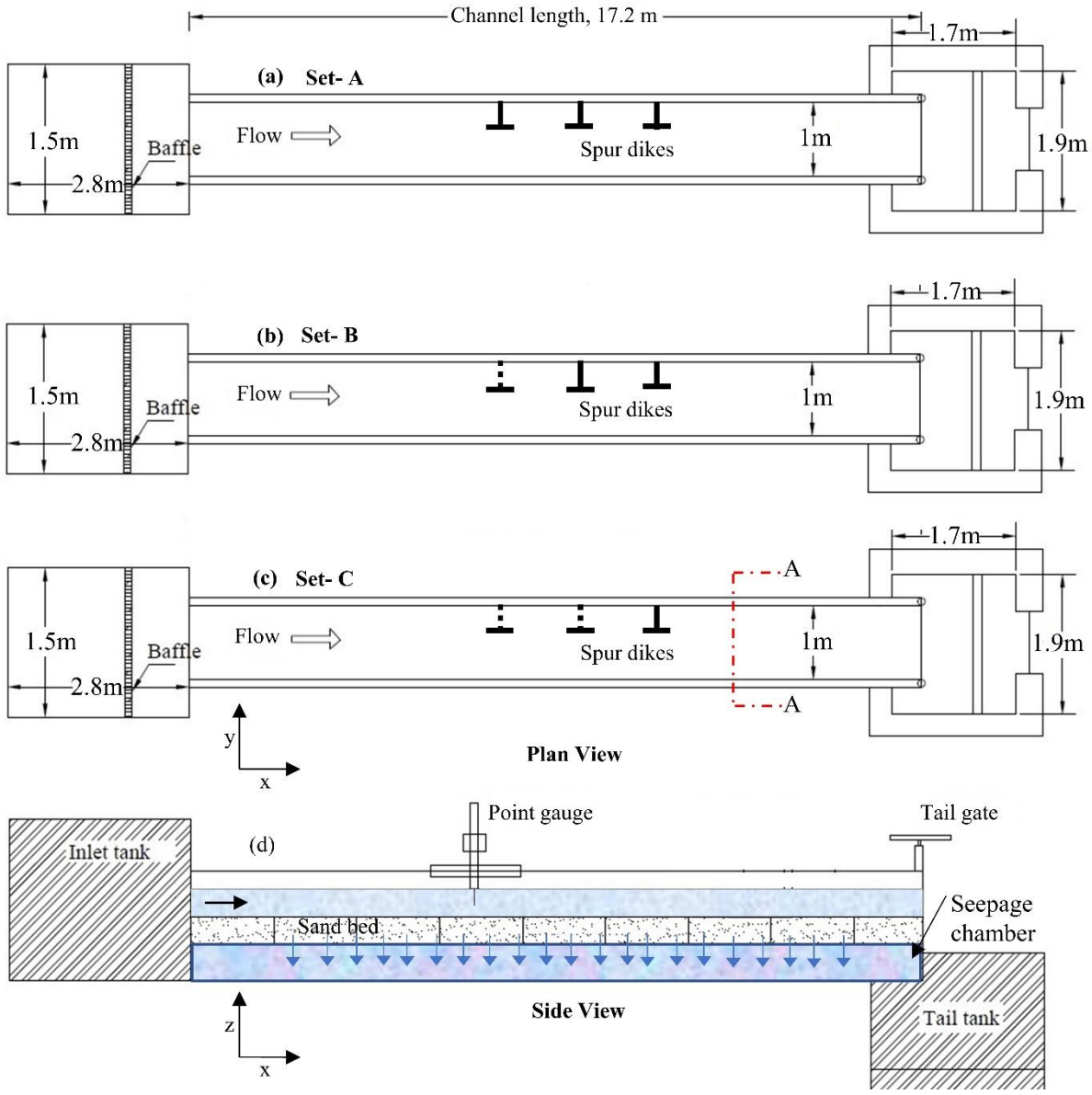

Figure 2.16 Experimental setup in plan and side view projections with different permeability sets of spur dikes: Set-A (a), Set-B (b), Set-C (c), along with side view (d).

In each experiment, three spur dikes were arranged in series, creating a comprehensive field of spur dikes within the designated test section. This approach differs from conventional studies

on single spur dikes and holds significant promise for river protection. The entire length of the channel is made up of a sediment bed with a thickness of 22 cm. We kept a distance of 8.5 m between the initial spur dike and the channel inlet to allow for the complete development of turbulent flow. These spur dikes had an overall height of 36 cm; 15 cm extended above the sediment bed, while the remaining dikes were submerged beneath it. The design dimensions of the spur dike setup are listed in Table 2.3.

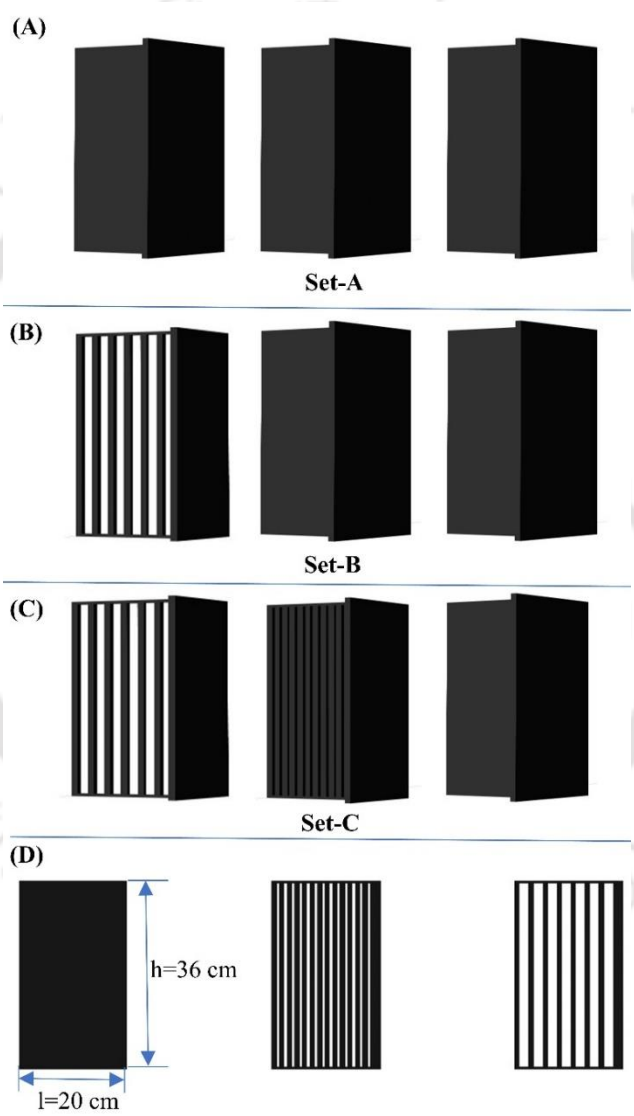

Figure 2.17 Isometric spur dike arrangement with different permeability sets of spur dikes: Set-A (A), Set-B (B), and Set-C (C), along with the side view (D).

Table 2.3. Spur dike dimensions

Spur dike arrangements

Spur dike length (Projected), L	0.2	m
Spur dike height, h_S	0.36	m
Spur dike width (wing), L'	0.2	m
Spacing between spurs, ΔS	0.6	m
Spurs orientation, θ	90	degree

Figure 2.18 Experimental bed conditions before run with different sets of permeable spur dikes, Set-A (a), Set-B (b), and Set-C (c).

2.9.2.1 Velocity measurement around different sets of permeable spur dike

The instantaneous velocity was measured at 28 specific points, as shown in Figure 2.19. Turbulent flow in horizontal planes was studied to determine its pattern. One plane, located close to the water surface at a height of z/h = 0.50, played a crucial role in replicating the complex water movements around permeable spur dikes within the channel.

Additionally, to examine the occurrence of scour depth, this study paid particular attention to location A_1 (at z/h = 0.05**)**, which represents the channel's bottom and is strategically situated at the wing edge of the spur dike. Velocity profiles were drawn for this specific location to analyze the effect of permeability and downward seepage conditions. This selection was based on prior research pinpointing it as a significant area exhibiting maximum variation in scour depth (Vaghefi et al., 2009; Patel & Kumar, 2023, 2024).

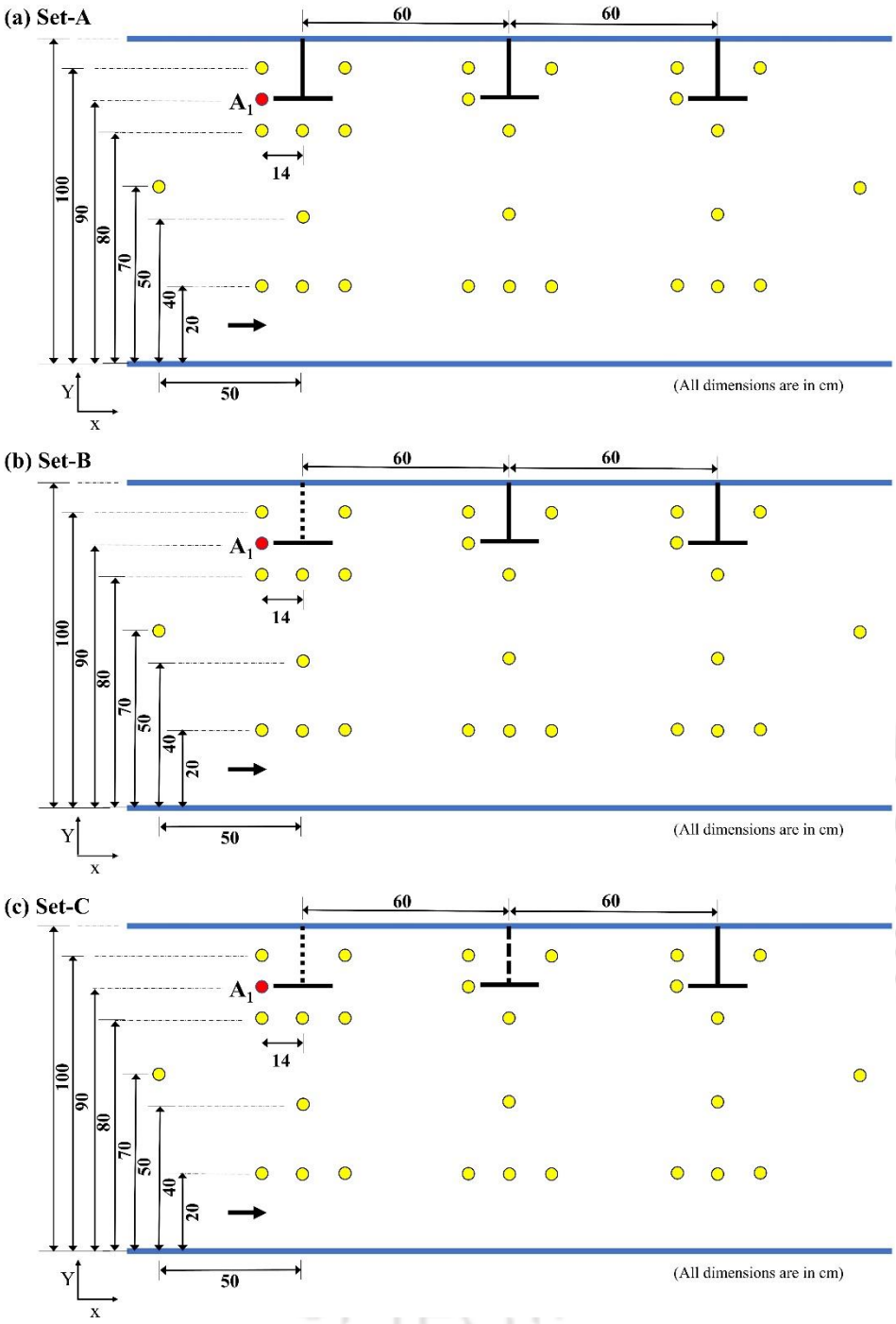

Figure 2.19 Velocity measurement points locations in the test section under various permeable spur dike combinations.

2.9.3 Optimal Spur Dike Orientation for Scour Mitigation under Downward Seepage Conditions

The methodology and experimental setup involved a series of experiments conducted in an experimental flume of straight rectangular channels. The configuration of this experimental

flume is visually represented in Figure 2.20. The study concentrated on optimising three distinct angles of spur dikes, specifically, 60º, 90º, and 120º, while analysing the development of scour depth over time. The analysis was conducted at 2, 12, and 24-hour intervals under a no-seepage condition. The ultimate evolution of scour after 24 hours was subsequently compared to conditions where downward seepage was applied. Figure 2.21 displays the test section of the experimental bed before the experimental run.

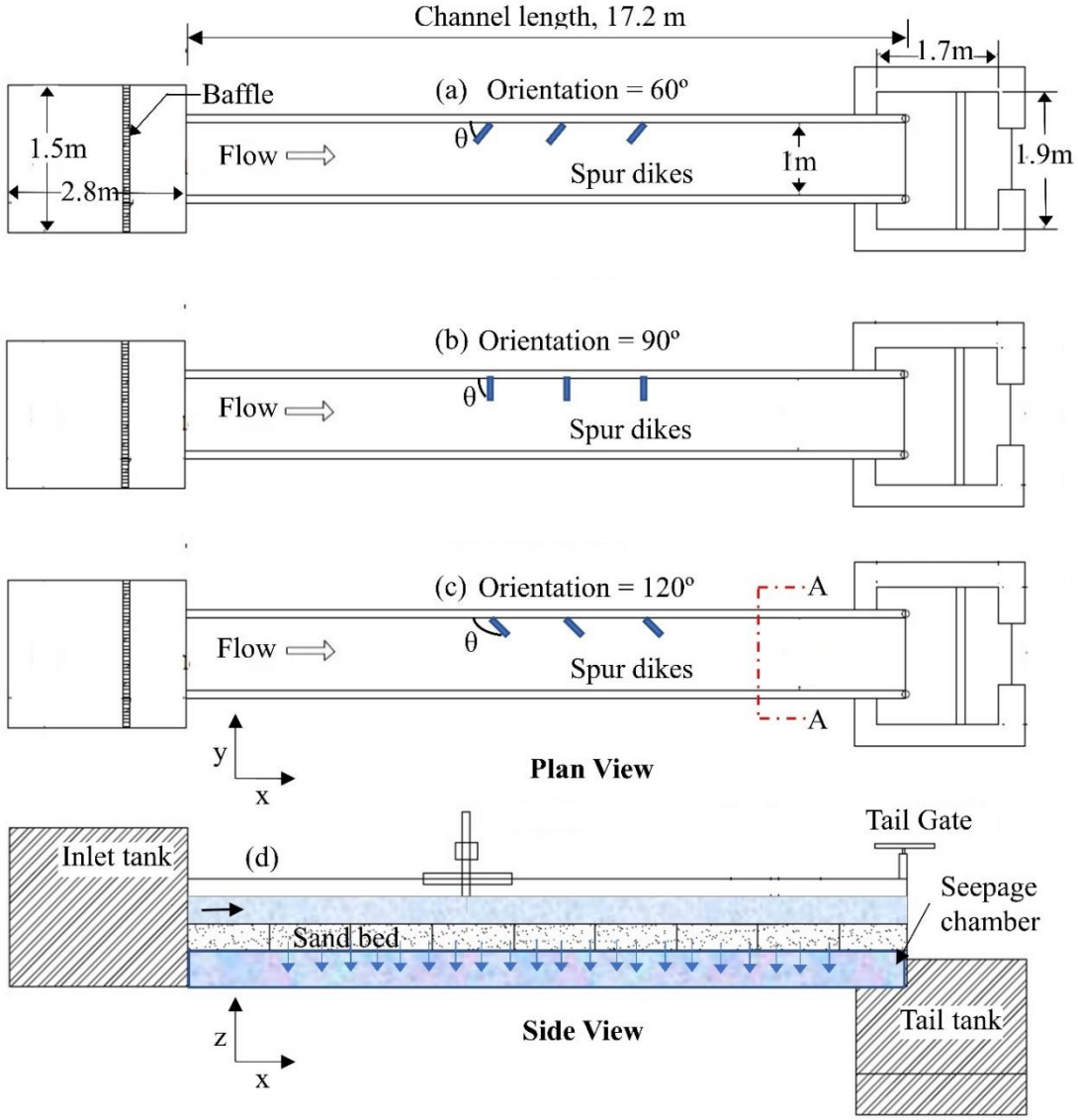

Figure 2.20 The experimental configuration featuring oriented spur dikes in a plan view, displaying variations at (a) 60°, (b) 90°, and (c) 120°, along with (d) a side view.

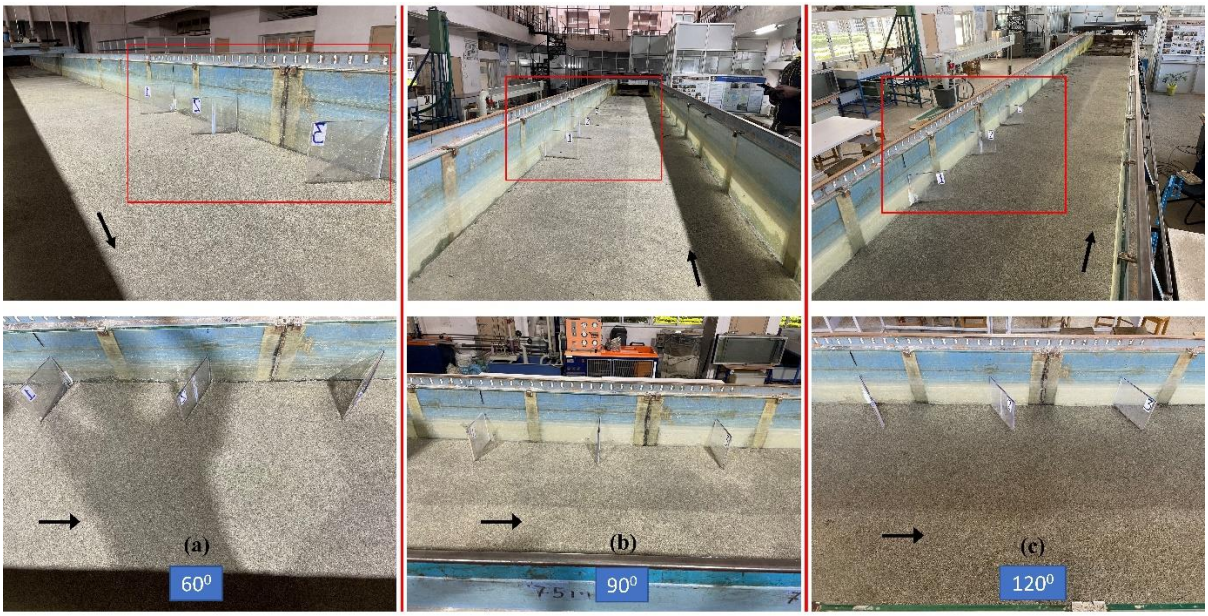

Figure 2.21 Experimental bed conditions before run with different spur dike orientations, 60° (a), 90° (b), and 120° (c).

2.10 Multiscale characteristics of scour depth migration

Scour rate migration was observed between *P*-*Q* and *P*-*R*, which were located 30 cm and 130 cm apart, respectively as shown in figure 2.22. Our analysis focuses on studying the impact of seepage on sediment movement at the first spur dike and compares it to the entire field of spur dikes. The dataset for locations *P*-*Q* specifically looks at the erosion rate near the first spur dike, while the dataset for locations *P*-*R* covers the erosion rate across the entire field of spur dikes. This setup was installed near the spur dike tip $Y = 50$ cm to collect data. The arrangement of transducers is attached to a moving trolley and can be moved to the desired location. The data collection was performed for 5 min for each time interval of 0, 2, 6, and 12 h for each location, i.e. *P*, *Q* and *R* for each no-seepage, seepage velocities run. Furthermore, this recorded data was used to analyse the bed elevation changes and temporal and spatial scale celerity.

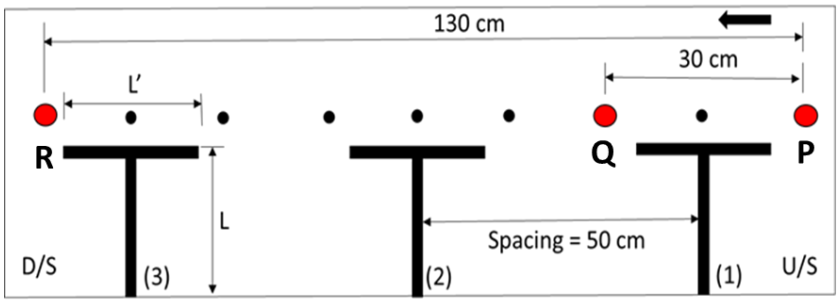

Figure 2.22 measuring points of bed elevation and multiscale celerity.

Table 2.4 Description of experimental parameters and flow properties

Flow Properties	**Objective**			
	1		**2**	**3**
	With bank		**Without bank**	
Flow rate (Q) m^3/s	0.023	0.03	0.03	
Seepage condition (NS, V_{S1}, V_{S2}) mm/s	V_{S1} = 0.071, V_{S2} = 0.143	V_{S1} = 0.09, V_{S2} = 0.18	V_{S1} = 0.09, V_{S2} = 0.18	V_S = 0.18
Avg. Flow depth (y) m	0.128	0.13	0.135	0.13
Mean velocity (V) m/s	0.226- 0.246	0.303-0.334	0.222	0.23
Froude number (Fr)	0.19-0.22	0.27-0.30	0.18-0.20	0.20-0.21
Reynolds number (Re)	22525-23070	29694-32732	23511-23697	23730-23847
Sediment				
Sediment size (d_{50}) mm	1.1		0.23	
Standard deviation (σ_g)	1.03		0.79	
Specific gravity (G_s)	2.65		2.65	
Angle of repose (θ_r)	θ_r = 31.5°		θ_r = 35°	
Bank angle (θ_b)	45°		No-bank	
Channel bed slope, (S_o)	1/526.3			
Spur dike				
Spur Shape				
Material used	Wooden		Acrylic	
Permeability	Impermeable		Permeable Set-A (0,0,0) % Set-B (60,0,0) % Set-C (60,30,0) %	Impermeable
Projected length (cm)	12.6		20	
Spacing factor	3.96		3	
Orientation (θ)	90°		90°	60°, 90°, 120°

3 Experimental Study on the Optimal Spur Dike Shape under Downward Seepage[3,4,5,6]

3.1 Introduction

The scouring in the channel can affect the strength of the spur dike or any structure, making it prone to failure (Pandey et al., 2019). To prevent this, engineers must consider the maximum expected scouring depth around the spur dike during construction. However, predicting the exact scour depth remains challenging (Pandey et al., 2021a). Predicting and estimating the maximum depth of scour around spur dikes, as well as understanding the factors contributing to it, are essential for the efficient and risk-free construction of spur dikes (Rahman & Muramoto, 1999; Mohammadpour et al., 2016; Pandey et al., 2016, 2018, 2021b; Wang et al., 2017; Tripathi & Pandey, 2022; Fuladipanah, et al., 2023).

Regarding the configuration of spur dikes, there are several plan view shapes to choose from, including straight (rectangular), straight dikes with pier heads, L-head, T-head, hockey stick or curved dikes, and inverted hockey stick spur dikes. At specific river segments, all designs serve one purpose: preventing banks from erosion.

Regarding cost and ease of construction, spur dikes in rectangular shapes are the most cost-effective and straightforward. Due to its ease of installation, this design has drawn considerable

3 Patel, H. K., & Kumar, B. (2023). Hydro-morphological behavior around T-shaped spur dikes with downward seepage. Scientific Reports, 13(1), 10454. doi.org/10.1038/s41598-023-37694-w

4 Patel, H. K., Arora, S., Chavan, R., & Kumar, B. (2024). Migrating Scour Depth around a Spur Dike with Downward Seepage Using Multiscale Characterizations. Experimental Thermal and Fluid Science, 151, 111071. doi.org/10.1016/j.expthermflusci.2023.111071

5 Patel, H. K., Qi, M., & Kumar, B. (2023). Downward seepage effects on flow near a L-shape spur dike and bed morphology. International Journal of Sediment Research, 39(2), 194-208. doi.org/10.1016/j.ijsrc.2023.11.005

6 Patel, H. K., & Kumar, B. (2023). Experimental Study on the Optimal Spur Dike Shape under Downward Seepage. Water Science, 38(1), 172-191. doi.org/10.1080/23570008.2024.2321423

attention from researchers. As a result, rectangular spur dikes have been widely utilized in research studies exploring flow characteristics around these structures. Various researchers (Ezzeldin et al., 2007; Duan, 2009; Yazdi et al., 2010; Duan et al., 2011; Koken & Gogus, 2015; Jeon et al., 2018; Kang, 2018; Indulekha et al., 2021; Iqbal et al., 2021; Jafari & Sui, 2021; Kafle, 2021; Kang et al., 2021b; Lodhi et al., 2021; Mulahasan et al., 2021; Pandey et al., 2022; Pourshahbaz et al., 2022), have employed rectangular spur dikes to investigate scouring process and analyze flow characteristics around these river training structures.

Previous research has shown that L-shaped spur dikes effectively prevent riverbank erosion. These structures successfully divert water flow away from the riverbank and, as a result, reduce the depth of scouring. Studies (Kadota et al., 2010; Masjedi et al., 2011; Dehghani et al., 2013; Mojtahedi & Basmenji, 2017; Kumar & Ojha, 2019, 2021) have highlighted the positive impact of L-shaped spur dikes in mitigating erosion and protecting the stability of the riverbank.

In contrast to previous studies, recent research over the past decade has consistently indicated that the T-shape configuration of spur dikes exhibits the least amount of scouring when compared to other geometric shapes (Safarzadeh et al., 2016; Vaghefi et al., 2016b, 2018,2019; Mehraein et al., 2017; Tripathi & Pandey, 2021; Patel & Kumar, 2023). The findings from these multiple studies converge on the conclusion that the T-shaped design of spur dikes offers significant advantages in minimizing scouring. Safarzadeh et al. (2016) investigated the three-dimensional turbulent flow field around a single straight and two different T-shape spur dikes (with shorter and longer wing lengths) under smooth flat-bed conditions. They have concluded that the strong horseshoe vortex forms close to the spur dike base in the single straight spur dike. In contrast, the horseshoe vortex in a T-shape with a shorter wing length spur dike is weaker than in a single straight spur dike and completely disappears for a T-shape with a more extended wing length spur dike.

Despite exploring various spur dike shapes and combinations to achieve local scour reduction, their practical implementation remains limited. Researchers also investigated alternative configurations to understand their effectiveness in reducing scouring around spur dikes. Bahrami-Yarahmadi, et al. (2020) used a triangular-shaped spur dike to analyze the scour pattern development around it. Their findings suggested that the triangular shape has the potential to minimize scouring from the spur dike tips, indicating its potential effectiveness in erosion mitigation.

In a study, Masjedi et al. (2010) evaluated the influence of various wing shapes in T-shape spur dikes. Their research found that the oblong wing design had the least scour, about 20% less than the rectangular wing shape. Furthermore, the scour depth around the rectangular chamfered wing shape was smaller than the basic rectangular spur dike. According to El-Rashedy et al. (2018), discharge and Froude number influence scouring processes around straight, hockey, molehead, L shape, and T shape dikes. According to the results of the studies, the hockey shape spur dike was very successful in minimizing scour depth.

Based on a comprehensive examination of the available literature, numerous research studies have delved into the scour patterns that occur around particular shapes of spur dikes. Past research demonstrated that various shapes of spur dikes could help prevent riverbank erosion by redirecting the water's flow away from the structures and reducing scour depth. However, the existing literature does not comprehensively evaluate how these spur dike shapes influence scouring processes while considering a critical factor such as seepage. This study aims to bridge this gap by optimizing the suitable spur dike shapes based on scour depth evolution, considering the influence of downward seepage. The study's findings will be crucial for selecting the right spur dike shape in the early stages of river engineering projects.

3.2 Experimental conditions

The investigation focused on three distinct spur dike shapes T-shaped, L-shaped, and rectangular shaped under two different discharges of 0.023 m³/s and 0.030 m³/s. For each discharge, three seepage conditions were applied. At a discharge of 0.023 m³/s, the conditions included no seepage and seepage velocities of V_{S1} = 0.071 mm/s and V_{S2} = 0.143 mm/s. Similarly, at a discharge of 0.030 m³/s, the conditions included no seepage and seepage velocities of V_{S1} = 0.09 mm/s and V_{S2} = 0.18 mm/s. The average flow depth observed was 0.128 m for a discharge of 0.023 m³/s and 0.13 m for a discharge of 0.030 m³/s. Additional experimental details are provided in Table 2.4.

3.3 Scour depth variation and channel bed morphology

Figure 3.1 illustrates changes in the shape of the riverbed within the test section. The research findings highlight seepage's substantial influence on the alluvial channel's overall configuration. Seepage intensifies the bed particle movement, and when it is more pronounced, it leads to an increased detachment of these particles. This, in turn, results in the formation of deeper hollows in the riverbed, known as scour depressions. The investigation found the most significant local scouring around the tip of the first spur dike wing (spur-1). Minor hollows, on the other hand, were spotted near the second and third spur dikes. This disparity in scour depth can be traced to how the streamflow behaved as it approached the spur dikes. In particular, as the water flowed toward the first spur dike, it diverted from its edge, leading to greater scouring in front of it than the subsequent dikes. Sediment eroded from the first spur dike tended to concentrate towards the location of the third spur dike in all of the scenarios evaluated. This accumulation resulted in a sand-dune-like structure next to the third dike. The longitudinal scouring in the riverbed expanded when the seepage rate grew stronger.

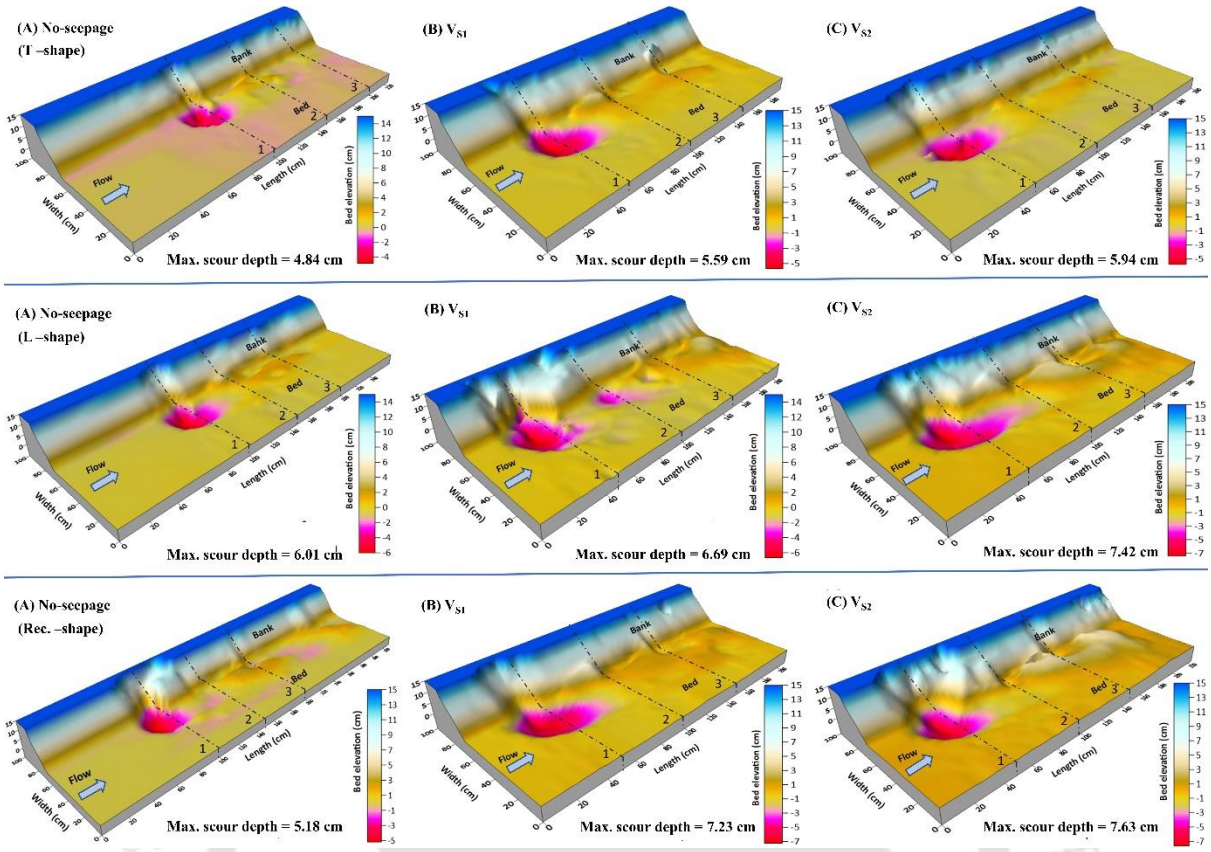

Figure 3.1 Maximum scour depth and surrounding bed morphology under various spur dike shapes and seepage conditions.

Measurements were conducted on three spur shapes under three conditions: no seepage, V_{S1}, and V_{S2}. For the T-shaped spur dike, the highest scour depth was recorded at the edge of the first spur dike wing, with measurements of 4.84 cm, 5.59 cm, and 5.94 cm for conditions without seepage, V_{S1}, and V_{S2}, respectively. This variation shows a proportional increase in maximum scour depth with rising seepage. Specifically, the application of V_{S1} led to a 15.5% elevation in maximum scour depth, while V_{S2} resulted in a 22.7% increase compared to the no-seepage scenario.

Similarly, for the L-shaped spur dike, the maximum scour depth was measured at the corner where both arms of the L-shape converge, at 6.01 cm, 6.69 cm, and 7.42 cm for no seepage, V_{S1}, and V_{S2}, respectively. Seepage also had a significant impact here, with a maximum scour depth increase of 11.3% for V_{S1} and 23.4% for V_{S2} relative to the absence of seepage.

In the case of the Rectangular-shaped spur dike, the maximum scour depth was recorded at the edge of the vertical arm, with measurements of 5.18 cm, 7.23 cm, and 7.63 cm for conditions without seepage, V_{S1} and V_{S2}, respectively. Seepage induced a substantial increment, with a growth of 39.5% for V_{S1} and 47.2% for V_{S2} compared to the no-seepage scenario.

In the absence of seepage, in comparison with other shapes, the greatest scour depth was noted around the L-shaped spur dike-1, which exceeded the scour depths of the Rectangular and T-shaped spur dikes by 16% and 24.1% at the same position. However, upon the introduction of seepage, for V_{S1}, the maximum scour depth occurred in the Rectangular-shaped spur dike, surpassing the L-shaped and T-shaped counterparts by 8% and 29.3%, respectively. A similar trend emerged with increased seepage velocity (V_{S2}), where the maximum scour depth was highest in the Rectangular shape, exhibiting a 3% and 28% increase compared to the L-shaped and T-shaped spur dikes, respectively.

In summary, the outcomes underscore the substantial impact of seepage on maximum scour depth, revealing that increased seepage rates correspond to more extensive scouring: channel morphology and bed configuration experience greater distortion in the presence of seepage. Moreover, the shape of the spur dikes plays a pivotal role in shaping the entire field's morphology when downward seepage is involved. Downward seepage influences the hydrodynamic processes around different shapes of spur dikes, impacting flow patterns, turbulence, and sediment transport. The specific effects vary based on the geometric configuration of the dike, with T-shaped, L-shaped, and rectangular-shaped dikes exhibiting distinct responses to seepage, ultimately influencing scour depth near the dikes.

In the context of T-shaped dikes, downward seepage interacts with the streamlined flow created by the dike, actively contributing to maintaining the equilibrium of sediment particles. This equilibrium restricts the displacement of particles, mitigating the scouring potential near the

dike. For L-shaped dikes, seepage induces energy redistribution, influencing sediment transport patterns. The specific geometry of the dike plays a crucial role in determining the nature of this redistribution and, consequently, impacts the scour depth in the vicinity. In the case of rectangular-shaped dikes, the forceful obstruction of flow, coupled with downward seepage, intensifies the detachment of sediment particles from the riverbed. This heightened sediment transport significantly alters the scour depth around the dike.

Across all dike shapes, downward seepage accelerates the detachment of sediment particles from the base of the dikes. This detachment is a common mechanism enhancing sediment transport and scouring processes.

3.3.1 Longitudinal scour depth

Figure 3.2 depicts how scour depth varies along the length of the channel near a spur dike. For a given flow rate and seepage condition, data on the bed surface were gathered in the downstream direction at the tip of the spur dike (at 0.56 m from the right bank). When water currents meet a series of spur dikes, they create an obstruction that shapes a curved wave resembling a bow on the water's surface (Daneshfaraz et al., 2023; Norouzi et al., 2023). This wave makes water move downward toward the structure's base. Thus, it creates a horseshoe-shaped vortex at the edge of this obstruction (Zhang & Nakagawa, 2008; Ezzeldin, 2019). Alongside, a complex swirling water pattern, referred to as a "vortex system," emerges along the spur dike's boundary. These swirling currents and vortices are critical for removing silt from the bottom of the structure. As a result, the sediment loosens and is carried downstream by the primary current. This detached material then gathers and settles downstream areas (particularly between the second and third spur dikes), where the flow velocity is noticeably slower. The variation in dune formation with no seepage is linked to the findings of Roushangar et al. (2024), who observed that the eddy current in the area of the spur dikes created dunes

with a height proportional to the scour depth in its vicinity. These variations result from how water flows around the base of different shapes.

The formation of the horseshoe vortex is found to be weak at the base of the T-shape spur dike compared to other shapes. These findings are consistent with earlier research by Safarzadeh et al. (2016). Additionally, the study revealed that scour depth variations are significant, particularly at higher seepage velocities. This theory is consistent with Jahan (2014) findings, which found that, compared to no suction, 5% and 10% suction increased equilibrium scour depth by about 23% and 42%, respectively. The particular shapes of the spur dikes have an important role in changing flow patterns, resulting in sediment transport, erosion, and deposition in specific areas downstream of the spur dike arrangement.

3.3.2 Temporal scour evolution

Figure 3.3 represents the change in scour depth over time for varied seepage situations. According to the findings, the deepest scour occurs near the pointed end of the first spur dike. The scour forms quickly during the first 6-8 h, then gradually increases until it stabilises after around 18 h. This pattern holds across all the spur dike shapes evaluated in this study. However, when a T-shaped spur dike is used, scour develops slower than the other types. The scouring process steadily intensifies with the T-shaped design until it reaches equilibrium.

In contrast, the rate of scour depth development is higher with the L-shape of the spur dike with the absence of seepage. As seepage was applied, the scour rate was significantly enhanced around all shapes until it attained equilibrium, and the scour depth changed with a higher rate with an L-shape and rectangular shape spur dike. In summary, this study emphasises the need to account for seepage's impact on spur dike scour depth. Understanding the temporal evolution of scour depths and the variation in response to different spur dike shapes is essential for designing irrigation systems that can effectively manage seepage and ensure long-term efficiency and sustainability.

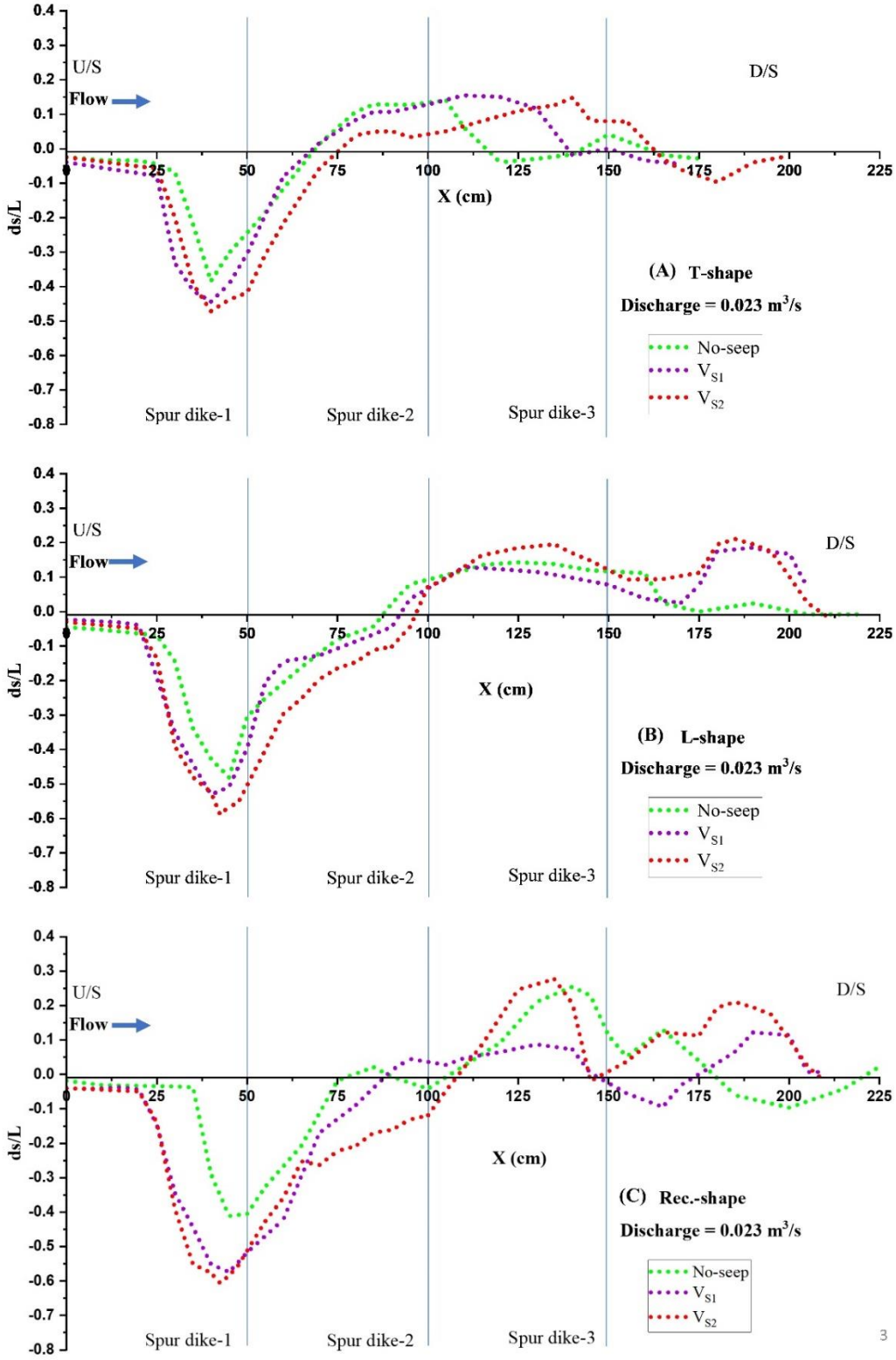

Figure 3.2 Longitudinal variation of scour formation under various spur dike shapes and seepage conditions. Here, the maximum scour depth (*ds*) is non-dimensionalized with the projected length of the spur dike (*L*).

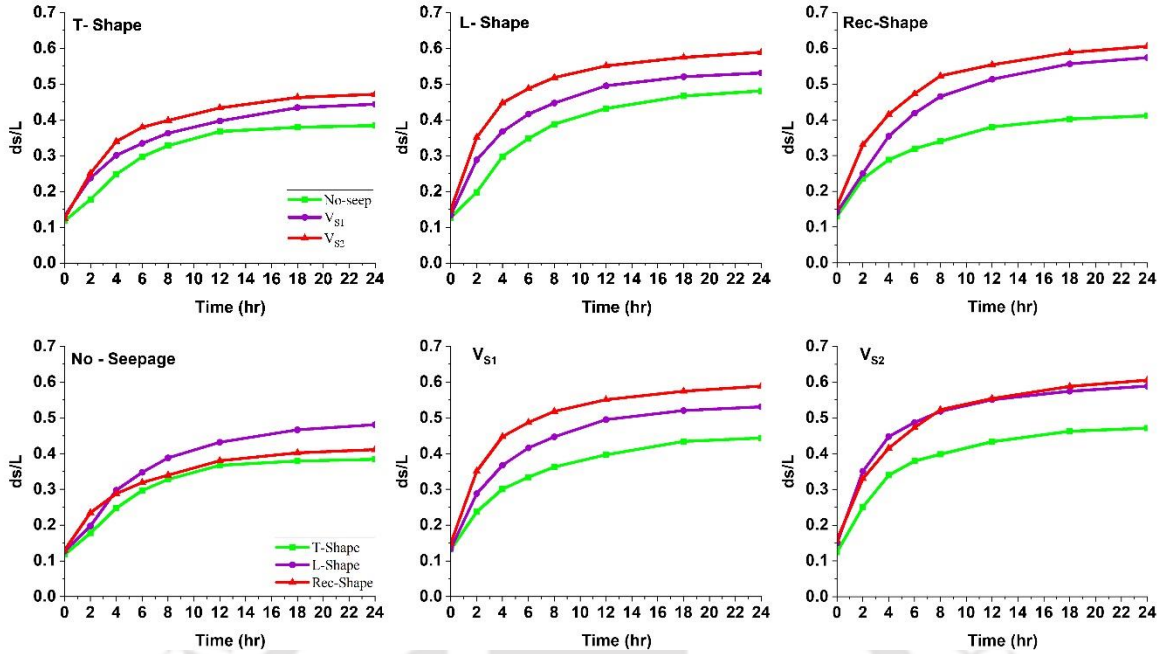

Figure 3.3 Evolution of scour depth over time under various spur dike shapes and seepage conditions.

3.4 Velocity

In the context of this experimental analysis, we examine two distinct areas: the primary flow zone (main flow zone) and the obstacle zone. These regions play a critical role in understanding the dynamics of the flow pattern. The primary flow zone comprises the region with the most noticeable flow. This area extends from y = 0 cm to y = 56 cm and is the space through which the incoming flow converges. In this zone, water movement rapidly increases through the wing edge of spur dikes. These spur dikes divert the flow, leading to convergence within the main flow zone. This convergence produces a unified stream of water that flows through the defined location.

Conversely, the obstacle zone extends from y = 56 cm to y = 85 cm. The spur dikes perform a different role in this region. These constructions obstruct and impede water movement rather than assisting it. As a result of the presence of the spur dikes, the flow inside the obstacle zone

is constrained and altered. This zone has a distinct flow behaviour compared to the main flow zone because the obstructions greatly influence the flow dynamics.

A series of contour plots in Figure 3.4 illustrates the streamwise velocity distribution near the water's surface, particularly at a depth of $z/h = 0.50$. These plots provide a better understanding of the complicated flow dynamics by showing how spur dike zones influence the flow velocity. To further understand how water flow influences scour formation, we focused on three crucial locations along spur dikes where the deepest scouring occurred. Our research found that the most substantial alterations in flow patterns occurred around the first spur dike. As a result, our primary investigation focused on the area surrounding the first spur dike of each shape to determine the causes of these flow fluctuations and their impact on scouring.

For T-shaped spur dikes near the first one, velocity increases by 5.2% (V_{S1}) and 11.1% (V_{S2}) compared to no seepage. Similarly, L-shaped spur dikes see a 14% (V_{S1}) and 45% (V_{S2}) velocity increase, while Rectangular-shaped spur dikes experience 16% (V_{S1}) and 48% (V_{S2}) velocity increases. Experimental data highlights that maximum velocity magnitude occurs around Rectangular-shaped dikes, and seepage amplifies this effect. Conversely, weaker velocity magnitude is seen near T-shaped dikes, which strengthens with seepage.

Without seepage, L-shaped and Rectangular-shaped dikes have 26% and 41% higher velocities than T-shaped ones. For V_{S1}, increases are 37% (L-shaped) and 56% (Rectangular-shaped), and for V_{S2}, increases are 65% (L-shaped) and 88.7% (Rectangular-shaped) than T-shaped. This consistent trend indicates that higher seepage leads to more significant velocity variation, notably around Rectangular-shaped dikes.

Observing the water's surface at a depth of $z/h = 0.50$ reveals that the greatest velocity intensity is centred around the initial spur dike. The flow intensity steadily reduces downstream through the successive spur dikes (2 and 3). This pattern is consistent across all scenarios involving

different spur dike shapes. This effect becomes particularly pronounced when seepage rates are introduced.

A distinctive pattern is associated with the flow as it encounters the spur dike zones. In response to the flow's interaction with the wing edges of the spur dike, which are placed in the direction of the incoming flow, the flow is redirected and constricted. As a result of this interaction, the flow velocity within the main flow zone increases significantly. As velocity increases, it tends to scatter and expand longitudinally. The maximum velocity can be seen in this wing edge area of the spur field. After passing through the spur dike field, the flow velocity decreases as the flow passes through all the spur dikes.

This change leads to an area behind and between spur dikes, where velocity reaches its lowest, possibly even going negative. This specific region is called the obstruction zone, where the spur dikes disrupt the natural flow pattern, causing slower or even flow reversal.

In addition, it is interesting to note how seepage impacts flow. In the main flow zone, where there is downward seepage, the velocity is noticeably higher than in situations without seepage. This suggests that introducing downward seepage significantly boosts flow velocity in this zone.

Figure 3.5 presents a detailed visualisation of the streamwise velocity distribution close to the channel bed, particularly near bed z/h = 0.12. These contour plots show how numerous conditions, like seepage and spur dike zones, affect flow velocity along the channel bed.

A distinctive behaviour emerges near the channel bed at z/h = 0.12, where seepage's influence is more pronounced. In the vicinity of the first spur dike near the channel's bed, there is a reversal in the velocity magnitude, characterised by a negative value. This negative effect becomes even more prominent when seepage is introduced. For the T-shaped spur dike, the

increase in velocity magnitude with V_{S1} and V_{S2} seepage velocities is 2 times and 3.5 times, respectively, compared to scenarios without seepage. This negative streamwise velocity magnitude trend also holds for other spur dike shapes. For instance, the L-shaped spur dike shows a velocity magnitude increase of 74% (V_{S1}) and 1.6 times (V_{S2}) with seepage, compared to no seepage.

Similarly, the Rectangular-shaped spur dike exhibits a velocity magnitude increase of 56% (V_{S1}) and 2.18 times (V_{S2}) with seepage, compared to no seepage. This negative impact on velocity magnitude reveals flow reversal patterns around these channel bed spur dikes. This phenomenon is closely linked to horseshoe vortices' formation and current generation. The horseshoe vortex disrupts channel flow patterns and creates a flow reversal near the bottom. Previous studies have supported this phenomenon (Qi et al., 2013; Sharma et al., 2017; Chavan & Kumar, 2020). Flow reversal causes sediment particles to loosen from the bottom of the structures and transports them via amplified lateral flow around obstacles. These factors play a pivotal role in the detachment of particles from the base of the structure. The application of downward seepage further accelerates the rate of this detachment.

Without seepage, the velocity magnitude increases 1.69 times for L-shaped and three times for Rectangular-shaped spur dikes, compared to the T-shaped spur dike. However, with seepage velocity (V_{S1}), the velocity magnitude increase for L-shaped and Rectangular-shaped spur dikes was 56% and 1.12 times, respectively, compared to the T-shaped spur dike. Similarly, for seepage velocity (V_{S2}), the velocity magnitude increase for L-shaped and Rectangular-shaped spur dikes was 56.4% and 1.88%, respectively, compared to the T-shaped spur dike. This consistent pattern underscores that as the seepage rate rises, the velocity magnitude consistently experiences an increase.

The flow velocity close to the channel's bottom is notably slow, primarily owing to the resistance offered by the bed. The contour plots clearly show that the velocity near the bed increases significantly with seepage within the main flow area. This stronger movement close to the bed plays a significant role in moving sediment swiftly in the channel. The introduction of downward seepage causes the velocity patterns to shift downward across all measurement points. The existence of seepage alters the flow pattern and the velocity distribution inside the flow significantly. The alteration in velocity distribution plays a pivotal role in the dynamics of the riverbed sedimentation. In conjunction with the shape of the dike, the presence of downward seepage increases turbulence mixing. This heightened turbulence becomes a compelling force in reshaping the structure of the riverbed. Consequently, the riverbed undergoes changes that contribute significantly to the formation of scour depth near the spur dikes.

In contrast, within the obstruction zone, the changes in velocity near the channel boundary are less significant. This region experiences relatively minor fluctuations in velocity magnitude compared to the more dynamic alterations occurring within the main flow zone.

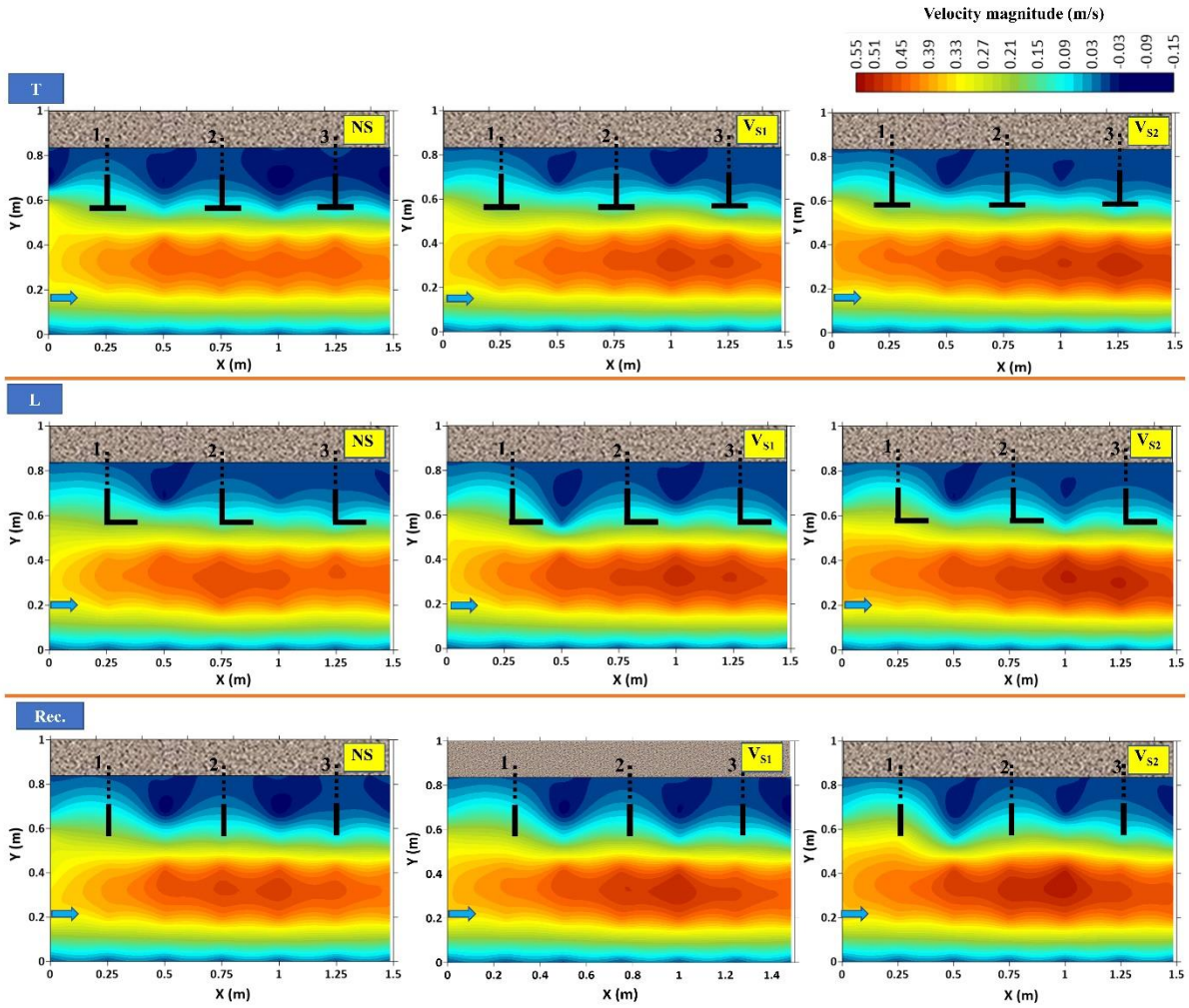

Figure 3.4 The plots of velocity magnitude in the streamwise direction, particularly near water surface z/h = 0.50.

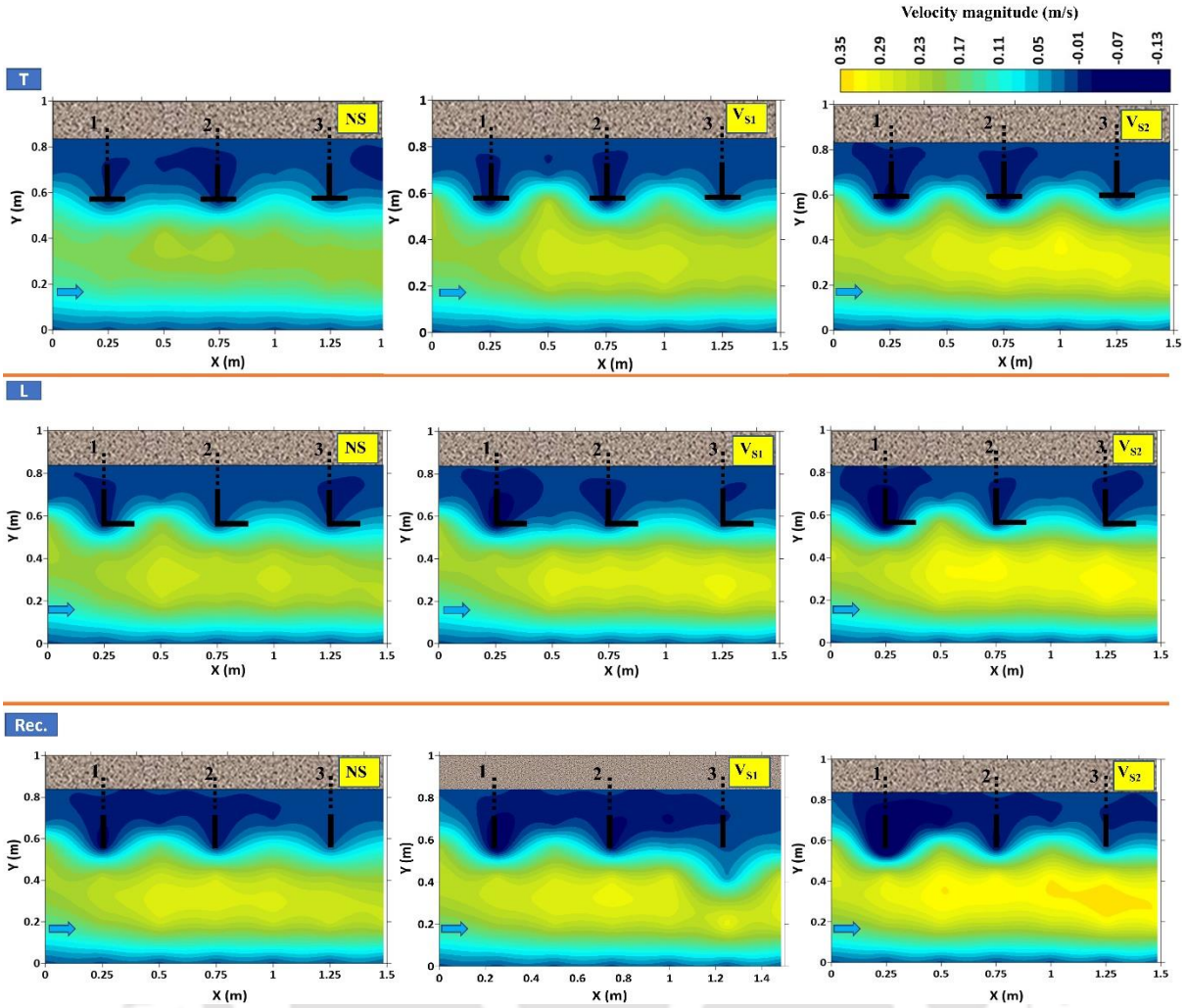

Figure 3.5 The plots of velocity magnitude in the streamwise direction, particularly near the channel bed z/h = 0.12.

3.5 Reynolds shear stress (RSS)

Reynolds shear stress (RSS) is a critical concept in fluid dynamics that helps us understand turbulent flows. It shows how momentum moves between the horizontal streamwise and vertical directions due to changing velocities in vertical (Z) and streamwise (X) directions. This parameter is essential for studying how fluids behave, especially in turbulent situations. The experiment's findings showed variations in Reynolds shear stress were observed within the test section due to the spur dikes' wake formation. Furthermore, the spur dike disrupted the incoming flow, enhancing horizontal turbulent mixing.

Figure 3.6 displays the distribution of Reynolds shear stress near the channel boundary, particularly at z/h = 0.12. Notably, a distinctive behaviour arises near the channel bed at this depth, where the influence of seepage becomes more prominent. A reversal in RSS magnitude is observed around the first spur dike near the channel bed, characterised by negative values. This negative effect becomes even more pronounced with the introduction of seepage. Thus, it plays a critical role in the sediment detachment from the base of the spur dikes, and the presence of downward seepage further accelerates this detachment process. This negative trend in streamwise RSS magnitude also holds true for other spur dike shapes.

For instance, in the case of the T-shaped spur dike, the increase in RSS magnitude with seepage velocities V_{S1} and V_{S2} is 1.88 times and 2.9 times, respectively, compared to scenarios without seepage. L-shaped spur dike exhibits an increase of 54% (V_{S1}) and 1.3 times (V_{S2}) in RSS magnitude with seepage compared to no seepage. Similarly, the Rectangular-shaped spur dike shows an RSS magnitude increase of 23% (V_{S1}) and 74 % (V_{S2}) with seepage, compared to no seepage.

Without seepage, the RSS magnitude increases 1.2 times for L-shaped and 2.4 times for Rectangular-shaped spur dikes compared to the T-shaped spur dike. However, with seepage velocity (V_{S1}), the velocity magnitude increase for L-shaped and Rectangular-shaped spur dikes was 18% and 45%, respectively, compared to the T-shaped spur dike. Similarly, for seepage velocity (V_{S2}), the RSS magnitude increase for L-shaped and Rectangular-shaped spur dikes was 30% and 51%, respectively, compared to the T-shaped spur dike. This consistent pattern underscores that as the seepage rate rises, the RSS magnitude consistently experiences an increase.

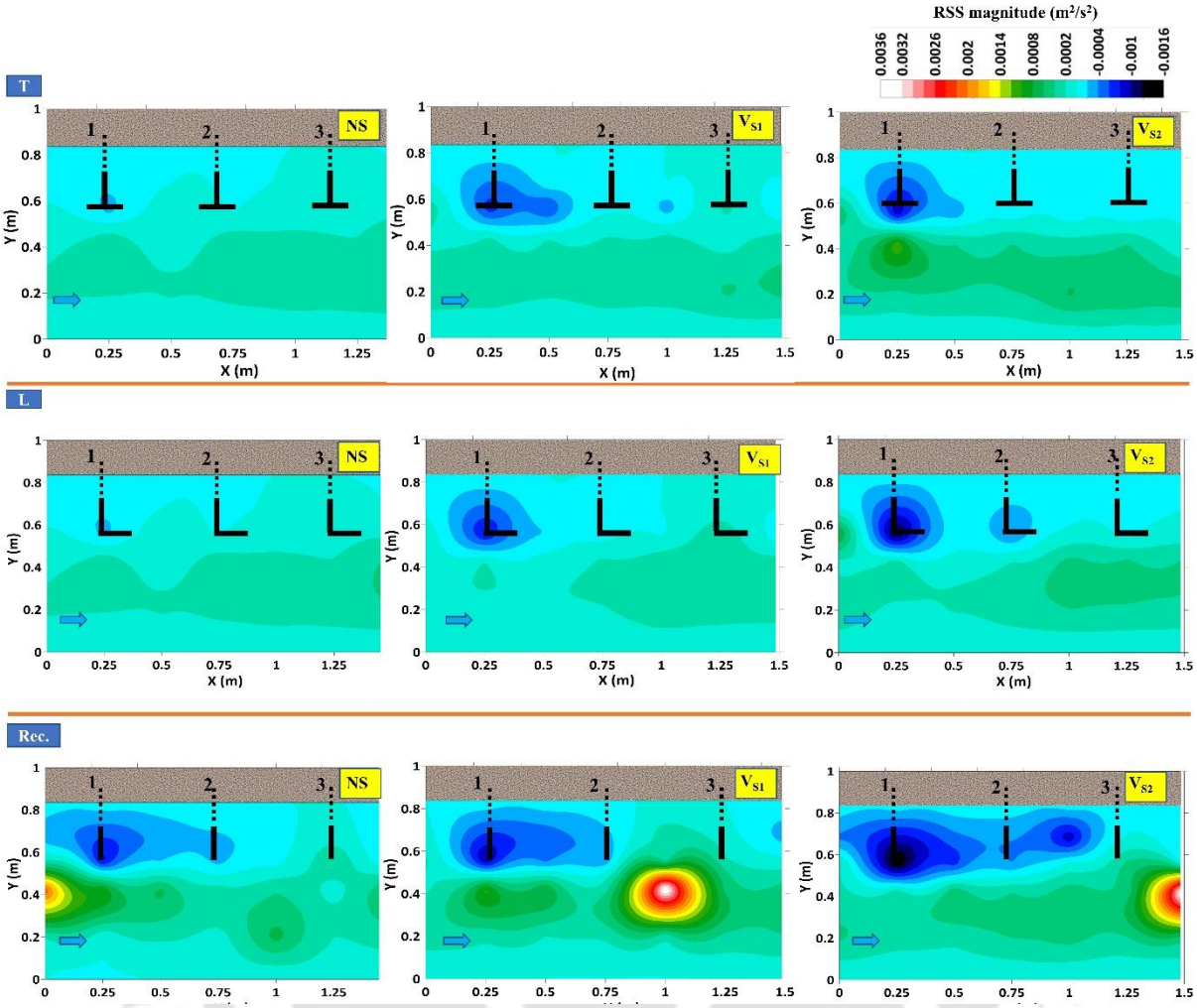

Figure 3.6 The plots of RSS magnitude, particularly near the channel bed *z/h* = 0.12.

3.6 Bed Shear Stress (BSS)

The force that moving water in a river or channel applies to the riverbed is called bed shear stress. This force is caused by the dynamic interaction between the water and the bed, where the flowing water exerts pressure on the bed, and the bed resists that pressure due to its roughness or irregularities. BSS's magnitude is affected by velocity, channel slope, and bed surface properties.

The stability of a river channel, the erosion rate of its bed, and sediment movement are all influenced by bed shear stress. Spur dikes are man-made barriers that disrupt water flow and increase turbulence. Because of the turbulence, estimating the bed shear stress using conventional methods near these structures is challenging. Researchers established

various approaches to estimate bed shear stress close to structure. One typical approach includes using specialist sensors, such as acoustic Doppler velocimeters (ADV), capable of measuring the flow's instantaneous velocity and turbulence near structures. The turbulent kinetic energy (TKE) technique may determine the BSS by measuring flow velocity using the ADV. An empirical equation that relates the TKE to the bed shear stress may be used to calculate the bed shear stress. The equation is given as follows:

$$\tau_0 = C \times \rho \times TKE \tag{3.1}$$

The symbol "ρ" denotes the density of water. Previous studies adopted a constant value of "*C*" to represent the resistance coefficient for flow in open channels. Specifically, this value has been reported as 0.19 in studies (Stapleton & Huntley,1995; Thompson et al., 2003).

Turbulent kinetic energy measures the energy associated with turbulence in a fluid flow. It represents the sum of the kinetic energies of the turbulent fluctuations in velocity within the fluid. Turbulent Kinetic Energy (TKE) is closely related to the fluid flow's velocity fluctuations and is a significant parameter in investigating alluvial channels. The equation represents it as follows:

$$TKE = \frac{1}{2}(\overline{u'u'} + \overline{v'v'} + \overline{w'w'}) \tag{3.2}$$

The variables u', v', and w' denote the turbulent velocity fluctuations in the streamwise, transverse, and vertical directions of the flow.

Bed shear stress was calculated for no seepage and seepage velocities (V_{S1} and V_{S2}) for different shapes of spur dikes. The value of bed shear stress was computed at the center of the spur dike field (Table 3.1).

Table 3.1 Description of bed shear stress values with the condition of seepage and different spur dike shapes.

Seepage condition	NS	V_{S1}	V_{S2}	NS	V_{S1}	V_{S2}	NS	V_{S1}	V_{S2}
	T-shape			L-shape			Rectangular shape		

Bed shear stress (T_0) near bed $z/h < 0.2$ (N/m^2)									
	0.66	0.69	0.78	0.69	0.73	0.82	0.89	0.95	1.16

The computed bed shear stress values exceeded the critical bed shear stress of 0.64 N/m² in all scenarios, considering seepage conditions and different spur dike shapes. This shows that the water flow in the channel was adequate to promote sediment transport. The influence of bed shear stress on sediment movement is more pronounced under downward seepage conditions. Additionally, the shape of the spur dike significantly affects bed shear stress. Rectangular-shaped spur dikes produce the higher bed shear stress compared to L- and T-shaped dikes due to their blunt geometry, which directly obstructs the flow, creating intense flow constriction, and stronger turbulence around the structure. This leads to the formation of larger horseshoe vortices and increased bed shear stress. Whereas, T-shaped dikes extend laterally, guiding the flow more streamlined compare to rectangular-shape and L-shape. This reduces velocity concentration near the base, leading to lower bed shear stress. Furthermore, the sediment transport rate increases with both the seepage application rate and the effect of shape of the spur dikes.

3.7 Multiscale statistical characterisation of scour depth evolution rate

The bed elevation fluctuations at locations (P), (Q), and (R) around the spur dike field were measured using Ultrasonic Ranging System (URS) at different time steps, including the initial time (0 h) and after 2, 6, and 12 h, and presented in Figure 3.7. At locations (P) and (Q), it was noticed that the scour depth (compared to the bed level) initially increased rapidly and then gradually changed over time, regardless of seepage conditions. This pattern persisted until a balance was achieved between the stream's capacity to erode and the resistance of the bed material to movement. The scour depth increases as the seepage velocity increases. Moreover, the rate of scouring was faster in the presence of seepage compared to the absence of seepage.

This is likely because the downward seepage destabilises particles resting on the boundary, initiating their motion.

As the flow moves downstream, it loses its strength due to the structure's hindrance and the channel bed's resistance, causing sediment to settle down. Deposition of detached sediment was observed in the confined area between spur dikes and around spur dike-3, and the deposition rate rose with higher seepage rates. The increased deposition volume over the same 24-hour period supported this observation.

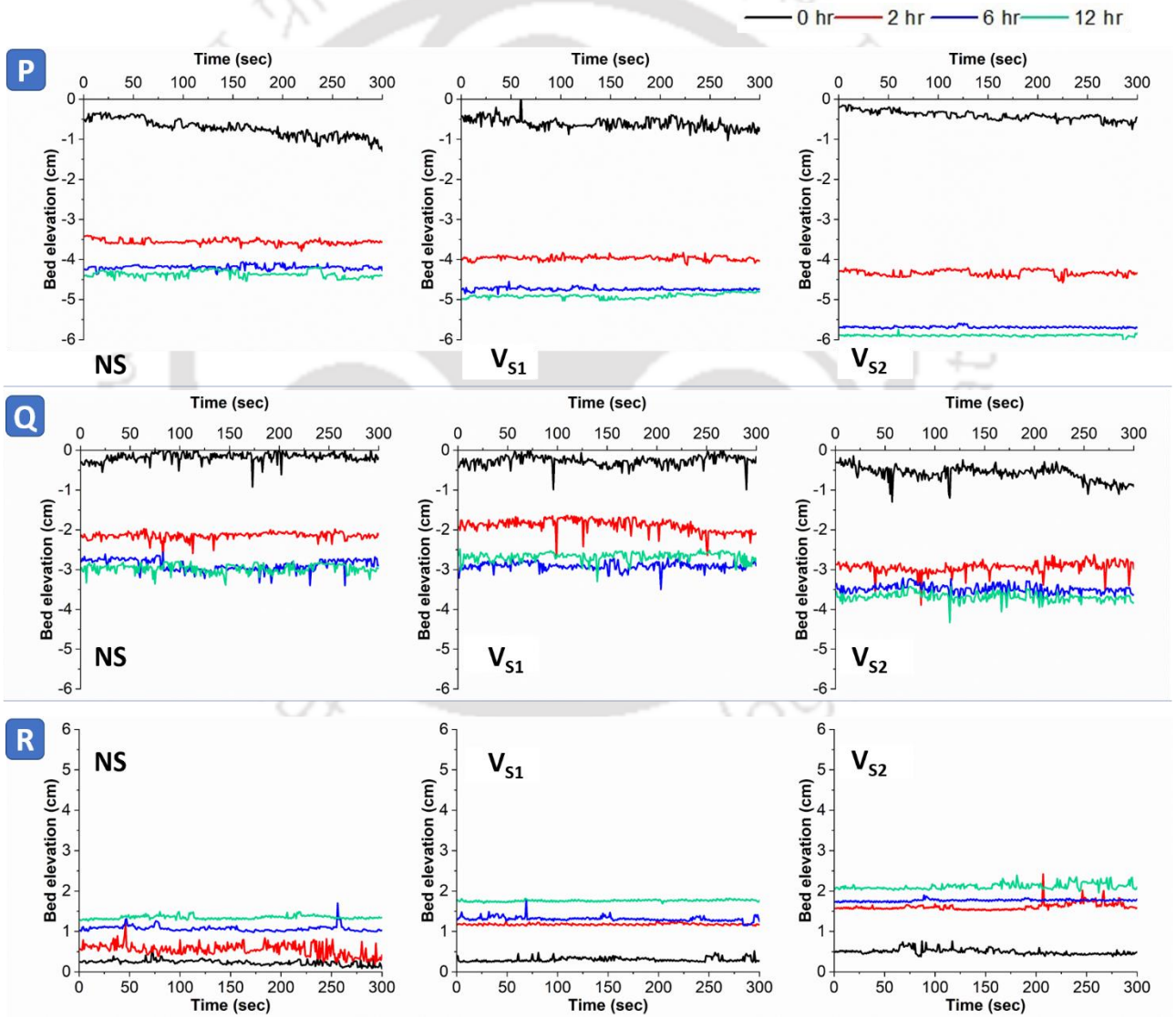

Figure 3.7 Bed elevation fluctuations at locations (P), (Q), and (R) for no seepage and seepage velocities V_{S1} and V_{S2} with a flow rate of 0.03 m^3/s

During the study of migrating scouring, it was observed that the erosion of the channel's bed varied depending on the length and duration of the area under investigation. This variability indicated the presence of a phenomenon known as "scale-dependent celerity." The rate at which alluvial scouring occurs can differ significantly based on spatial and temporal scales. To better understand this phenomenon, the researchers employed wavelet transformation on the bed elevation data. By analysing the lag corresponding to the highest cross-correlation coefficient between two series of bed elevation data, the study determined the celerity that varies with scale. Bed elevation data was collected using transducers at one-second intervals throughout the experiment, allowing us to assess the temporal scale celerity of the scour hole around the spur dikes.

3.8 Wavelet transforms

3.8.1 Time-frequency analysis

The wavelet transform has evolved into a robust time-frequency analysis and signals coding tool in recent years, and it is now preferred for the analysis of complex nonstationary signals. The Wavelet transforms and decomposes a signal at different timescales. Wavelet transform aids in providing a clearer and more significant insight for examining quantities that exhibit a broad range of physical and dynamic characteristics across various scales. It is described as a collection of fundamental operations $\psi_{a,b}(t)$ that can be produced by rescaling and translating the so-called mother wavelet as follows

$$\psi_{a,b}(t) = \frac{1}{\sqrt{a}}\psi\left(\frac{t-b}{a}\right); a > 0, -\infty < b < \infty, \tag{3.3}$$

Where a and b are the two parameters, a defined as scale parameters, and b determines the wavelet location.

Continuous Wavelet transforms (CWT) are used to project moving signals' fluctuating properties. However, CWT represents the time frequency of a signal *f(t)* that the following equation can define:

$$W_f(a,b) = \int_{-\infty}^{+\infty} \psi_{a,b}(t) f(t) dt \tag{3.4}$$

Here, the integral transform using a set of functions $\Psi_{a,b}(t)$ defines the CWT of a signal *f (t).* The wavelets obtained from a mother wavelet are denoted by $\psi_{a,b}(t)$.

$$\psi_{a,b}(t) = \frac{1}{\sqrt{a}} \psi \left(\frac{t-b}{a}\right), \tag{1.5}$$

The mother wavelet must follow the invertible wavelet transform's admissibility requirement, which is provided by:

$$\int_{-\infty}^{+\infty} \psi_{a,b}(t) dt = 0 \tag{3.6}$$

This suggests that the area under the curve must be zero to act as a local differencing filter. Higher-order vanishing moments in a wavelet, i.e.

$$\int_{-\infty}^{+\infty} t^k \psi(t) dt = 0, \qquad (k = 1,2,3, \ldots . N-1 \ldots, \infty) \tag{3.7}$$

The availability of wavelets with higher-order disappearing moments facilitates the development of higher-order differencing filters that can eliminate polynomial sets from a signal.

An order polynomial '*N-1*' was eliminated using a wavelet with '*N*' vanishing moments. A family of wavelets having Nth-order derivatives of the Gaussian function $g_0(t)$ is known as the mother wavelet (*t*). Given as

$$g_N(t) = \left(\frac{d^N}{dt^N}\right) g_0(t), N = 1, 2\ldots\ldots). \quad (3.8)$$

Since the Mexican hat wavelet $g_2(t)$ was used as the mother wavelet in the current study, wavelet coefficients were computed using the well-known Mexican hat wavelet *N*=2:

$$g_2(t) = \frac{2}{\sqrt{3}}\pi^{\frac{-1}{4}}(1-t^2)e^{\frac{-t^2}{2}} \quad (3.9)$$

The wavelet coefficients were determined by substituting eq. (3.9) into equations (3.5) and (3.6),

$$W_f(a,b) = \frac{1}{\sqrt{a}}\int_{-\infty}^{+\infty} g_2\left(\frac{t-b}{a}\right) f(t)dt \quad (3.10)$$

Between two data sets, $f_1(t)$ and $f_2(t)$, the wavelet cross-covariance (*WCC*) was calculated as,

$$WCC_{f_1 f_2}(a,\Delta t) = \int_{-\infty}^{+\infty} W_{f_1}(a,b)W_{f_2}(a,b+\Delta t)db \quad (3.11)$$

where the WCs of the two-bed elevation series *f1(t)* and *f2(t)*, respectively, at scale a and two adjacent locations b and $b+\Delta t$, are $W_{f_1}(a,b)$ and $W_{f_2}(a,b+\Delta t)$, respectively. To compute the wavelet cross-correlation, the signal variance was standardised. Initially, this research established the wavelet coefficient for the bed elevation data series' variance. Afterwards, the lag was identified for a particular scale corresponding to the maximum cross-correlation coefficient between two wavelet series (*a*).

The temporal celerity of the scour depth is defined as the interval between two succeeding data series divided by the lag. The equation to find it is given as follows:

$$V_c(a,\Delta t) = L/\Delta t_{max} \quad (3.12)$$

Where 'L' denotes the separation between adjacent segments of the bed elevation series, and t_{max} represents the time when the cross-correlation between two signals is at its highest.

3.8.2 Maximum correlation coefficient

Figure 3.8 is a graphical representation of the maximum correlation coefficient between the upstream and downstream of the spur (1) at locations P and Q and between the upstream and downstream of the spur field at locations P and R. The figure plots the maximum correlation coefficient as a function of the time scale for seepage and no-seepage conditions. The results indicated that small-scale values (3 s) showed low cross-correlation coefficients, suggesting a lack of correlation and inconsistent celerity measures. Consequently, it is not advisable to associate any minor transient features that might vanish with the data recorded by the transducers. In contrast, larger-scale values (>6 s) exhibited an increasing correlation coefficient ranging from 0.5 to 0.8, indicating a higher level of correlation and consistent celerity measures. These findings suggest that analysing data at larger time scales may provide more reliable and accurate results. Furthermore, the correlation coefficient was higher at the initial time step of 0 h than at 6 and 12 h.

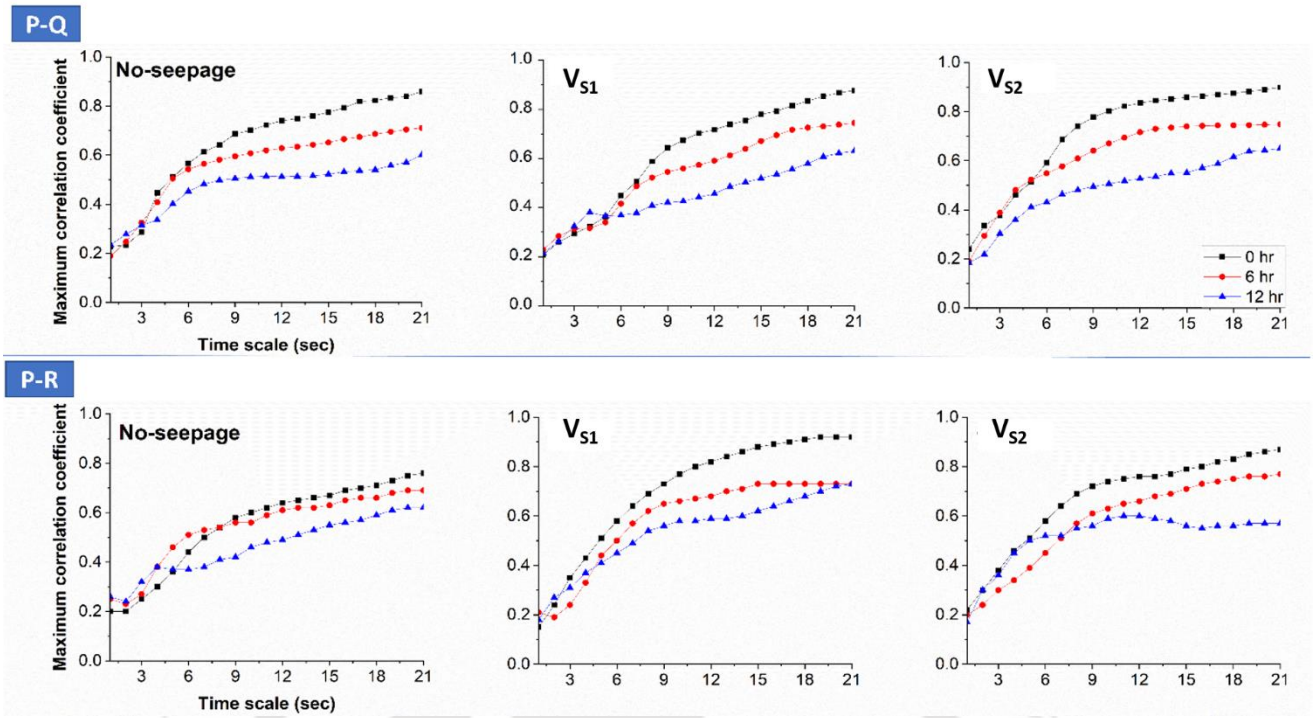

Figure 3.8 Showing the Maximum correlation coefficient at time steps 0, 6 and 12 hours at location P-Q and P-R for NS, V_{S1}, and V_{S2} with flow rate 0.03 m^3/s.

3.8.3 Time scale celerity

Time scale-dependent celerity was estimated by determining the time at which the maximum cross-correlation occurs. The time scale celerity for the spur dike field was evaluated using wavelet cross-correlation over a time scale of 1-21 s. The estimated celerity between location (P) to location (Q) and location (P) to location (R) with a temporal scale for no seepage and seepage flow is shown in Figure 3.9. The figure illustrates a clear pattern: as the scale increases, celerity gradually decreases. This observation suggests that larger-diameter scour holes tend to travel at a slower pace compared to smaller ones. In other words, as the size of the scour hole increases, its downstream movement becomes slower and more gradual. According to the figure, a smaller scale has higher celerity than a larger scale. The celerity of the scour hole has increased at a higher rate initially (0 h), compared to 6 and 12 h. Also, this moving rate is faster with a seepage velocity. Such as, the average time scale celerity, as shown in the Table-3.2, increases by about 5% with seepage velocity V_{S1} and 17% with seepage velocity V_{S2}, compared

to no-seepage conditions between locations P and Q. In locations P-R, the average celerity increases by about 5.5% with seepage velocity V_{S1} and 11% with seepage velocity V_{S2} compared to no-seepage conditions (Table 3.3).

Over time, the time scale celerity gradually decreases and eventually reaches equilibrium. This study observed that the average celerity of scour holes was lower in cases without seepage than those with seepage across different time scales. This finding suggests that under seepage conditions, the scour depth becomes deeper, as indicated by the faster movement of the scour holes over time.

In addition, the experiment findings with spur dikes in series compared with that of a single spur dike when placed in an experimental flume. At (P-Q) under no-seepage conditions, the averaged time scale celerity was 2.17 with series spur dikes and 2.09 with a single spur dike. For V_{S1}, it was 2.28 (series) and 2.16 (single), while for V_{S2}, it was 2.48 (series) and 2.36 (single) cm/hr. At (P-R), the celerity averaged 9.06 (series) and 7.81 (single) for no-seepage, 9.58 (series) and 8.67 (single) for V_{S1}, and 10.07 (series) and 9.15 (single) for V_{S2} cm/hr.

It was observed that the averaged time scale celerity is reduced with a single spur dike when compared with in series. The percentage reduction in celerity at (P-Q) was 3.72% (no-seepage), 5.28% (V_{S1}), and 4.81% (V_{S2}). At (P-R), it was more substantial: 13.47% (no-seepage), 9.37% (V_{S1}), and 9.13% (V_{S2}).

The experiments comparing the performance of spur dikes in series with that of a single spur dike in an experimental flume revealed some significant findings. At position (P-Q) under no-seepage conditions, we found that the averaged time scale celerity was slightly higher with series spur dikes compared to a single spur dike. Similarly, for V_{S1} and V_{S2}, the celerity values were also marginally higher with series spur dikes. At position (P-R), the pattern continued but

the magnitude of change was enhanced with series spur dikes consistently resulting in higher celerity values compared to a single spur dike.

Table 3.2 Statistics of the time scale bed celerity (cm/h) in sections P-Q

Time scale (sec)	No seepage			V_{S1}			V_{S2}		
	0 h	**6 h**	**12 h**	**0 h**	**6 h**	**12 h**	**0 h**	**6 h**	**12 h**
1	4.19	4.76	5.21	4.71	4.37	4.83	5.58	5.50	5.25
2	3.53	3.94	3.98	4.01	3.82	3.86	4.08	4.64	4.54
3	3.12	3.24	3.72	3.46	3.50	3.41	4.06	3.83	3.35
4	2.91	2.60	2.39	3.11	3.16	2.84	3.54	3.16	2.80
5	2.21	2.32	1.92	2.95	2.95	2.46	3.21	2.50	2.23
6	2.15	2.18	1.78	2.83	2.73	2.22	2.79	2.39	2.14
7	2.15	2.05	1.71	2.64	2.52	1.97	2.56	2.23	2.05
8	2.12	1.98	1.66	2.44	2.31	1.86	2.45	2.15	1.96
9	2.14	1.94	1.62	2.37	2.19	1.78	2.39	2.09	1.88
10	2.15	1.93	1.59	2.35	2.13	1.71	2.35	2.05	1.81
11	2.14	1.93	1.55	2.26	2.07	1.66	2.32	2.00	1.76
12	2.10	1.92	1.53	2.15	2.00	1.62	2.30	1.97	1.72
13	2.06	1.89	1.52	2.06	1.91	1.59	2.28	1.94	1.70
14	2.04	1.85	1.50	1.99	1.82	1.57	2.27	1.92	1.68
15	2.06	1.79	1.47	1.93	1.72	1.56	2.27	1.92	1.67
16	2.04	1.73	1.44	1.87	1.63	1.56	2.26	1.92	1.67
17	2.12	1.67	1.40	1.80	1.54	1.55	2.25	1.93	1.67
18	2.08	1.62	1.36	1.77	1.50	1.53	2.24	1.93	1.66
19	2.04	1.58	1.31	1.69	1.43	1.51	2.23	1.93	1.66
20	2.08	1.55	1.27	1.68	1.38	1.50	2.22	1.91	1.66
21	2.07	1.52	1.23	1.65	1.33	1.50	2.21	1.89	1.66
Average bed celerity	**2.36**	**2.19**	**1.96**	**2.46**	**2.29**	**2.10**	**2.76**	**2.47**	**2.22**

Table 3.3 Statistics of the time scale bed celerity (cm/h) in sections P-R

	No seepage			V_{S1}			V_{S2}		
Time scale (sec)	**0 h**	**6 h**	**12 h**	**0 h**	**6 h**	**12 h**	**0 h**	**6 h**	**12 h**
1	23.19	20.63	18.80	26.31	25.57	23.19	23.20	23.02	19.26
2	20.32	18.42	14.75	20.69	19.43	18.42	16.15	15.61	15.62
3	18.65	17.39	12.41	18.26	17.17	15.72	13.90	12.98	14.72
4	15.51	12.16	10.20	15.58	14.76	12.08	12.39	10.28	13.69
5	12.90	10.16	8.27	13.89	12.55	9.26	11.52	9.27	11.93
6	10.57	9.17	8.11	11.11	11.32	7.67	10.67	8.96	10.38
7	9.33	8.77	7.34	10.48	10.36	6.82	10.60	8.97	9.11
8	8.61	8.62	6.80	8.65	9.72	6.38	10.43	9.12	8.25
9	8.08	8.56	6.52	8.27	8.75	6.15	10.21	8.90	7.69
10	7.72	8.52	6.35	8.11	8.21	6.04	10.16	8.54	7.37
11	7.47	8.38	6.25	8.02	7.87	5.97	10.05	8.35	7.17
12	7.30	8.16	6.17	7.94	7.68	5.94	10.00	8.33	7.03
13	7.16	7.82	6.11	7.86	6.74	5.92	9.83	8.43	6.89
14	7.05	7.44	6.03	7.72	6.43	5.91	9.83	8.63	6.73
15	6.93	7.03	5.93	7.53	6.33	5.89	9.90	8.89	6.57
16	6.81	6.67	5.83	7.28	5.84	5.89	9.64	9.14	6.43
17	6.68	6.36	5.72	7.04	5.57	5.88	9.27	9.05	6.31
18	6.54	6.12	5.61	6.83	5.32	5.88	9.03	8.96	6.22
19	6.40	5.94	5.52	6.65	5.19	5.89	8.92	8.88	6.15
20	6.26	5.81	5.45	6.51	5.70	5.89	8.93	8.81	6.11
21	6.12	5.70	5.39	6.41	5.06	5.89	8.32	8.78	6.09
Average bed celerity	**9.98**	**9.42**	**7.79**	**10.53**	**9.79**	**8.41**	**11.09**	**10.09**	**9.03**

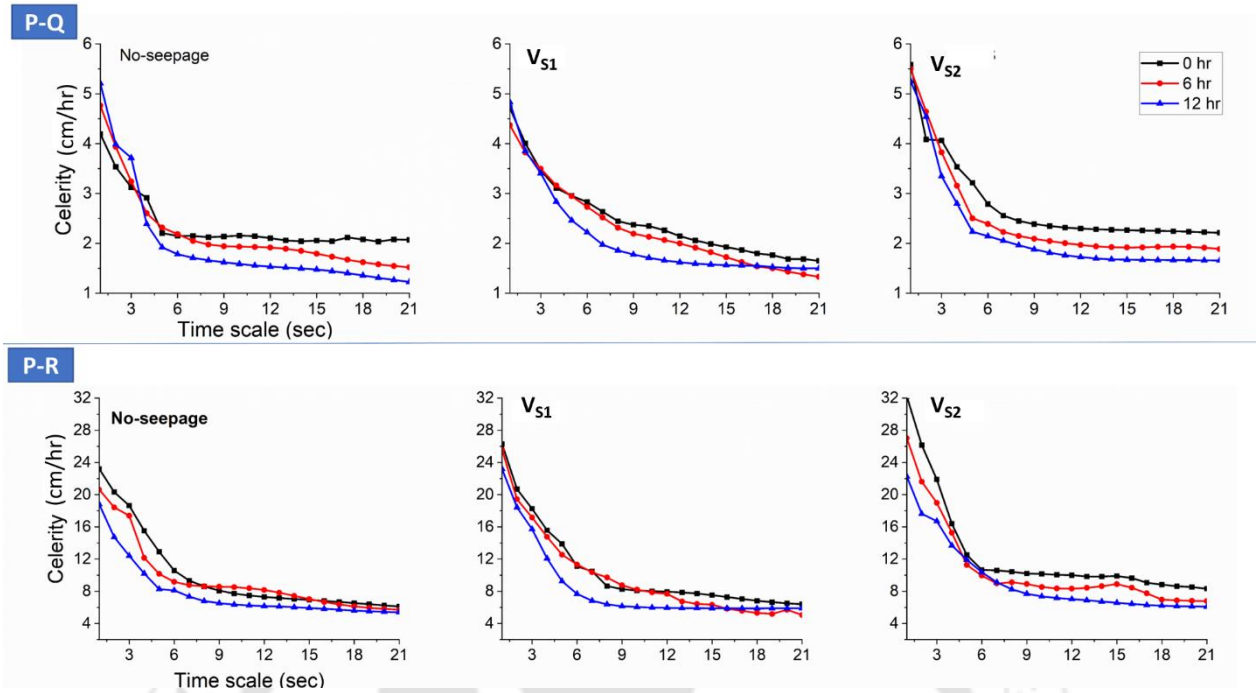

Figure 3.9 Showing the Time scale celerity at location P-Q and P-R at time steps 0, 6 and 12 hours for NS, V_{S1}, and V_{S2} with flow rate 0.03 m^3/s

3.8.4 Length scales celerity

Tables 3.4 and 3.5 summarise the celerity statistics of length scales between locations P-Q and P-R, respectively. The data were collected at two-time intervals (0-6 h and 6-12 h) under seepage and non-seepage conditions. This section examines the impact of seepage on the length scale celerity of the spur field. To accomplish this, we discretised the bed elevation data into different length scales and calculated the wavelet coefficients for the data series. We then determined the lag corresponding to each scale's highest cross-correlation coefficient. Finally, we calculated the celerity by dividing the lag by the time difference between two subsequent series. The length scale celerity of Scale 1-21mm was calculated using wavelet cross-correlation. Figure 3.10 illustrates the celerity using different length scales for different time intervals. The celerity of bedforms increases from 0 to 6 h and decreases after 6 h (6-12 h). Additionally, the figure shows that celerity decreases rapidly up to a particular length scale (0-6 mm) and then stabilises at larger length scales (6-21 mm) of bedforms.

Results also revealed that, when seepage is applied, the length scale celerity increases faster than no seepage condition, and maximum celerity experiences with seepage velocity V_{S2}. The average length scale celerity increases by about 50% with seepage velocity V_{S1} and by 132% with seepage velocity V_{S2} for the location between P-Q. The average celerity in locations P–R rises by 38.4% with seepage velocity V_{S1} and nearly three times with seepage velocity V_{S2}. Over time, the average celerity falls and finds equilibrium. Compared to location P-Q, location P-R experiences a much higher transportation rate. This rate is due to the high sediment transport rate in the spur dike field, as flow is diverted through the first spur dike, resulting in higher momentum transfer. As a result, the rate of celerity increases.

Table 3.4 Statistics of the Length scale celerity (mm/h) between sections P-Q

	No-seepage		***V*S1**		***V*S2**	
Length scale (mm)	**0-6 h**	**6-12 h**	**0-6 h**	**6-12 h**	**0-6 h**	**6-12 h**
1	38.37	13.68	72.80	21.55	119.14	42.39
2	22.95	8.01	32.22	12.45	55.59	20.99
3	16.51	6.11	22.89	7.72	45.95	12.82
4	12.76	4.90	21.04	6.53	31.52	9.84
5	10.76	4.18	18.53	6.26	26.35	8.55
6	9.73	3.41	18.10	6.03	24.21	7.87
7	9.25	2.99	16.99	5.56	20.76	7.42
8	9.03	2.74	15.89	5.10	19.16	7.11
9	8.91	2.58	13.76	4.78	18.30	6.88
10	8.85	2.47	13.08	4.58	17.81	6.72
11	8.81	2.40	12.76	4.45	17.49	6.61
12	8.79	2.33	12.07	4.36	17.27	6.53
13	8.76	2.27	11.60	4.30	17.11	6.47
14	8.72	2.23	11.28	4.25	16.98	6.42
15	8.67	2.19	11.05	4.21	16.86	6.36
16	8.60	2.16	10.89	4.18	16.72	6.30
17	8.53	2.14	10.76	4.16	16.50	6.26
18	8.46	2.12	10.67	4.14	16.26	6.22
19	8.40	2.10	10.59	4.12	16.08	6.19

20	8.35	2.09	10.54	4.10	15.92	6.17
21	8.30	2.08	10.49	4.09	15.79	6.15
Average bed celerity	**11.50**	**3.58**	**17.52**	**6.04**	**26.75**	**9.54**

Table 3.5 Statistics of the Length scale celerity (mm/h) between sections P-R

Length scale (mm)	No- seepage		V_{S1}		V_{S2}	
	0-6 h	6-12 h	0-6 h	6-12 h	0-6 h	6-12 h
1	225.21	84.78	329.41	165.62	600.25	325.30
2	147.62	40.02	184.20	85.16	378.66	123.68
3	75.58	20.44	114.06	45.02	207.29	73.35
4	41.75	10.64	78.56	32.28	140.75	44.45
5	29.80	6.23	46.22	27.04	88.83	38.98
6	22.84	4.00	32.03	23.93	64.68	32.58
7	19.23	2.74	23.88	18.54	53.70	26.01
8	16.11	1.98	18.99	12.97	48.36	19.10
9	13.88	1.49	15.84	9.25	45.53	16.48
10	12.22	1.17	13.77	7.93	43.58	12.04
11	10.85	0.94	12.24	6.40	41.95	11.99
12	9.72	0.78	11.00	5.93	40.29	11.46
13	8.99	0.65	10.88	5.76	38.73	11.25
14	8.70	0.55	10.80	5.56	37.25	10.99
15	8.58	0.47	10.77	5.33	35.91	10.95
16	8.43	0.40	9.81	5.28	34.73	10.83
17	8.36	0.35	9.73	5.23	33.66	10.73
18	8.29	0.31	9.63	5.13	33.69	10.64
19	8.13	0.27	9.25	5.08	33.38	10.57
20	8.04	0.24	9.15	4.98	32.06	10.50
21	8.04	0.21	9.11	4.14	31.39	10.45
Average bed celerity	**33.35**	**8.51**	**46.16**	**23.17**	**98.32**	**39.63**

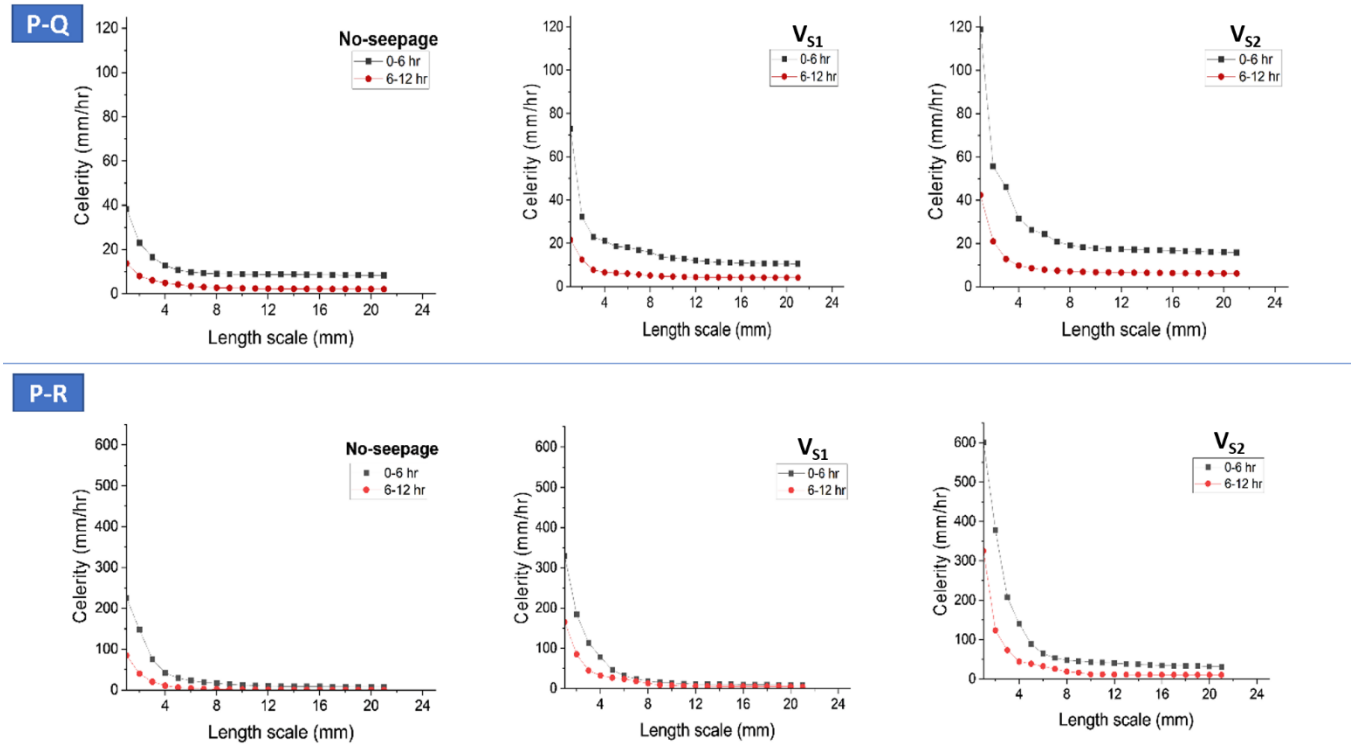

Figure 3.10 Showing the Length scale celerity at locations P-Q and P-R at different time steps for NS, V_{S1}, and V_{S2} with a flow rate of 0.03 m^3/s

3.9 Conclusion

In summary, our study demonstrates that downward seepage significantly enhances sediment transport, resulting in deeper scour depths at the riverine structure's base and substantial changes the entire channel morphology. This effect intensifies with increasing seepage rates. The scour depth undergoes rapid changes in the initial 6 to 8 h, followed by a more gradual evolution until stabilisation around 18 h across all examined spur dike shapes. Notably, T-shaped spur dikes exhibit a slower scour development rate.

Examining the experimental data, we observed the maximum velocity magnitude around Rectangular-shaped dikes at the water surface (z/h = 0.50), while T-shaped dikes displayed weaker velocities. This pattern strengthens with increasing seepage rates. At the near channel bed (z/h = 0.12), a notable impact on velocity magnitude was observed at the maximum scour depth position, indicating flow reversal patterns linked to horseshoe vortices' formation and

currents' generation. Downward seepage accelerates the detachment of particles from the structure base. Additionally, spur dikes disrupt the flow, altering Reynolds shear stress and increasing horizontal turbulence mixing, further amplified by seepage, causing flow reversals and particle detachment.

Different geometric configurations of T-shaped, L-shaped, and rectangular-shaped spur dikes impact their effectiveness in reducing local scouring. The head arrangement of L-shaped dikes may influence flow patterns and energy distribution. Rectangular-shaped dikes generate more direct flow obstructions, contributing to localised scouring by creating significant eddies and turbulence behind the dike's head. However, in T-shaped dikes, downward seepage interacts with the streamlined flow created by the dike, actively contributing to maintaining the equilibrium of sediment particles. This equilibrium restricts the displacement of particles, mitigating the scouring potential near the dike.

The scour depth's celerity was computed using wavelet cross-correlation over a 1–21 s time scale. When compared to a larger scale, the smaller scale has higher celerity. The rate of the scour hole has accelerated in the time interval of 0 h compared to 6 and 12 h. The average celerity initially rises by about 5 % with seepage velocity V_{S1} and by 17 % with seepage velocity V_{S2} for locations P-Q, and about 5.5 % with seepage velocity V_{S1} and 11 % with seepage velocity V_{S2} for locations P-R, compared to no-seepage conditions. The average celerity decreases over time and eventually reaches equilibrium. Over various time and length scales, this study found that the average celerity was lower for no seepage than for seepage runs.

For large-scale values (>6 s), the correlation coefficient progressively increases (range of 0.5–0.8). For small-scale values (3 s), small values of cross-correlation coefficients are obtained, indicating a lack of correlation and making it difficult to obtain reliable measurements of

celerity using cross-correlation analysis. The correlation coefficient at 0 h is higher than at 6 and 12 h.

The spatial celerity of bedforms increases from 0 to 6 h and decreases from 6 to 12 h. Specifically, the speed of bedforms decreases rapidly up to a certain length scale, ranging from 0 to 6 mm, and then stabilises at larger scales between 6 and 21 mm. When seepage is applied, the length scale celerity rises more quickly than under no-seepage conditions, and maximum spatial celerity was observed with seepage velocity V_{S2}.

This study is valuable for river management as it offers comprehensive insights into how seepage interacts with spur dikes, affecting sediment transport, scour depth, and flow dynamics. These findings are crucial for designing resilient river structures and irrigation systems capable of effectively managing seepage-related challenges, including seepage-resistant lined canals, permeable reactive barriers, seepage-controlled irrigation ponds, etc. This ensures the long-term sustainability and efficiency of water systems for agricultural and environmental purposes.

Experimental studies cannot fully replicate natural rivers with irregular banks, moving bedforms, vegetation, seasonal changes and seepage rates. However, they are essential for isolating specific phenomena and for comparative analysis.

While lab experiments offer valuable insights, it is crucial to acknowledge their limitations, particularly regarding their applicability to real-world situations. To address this, future studies will consider nonuniform sediment sizes, as this will lead to a better understanding of the complex interactions involved in downward seepage and scouring behaviour.

4 Channel Morphology with Permeable Spur Dikes under Downward Seepage[8]

4.1 Introduction

In the field of hydraulic river engineering, safeguarding riverbanks is of utmost importance for preserving natural river systems, adjacent lands, and essential infrastructure, such as bridges (Arora et al., 2023; Hasan & Toda, 2024). Various protective structures, including spur dikes, which play a critical role in counteracting the erosive forces of flowing water, are used. These dikes extend outward from the riverbank in different directions and configurations to divert the current away from the bank.

There are two types of spur dikes based on their permeability: permeable and impermeable spur dikes. While impermeable dikes obstruct and redirect incoming flows, permeable dikes facilitate flow passage at diminished velocities, thereby minimizing erosive impacts (Mioduszewski et al., 2003; Akbar et al., 2024). In contrast to impermeable counterparts, permeable spur dikes offer numerous advantages, including structural simplicity, reliable operation, ease of maintenance, enhanced stability, and reduced investment requirements (Shampa et al., 2020; Iqbal et al., 2021; Mirzaei et al., 2021; Tripathi & Pandey, 2021, 2022).

Several studies have been conducted to investigate the flow dynamics and scouring characteristics associated with permeable spur dikes (Osman & Saeed, 2012; Zhou et al., 2014; Esmaeli et al., 2022; Haider et al.,2022a; Hu et al., 2022). They found that permeable spur dikes can mitigate excessive scouring in the main river channel, reduce the local scour depth near dikes, and enhance overall safety compared to impermeable spurs.

[8] Patel, H.K., & Kumar, B. (2024). Channel Morphology with Permeable Spur Dike under Downward Seepage. (Under review)

Additionally, Osman and Saeed (2012) experimentally explored the impact of contraction on both spur dikes, revealing that impermeable dikes with higher contraction ratios exhibit significantly greater scour depths. Gao et al. (2022) observed that the flow velocity gradient and the vortex shedding frequency in the mixing layer increase as the blockage ratio increases. Yang et al. (2022b) showed that permeable spur dikes can effectively reduce velocities and enhance energy dissipation rates, particularly in spillway bends. Furthermore, research has explored the relationship between permeability and scour dimensions, revealing a direct correlation wherein decreased permeability corresponds to increased scour dimensions (Elawady et al., 2001; Li & Altinakar, 2016; Shahabi & Kashefipour, 2016; Nath & Misra, 2017).

Permeable spur dikes alter flow patterns and regulate sediment transport (Baba et al., 2010; Gu et al., 2011; Dingorkar et al., 2017). They have been shown to effectively reduce erosion and control sediment transport, particularly in compound channel scenarios. Moreover, studies have underscored the superiority of permeable dikes over impermeable dikes for reducing scour depths and altering flow pattern (Nasrollahi et al., 2008; Zhang & Nakagawa, 2008). In the study, Iqbal et al. (2021) investigated both types of spur dikes with varying permeability. Their findings revealed that increasing the permeability to 74% led to a reciprocal decrease in the mean streamwise velocity. Moreover, spur dikes exhibited reduced recirculation regions with increased permeability, permeable spur dike heads exhibited significant reductions in turbulent intensity (T.I.) and turbulent kinetic energy (TKE). Akbar et al. (2024) recommended permeable spur dikes to mitigate turbulent flow during floods, reduce scour depth, minimize recirculation regions, and effectively safeguard spur dike heads.

Despite numerous efforts to understand and control the scour depth in alluvial channels, predictions are still lacking, especially considering the effects of downward seepage through permeable boundaries. Previous studies (as mentioned in section 1.5) have highlighted the

significant influence of downward seepage on channel geometry, with higher seepage rates leading to increased conveyance of bedload and impacting the shape of the channel and surrounding ecological balance.

After thoroughly reviewing the available literature, several studies have been conducted to investigate the scour patterns around impermeable and permeable spur dikes. Previous research has shown that varying permeability can help to reduce scour formation by increasing the flow velocity through spur dikes. However, the literature does not comprehensively evaluate how permeable spur dikes affect scouring processes, especially regarding critical factors such as seepage. The present study aimed to fill this gap by examining how permeability affects scour progression around T-shaped spur dikes when subjected to downward seepage. Through this investigation, we aim to contribute to a deeper understanding of how permeable spur dikes can mitigate turbulent flow during floods, reduce scour depth, minimize recirculation regions, and effectively safeguard spur dike heads.

4.2 Experimental Conditions

Three experimental sets Set-A, Set-B, and Set-C were designed to investigate the impact of permeability on scour formation, bed morphology, and flow patterns. Set-A consisted of three impermeable spur dikes arranged in series, while Set-B included a 60% permeable first spur dike with the other two remaining impermeable. In Set-C, Spur-1 was 60% permeable, Spur-2 was 30% permeable, and Spur-3 remained impermeable. Each experimental set was analyzed under a discharge of 0.030 m^3/s and three seepage conditions: no seepage, seepage velocity V_{S1} = 0.09 mm/s and seepage velocity V_{S2} = 0.18 mm/s. The average flow depth observed for this discharge was 0.135 m. The experiments were conducted using sediment with a median particle size (d_{50}) of 0.23 mm. Additional experimental details are provided in Table 2.4.

4.3 Scour Depth Evolution

4.3.1 Based on seepage

Figures 4.1 to 4.3 display the changes in the channel bed shape inside the test section. The measurements were taken for three permeability sets (Set-A, Set-B, and Set-C) under three distinct conditions: no seepage, V_{S1}, and V_{S2}.

The maximum scour depth was measured in Set-A, where all three spurs were impermeable, as shown in Figure 4.1. The maximum scour depth was recorded at the edge of the first spur dike wing, with values of 10.23 cm, 11.56 cm, and 12.89 cm for the conditions without seepage, V_{S1}, and V_{S2}, respectively. This variation demonstrates a proportional increase in the maximum scour depth with increasing seepage. Specifically, the application of V_{S1} led to a 13% increase in the maximum scour depth, while the application of V_{S2} resulted in a 26% increase compared to that in the no-seepage scenario.

For Set B (Figure 4.2), the first spur dike was permeable at 60%, while the other two remained impermeable. Due to this permeability set the scour depth decreased around the first spur dike as 6.3 cm, 7.1 cm, and 8.33 cm for no-seepage, V_{S1}, and V_{S2}, respectively. However, the maximum scour depth shifted downstream and was observed around the second spur dike (9.56 cm, 9.99 cm, and 10.47 cm for no-seepage, $V_{S1,}$ and V_{S2}, respectively). The maximum scour depth increased by 12.6% for V_{S1} and 32.2% for V_{S2} relative to the no-seepage condition around the first spur dike. However, around the spur dike-2, the maximum scour depth increased by 5% for V_{S1} and 9.5% for V_{S2} compared to that under conditions without seepage.

To further reduce the maximum scour depth, we utilized set-C. In the case of the permeability Set-C of the spur dike (Figure 4.3), Spur-1 was permeable at 60%, Spur-2 was permeable at 30%, and Spur-3 remained impermeable. Now, the maximum scour depth decreased at both the first and second spur dikes. Around the first spur dike, the maximum scour depth decreased and was 4.58 cm, 6.65 cm, and 6.78 cm for the conditions without seepage, V_{S1}, and V_{S2},

respectively. The maximum scour depth around the second spur dike decreased to 6.70 cm, 6.82 cm, and 7.36 cm for the conditions without seepage, V_{S1}, and V_{S2}, respectively. However, seepage still had a substantial impact, increasing the maximum scour depth by 45.1% for V_{S1} and 48% for V_{S2} compared to the no-seepage scenario for the first spur dike and 2% for V_{S1} and 9.8% for V_{S2} compared to the no-seepage scenario for the second spur dike.

Regarding seepage conditions, the findings show that seepage has a significant impact on the maximum scour depth. Increased seepage rates correspond to more extensive scouring and cause greater channel morphology and bed configuration distortion. Seepage intensifies the movement of bed particles, leading to increased detachment and the formation of deeper scour depressions in the riverbed. These results align with those of previous studies (Prinos, 1995; Jahan, 2014; Francalanci et al., 2008; Patel & Kumar, 2023).

4.3.2. Based on the permeability

Notable findings emerged from comparing different scour reduction strategies based on permeability sets. The analysis revealed significant reductions in the maximum scour depth at spur dike-1 for conditions without seepage. Specifically, when using permeability Set-B, there was a decrease of 37.6%, while employing permeability Set-C resulted in an even more substantial reduction of 55.2% compared to impermeable spur dikes (Set-A). This trend persisted across different scenarios, such as the V_{S1} and V_{S2} conditions, where significant decreases in scour depth were observed at spur dike-1. When considering V_{S1}, applying permeability Set-B led to a reduction of 38.5%, and employing permeability Set-C resulted in a reduction of 42.4% compared to impermeable spur dikes (Set-A). Similarly, for the V_{S2} treatment, the use of permeability Set-B yielded a 35.3% reduction, while permeability Set-C achieved a 47.4% reduction compared to that of impermeable spur dikes (Set-A).

Minimal scouring was detected at spur dike-2 using Set-A under seepage and no-seepage conditions. However, under no-seepage conditions at this location, the use of permeability Set-C reduced the scour depth by 29.9% compared to that of Set-B. Similarly, under the V_{S1} condition at this site, the scour depth was 31.7% lower when using permeability Set-C compared to that of Set-B. Likewise, in the V_{S2} condition at this site, employing permeability Set-C resulted in a 29.7% reduction in scour depth compared to that of Set-B.

Regarding permeability, the most significant local scouring occurred around the tip of the first spur dike wing (spur-1) in Set-A, when impermeable spur dikes were used. However, in Set-B, where the first spur dike was permeable at 60%, the maximum scour depth shifted to the next spur dike while decreasing around the first spur dike. In Set-C, where the first spur dike was permeable at 60% permeability and the second spur dike at 30% permeability, the maximum scour depth was reduced around both spur dikes 1 and 2, with minor hollows observed near the third spur dike.

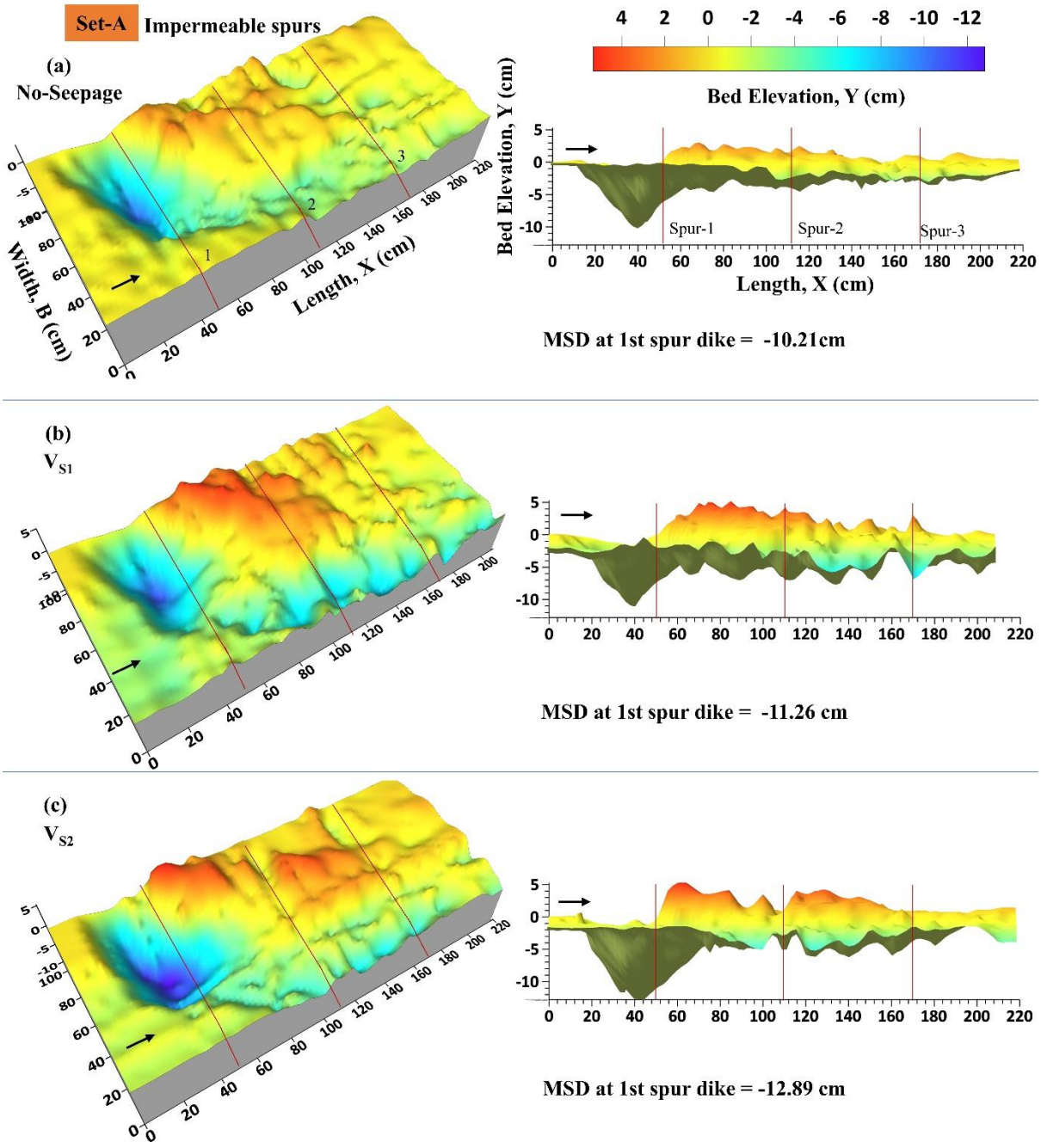

Figure 4.1 Bed morphology with local scour depth around spur dike Set-A under three conditions: no seepage (a), seepage velocity V_{S1} (b), and seepage velocity V_{S2} (c), along with their respective longitudinal profiles.

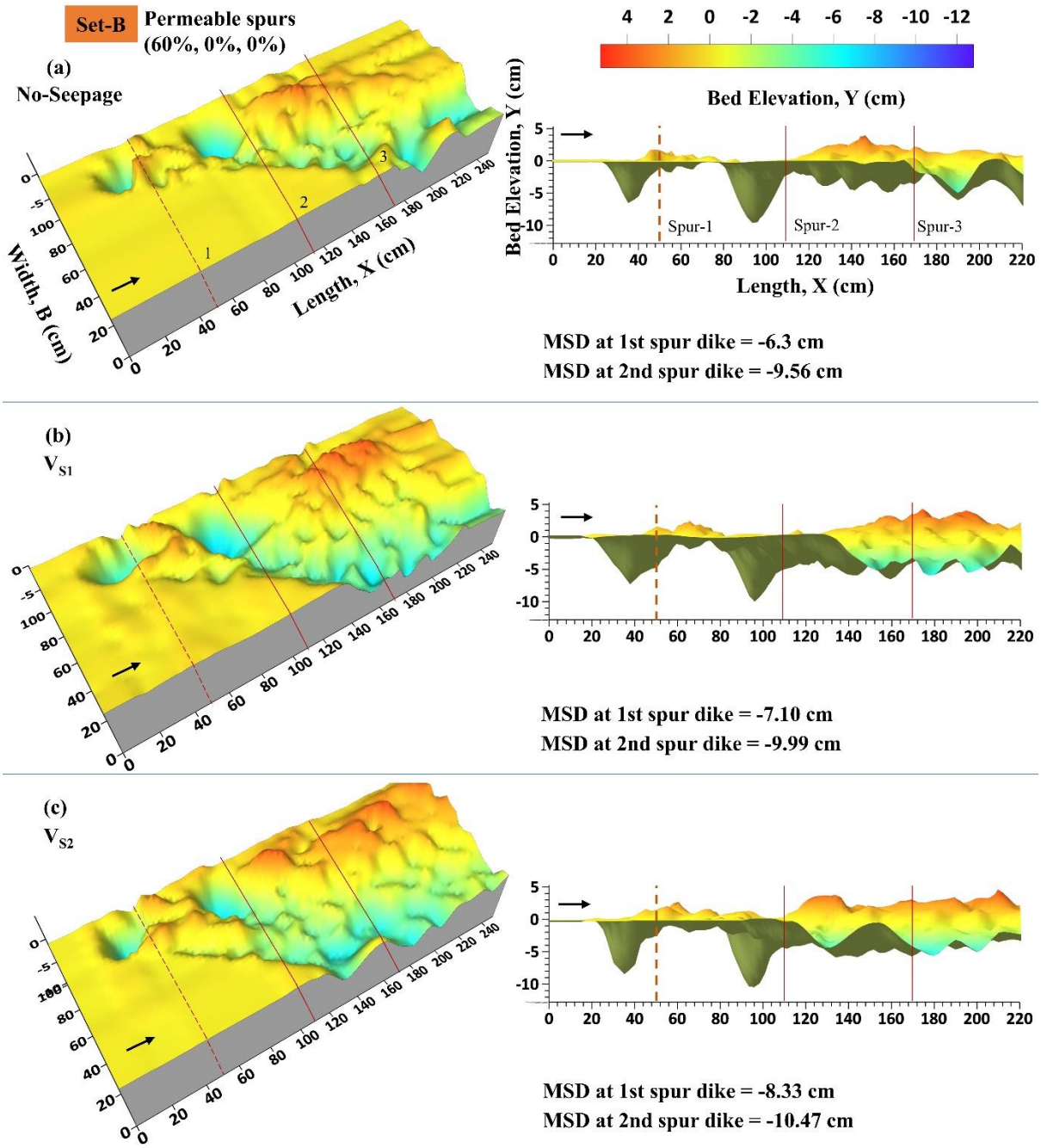

Figure 4.2 Bed morphology concerning the local scour depth around spur dike Set-B under three conditions: no seepage (a), seepage velocity V_{S1} (b), and seepage velocity V_{S2} (c), along with their respective longitudinal profiles.

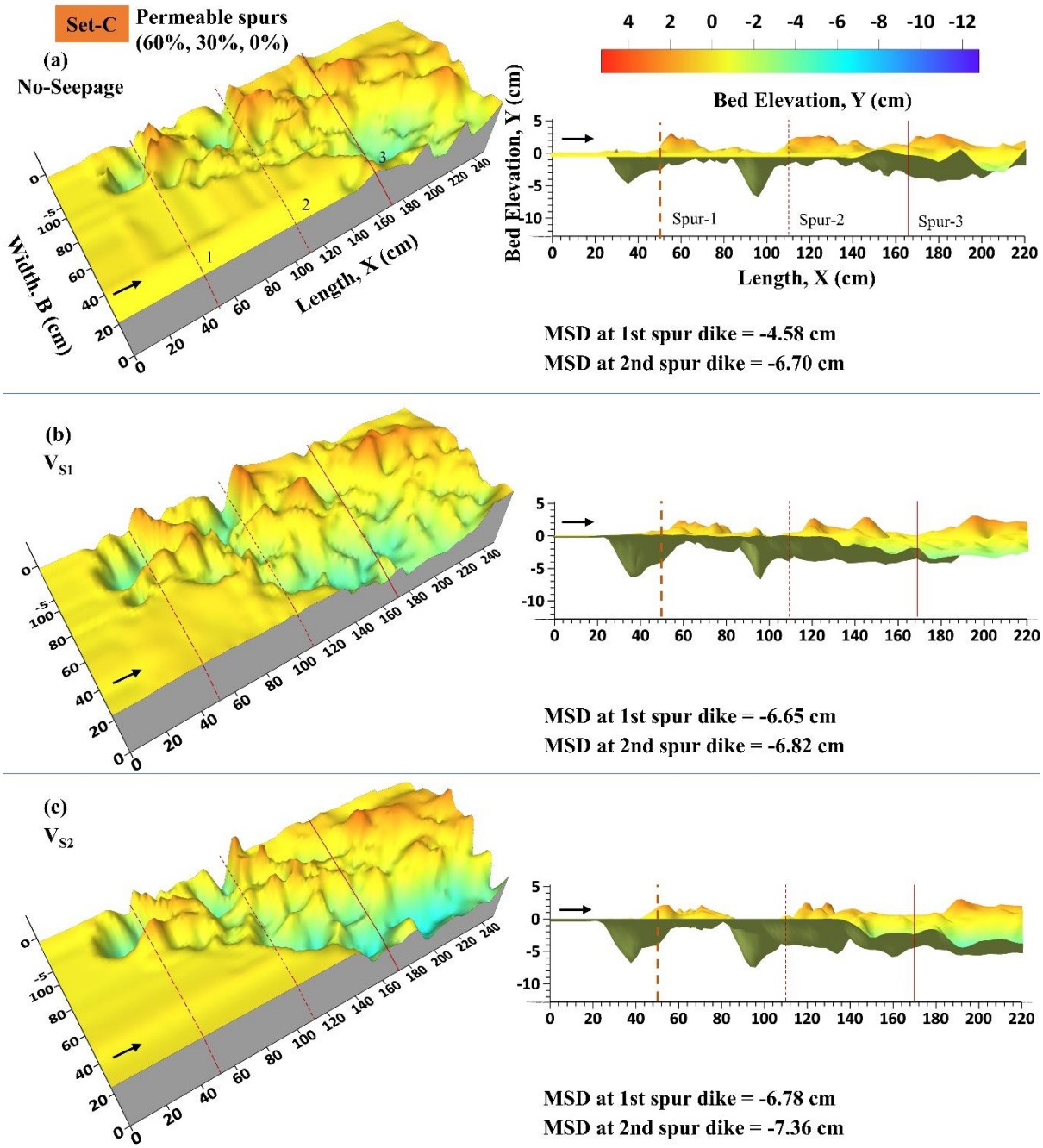

Figure 4.3 Bed morphology concerning the local scour depth around spur dike Set-C under three conditions: no seepage (a), seepage velocity V_{S1} (b), and seepage velocity V_{S2} (c), along with their respective longitudinal profiles.

4.4 Velocity

The contour plots in Figure 4.4 depict the streamwise velocity distribution near the water surface, particularly at a depth of z/h = 0.50. These plots focused on how spur dike zones influence flow velocity. The experimental analysis examined two crucial zones: the primary

zone (main flow zone) and the obstacle zone. These zones play a pivotal role in understanding flow dynamics. The main flow zone ranges from y = 0 cm to y = 80 cm and is characterized by the most pronounced flow. Water movement accelerates notably through the wing edges of spur dikes, leading to flow convergence. Conversely, the obstacle zone spans from y = 80 cm to y = 100 cm and experiences altered flow dynamics due to the obstructive nature of spur dikes, resulting in constrained flow behavior. The measurements were conducted across three permeability sets (Set-A, Set-B, and Set-C) under three distinct conditions: no-seepage, V_{S1}, and V_{S2}.

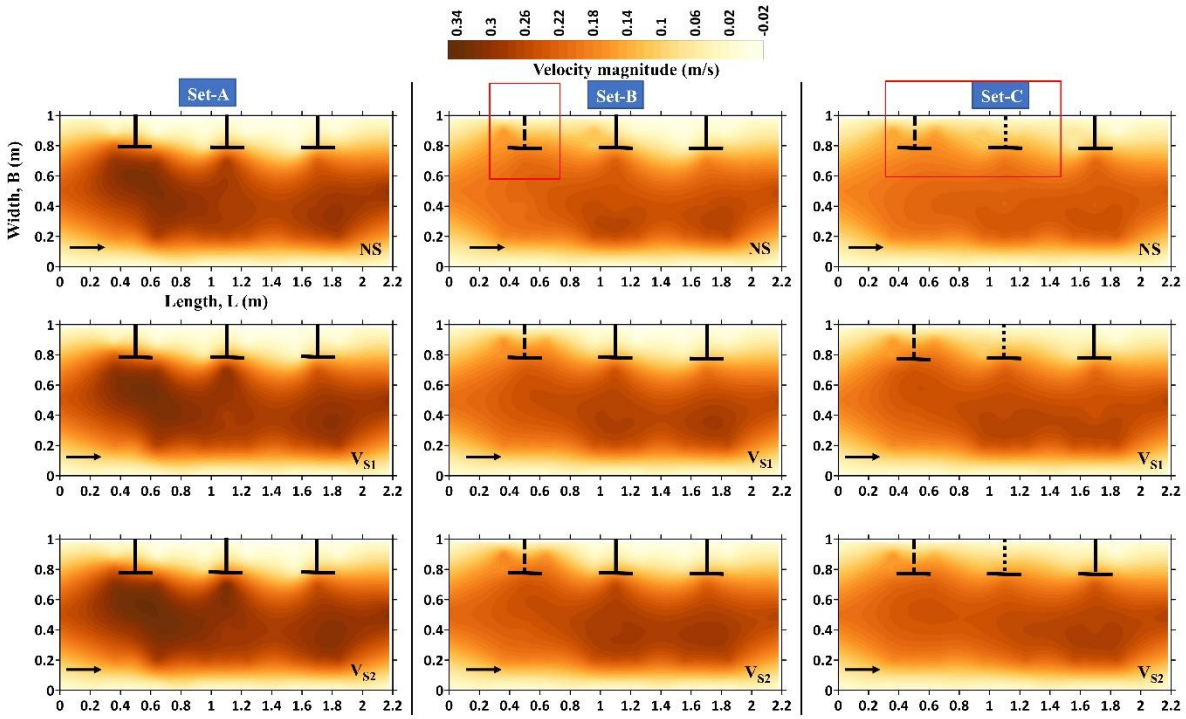

Figure 4.4 Velocity magnitude in the streamwise direction, particularly near the water surface at z/h = 0.50, with different permeability sets, i.e., Set-A, Set-B, and Set-C, and seepage conditions, no-seepage, V_{S1}, and V_{S2}.

In Set-A, impermeable spur dikes are employed, and the flow intensity peaks around the initial spur dike and gradually diminishes downstream through successive dikes. Flow redirection and constriction through spur dike wing edges significantly increase the velocity within the main

flow zone, with the maximum velocity observed in this area. However, the velocity of the obstruction zone decreased due to the disruption caused by the spur dikes.

In Set-B, where the initial spur dike permeability was set at 60%, there was a noticeable increase in velocity magnitude between spur-1 and spur-2 (obstruction zone) due to the increase in velocity and increased permeability. This disruption alters flow dynamics and aids in reducing turbulence generation around the edge of spur-1. Consequently, the flow encounters less resistance and disturbance as it interacts with the structure of the spur dike, leading to a more consistent and controlled flow pattern.

As the flow proceeded, the flow became redirected and constrained by the edge of spur dike-2. This interaction results in an increase in flow velocity within the main flow zone. Consequently, the maximum scour depth relocates to the subsequent spur dike (spur-2), with a decrease observed around the initial spur dike. Following passage through the spur dike field, the flow velocity gradually diminishes as the dike traverses all the spur dikes.

Set-C features a configuration in which the first spur dike possesses a permeability of 60%, and the second spur dike has a permeability of 30%. The higher permeability in Set-C weakened mass and momentum exchange in the flow, altering flow dynamics and reducing turbulence around the edges of Spur-1 and spur-2. This is due to the improved ability of the porous structure to allow water passage, thereby disrupting flow dynamics and decreasing turbulence generation. Consequently, there was a reduction in the maximum scour depth around both the first and second spur dikes, with minor depressions noted near the third impermeable spur dike.

In the obstruction zone, the fluctuations in velocity near the channel boundary are relatively low. This area undergoes less significant changes in velocity magnitude than the more dynamic

alterations observed within the main flow zone. Seepage rates accentuate this effect of velocity magnitude in all the sets.

4.4.1 Velocity profile at the location of the maximum scour depth (A1)

The previous investigations revealed that the most significant changes in flow patterns and variations in scour depth occurred primarily around the initial spur dike. To investigate the influence of permeability and downward seepage on the physical behavior of scour formation, we focused on a critical location (A_1) around spur dike-1. This location exhibited the deepest scouring observed in the impermeable spur dike Set-A.

4.4.1.1 Near the water surface

Near the water surface (z/h=0.50), as shown in the velocity profile in Figure 4.5 (a, b, c), upon analyzing the no-seepage condition, it was observed that the velocity magnitudes decreased by 27.7% for Set-B and 36.6% for Set-C compared to Set-A. Similarly, under the seepage condition (V_{S1}), there was a reduction in the velocity magnitude of 26.3% for Set-B and 32.4% for Set-C, while under the seepage condition (V_{S2}), the velocity magnitude decreased by 27.1% for Set-B and 32.5% for Set-C.

However, in terms of seepage (Figure 4.5 p,q,r), the velocity magnitude increases by 2% (V_{S1}) and 5.5% (V_{S2}) compared to that in the no-seepage conditions. Similarly, for Set-B, where permeability is introduced, there is a notable increase in velocity of 3.8% (V_{S1}) and 6.4% (V_{S2}). For Set-C, the velocity increases by 7% (V_{S1}) and 10.5% (V_{S2}).

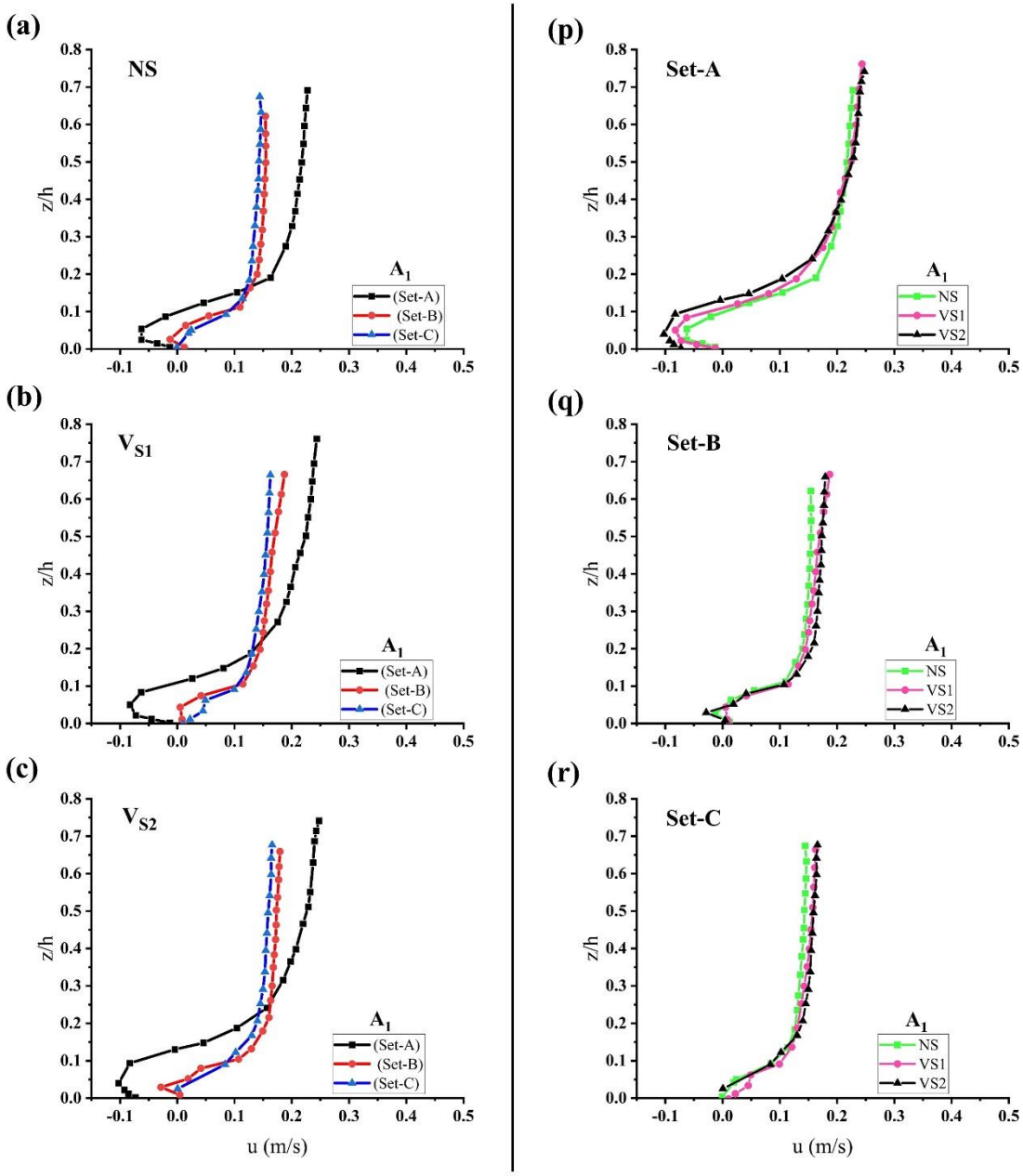

Figure 4.5 Velocity profile at location (A_1) under three seepage conditions: no seepage (a), seepage velocity V_{S1} (b), and seepage velocity V_{S2} (c) and three permeabilities, Set-A (p), Set-B (q), and Set-C (r).

4.4.1.2 Near the channel bed

Based on the permeability, the analysis of the velocity magnitudes near the channel bed (at *z/h* = 0.05) revealed significant differences in performance among the different sets of spur dikes across the various conditions. The impermeable spur dike Set-A exhibits negative values near the channel bottom, and this adverse impact on velocity becomes more pronounced with

increasing seepage rate. However, compared to Set-A under no-seepage conditions, Set-B demonstrated a substantial 79.03% increase in velocity magnitude, suggesting that including permeable spur dikes may significantly enhance flow. Set-C exhibited an even greater increase in velocity magnitude of 138.71% relative to Set-A, indicating that the permeable structures within this set may be even more effective at enhancing flow dynamics.

With V_{S1} seepage, Set-B continues to show an increase in velocity magnitude of 106.10%. Set-C, on the other hand, shows an even greater increase of 159.76% in velocity magnitude compared to Set-A under the same seepage conditions, suggesting that permeable dikes may be even more effective at facilitating flow with the introduction of seepage.

As seepage levels increase to those of $V_{S2,}$ an impermeable spur dike, Set-B, experiences a further increase in velocity magnitude, marking a significant increase of 118.63% compared to Set-A. Meanwhile, Set-C maintains its trend of heightened velocity magnitude, registering a 181.76% increase compared to Set-A, even as seepage levels intensify.

In impermeable spur dikes, as the seepage rate increases, the adverse effect on flow velocity intensifies (the flow becomes more reversed at the scour depth position), leading to an enhanced scour depth with potentially negative flow dynamics. Moreover, the observed increases in velocity magnitude indicate the potential effectiveness of permeable spur dikes for evaluating flow dynamics. Under no-seepage conditions, both Set-B and Set-C exhibit substantial increases in velocity magnitude compared to Set-A, suggesting that including permeable structures in spur dikes may enhance flow, with Set-C showing a more pronounced effect.

Based on seepage, for Set-A, the V_{S1} seepage condition experiences a 32.26% decrease in velocity magnitude compared to that of no seepage. Compared with no seepage, the V_{S2} seepage

condition experiences a 64.52% decrease in velocity magnitude. In comparison, Set-B and Set-C experience relatively low increases in velocity magnitude.

Impermeable spurs tend to reduce velocities, and this effect can sometimes be negative, particularly when seepage is introduced. The presence of impermeable spurs leads to resistance to water flow, reducing velocities near the channel bed. Additionally, as seepage infiltrates through impermeable spurs, the adverse effect on flow velocities intensifies, leading to further reductions and potentially negative flow dynamics.

4.5 Conclusion

The permeability of spur dikes plays a major role in altering the bed morphology and flow pattern around the spur dikes. The flow experienced less resistance and disturbance when it passed through the porous formation of the structure. The permeability reduces the mass and momentum exchange. Thus, it mitigates the disturbance of flow dynamics and turbulence generation. This turbulence reduction influences the spur dikes' stability and their hydraulic performance. Thus, potentially improving their effectiveness in mitigating scouring.

At location (A_1) near the channel bed, a distinct behaviour is observed where downward seepage interacts with the channel bed, and its effect becomes more pronounced. As water encounters a spur dikes, it restricts that flow and generates a curved bow wave on its surface. This wave forced the water downward toward the structure's base, resulting in a reversal flow with a negative value near the channel bed. With the application of seepage, this reversal flow becomes more prominent. Due to this reversal flow, horseshoe vortices and eddies are formed. Thus, it detaches the particle from the base of the structure and transports it downstream to the structure. A downward seepage further accelerates the detachment process.

Studies show that higher seepage rates result in more extensive scouring, which distorts riverbed and channel morphology. Seepage makes Sediment particles more detachable,

resulting in deeper scour depressions on the riverbed. When managing river dynamics and erosion, it is essential to consider seepage conditions.

Studies have shown that impermeable spur dikes are particularly susceptible to local scouring, while permeable configurations reduce scour depths. Hence, the permeable combinations could effectively counteract turbulence. Implementing permeable spur dikes could, therefore, be an effective strategy for mitigating scouring and enhancing the stability of spur dikes.

5 Optimal spur dike orientation for scour mitigation under downward seepage conditions[7]

5.1 Introduction

Spur dikes are hydraulic structures strategically positioned along the banks of rivers or streams for river training, and riverbank erosion protection. These structures can be positioned in different orientations, such as angled upstream, downstream, or perpendicular to the main flow direction. The proper alignment of spur dike is critical for streambank stabilisation and flood management because the orientation affects flow patterns, scouring, and downstream sedimentation processes. The scour formed by turbulent eddies can be especially dangerous if it threatens the stability of the spur dike or the riverbed downstream of the dike. Excessive scour can cause the dike to fail, resulting in floods and other consequences in extreme circumstances. As a result, it is critical to design and construct spur dikes properly to reduce the possibility of excessive scour while also ensuring their stability and safety.

There are several critical factors to consider when designing spur dikes, such as the shape, length, orientation, and submergence of spur dikes. Also, the spacing between each spur dike, the channel cross-section, the construction material, and the riprap size used are important design factors for employing spur fields (Yossef, 2002; Akbari et al., 2021). The orientation of these structures needs to be carefully considered based on the conditions and constraints of each project. There is an ongoing conflict regarding whether these spur dikes should face upstream or downstream.

[7] Patel, H.K., & Kumar, B. (2024). Optimal Spur Dike Orientation for Scour Mitigation under Downward Seepage Conditions. Journal of Hydrology and Hydromechanics, 72(2), doi.org/10.2478/johh-2024-0019

Researchers who favour upstream orientation claim that the dike's angle ($\theta < 90°$) deflects the flow away from the dike, resulting in less sedimentation and requiring less protection on the bank and upstream side of the dike. Studies have shown that upstream-oriented dikes reduce scour depth and offer better channel bank protection (Attia & Saied, 2006; Elsaiad & Elnikhely, 2016; Nath & Misra, 2017; Indulekha et al., 2021). Alvarez (1989) recommends angles between 70° and 90° for best protection, while Ezzeldin et al. (2007) found that an angle of 30° is most effective at reducing scour depth and protecting banks upstream.

Elsaiad and Elnikhely (2016) report that decreasing the angle of inclination from 90° to 25° reduces relative maximum scour depth by 55%. Nath and Misra's (2017) laboratory experiments show that an inclination angle of 60° results in the lowest scour depth for a given opening ratio and flow conditions. Indulekha et al. (2021) identified 45° angled groynes as ideal for controlling velocity in meandering rivers. However, according to the findings (Jafari & Sui, 2021), increasing the dike angle upstream can lead to increased scour depth. According to their study, each 10° increase in dike angle (from 45° to 90°) resulted in a proportional rise in scour depth, often between 5% and 10%.

Conversely, those favouring downstream orientation ($\theta > 90°$) contend that angling the dike in the downstream direction minimises turbulence and scour depths at the dike's downstream end. Furthermore, the more the dike is turned downstream, the greater the distance of the scour hole from the dike, which reduces the likelihood of debris and ice accumulation. For bank protection, it was advised to use an angle ranging from 100° to 120° (Kanungo, 1956; Mamak, 1964). Tison (1962) found that upstream-oriented dikes had the most remarkable maximum scour depth while downstream-oriented dikes had the lowest. Richardson and Simons (1984) suggested perpendicular placement but also noted the possibility of using angles between 100° and 110° to control flow. Spur dikes with angles greater than 90° help protect river banks by

allowing silt to settle and contribute to bank stability (Brown, 1985; Kuhnle et al., 2002). Krishna Prasad et al. (2016) proposed that an angle of 135° minimises erosion and ensures bank protection.

The question of how to position spur dikes still remains a subject of ongoing debate, and there is a divide in opinion to support any particular orientation. One frequently proposed strategy is positioning spur dikes at right angles to the flow lines. Garde et al. (1961) found that the maximum scour depth occurs when the spur dike is inclined at 90°. They also found that the scour depth was shallower for upstream and downstream inclinations. On the other hand, Kuhnle et al. (2002) discovered that 90° angled spur dikes caused the least scouring, while 135° angled ones caused the most erosion. Koken (2011) defined a new scour mechanism for 60° angled spur dikes and found the maximum possible scour with 90° angled spur dikes. Furthermore, Indulekha et al. (2021) suggested that within the groynes oriented at 90°, significant variations in properties such as pressure and turbulent kinetic energy were observed within the spur field. These variations underscored the dynamic and complex nature of flow patterns around these structures, indicating the potential for significant scouring effects.

Despite significant efforts to understand and control scour depth in alluvial channels, predicting it remains uncertain. Scour depth prediction becomes more complex when downward seepage occurs through permeable boundaries of the alluvial channels. As per earlier investigations, seepage's downward movement significantly influences channel configuration (as mentioned in section 1.2). However, as per the existing research, the assessment of local scour depth around angled spur dikes with downward seepage has yet to be analysed.

Thus, the fundamental goal of this research is to investigate how orientations of spur dikes affect the scouring process with downward seepage to determine the most effective alignment among the numerous possibilities available. This study presents the impact of downward

seepage on the variation in bed morphology and local scour pattern around three orientations of rectangular-shaped spur dikes, i.e., perpendicular, upstream, and downstream angled. It establishes the best orientation of the spur dike that is least affected by the downward seepage.

5.2 Temporal bed morphology and scour depth

This experimental study aimed to gain insights into the temporal variation in bed morphology and scours around rectangular-shaped spur dikes with different orientations. Scour depth development typically starts at the tip of a spur dike.

Concerning the specific outcomes corresponding to each orientation angle, assessing scour depth development around the initial spur dike after 2 hours (Figure 5.1) revealed varying measurements. The scour depth was initially recorded at 5.87 cm for the 60º orientation (labelled as (a)), marking an increase to 8 cm within the 90º orientation (denoted as (b)), and a measurement of 5.56 cm was noted for the 120º orientation (designated as (c)).

The measurements exhibited further variations after observing the evolution of scour depth after 12 hours (Figure 5.2). At this stage, the scour depth was measured at 8.57 cm for the 60º orientation (labelled as (a)), escalating to 10.8 cm within the 90º orientation (depicted as (b)), and observed at 7.32 cm for the 120º orientation (denoted as (c)).

Subsequently, at the 24-hour mark (Figure 5.3), the scour depth was registered at 9.80 cm for the 60º orientation (labelled as (a)), increased to 12.67 cm within the 90º orientation (indicated as (b)), and stood at 9.33 cm for the 120º orientation (designated as (c)).

Finally, when considering the 24-hour duration with the application of seepage (depicted in Figure 5.4), the scour depth measurements revealed additional variations. At this point, the scour depth was measured at 11.03 cm for the 60º orientation (labelled as (a)), escalated to

14.63 cm within the 90º orientation (denoted as (b)), and recorded at 10.26 cm for the 120º orientation (designated as (c)).

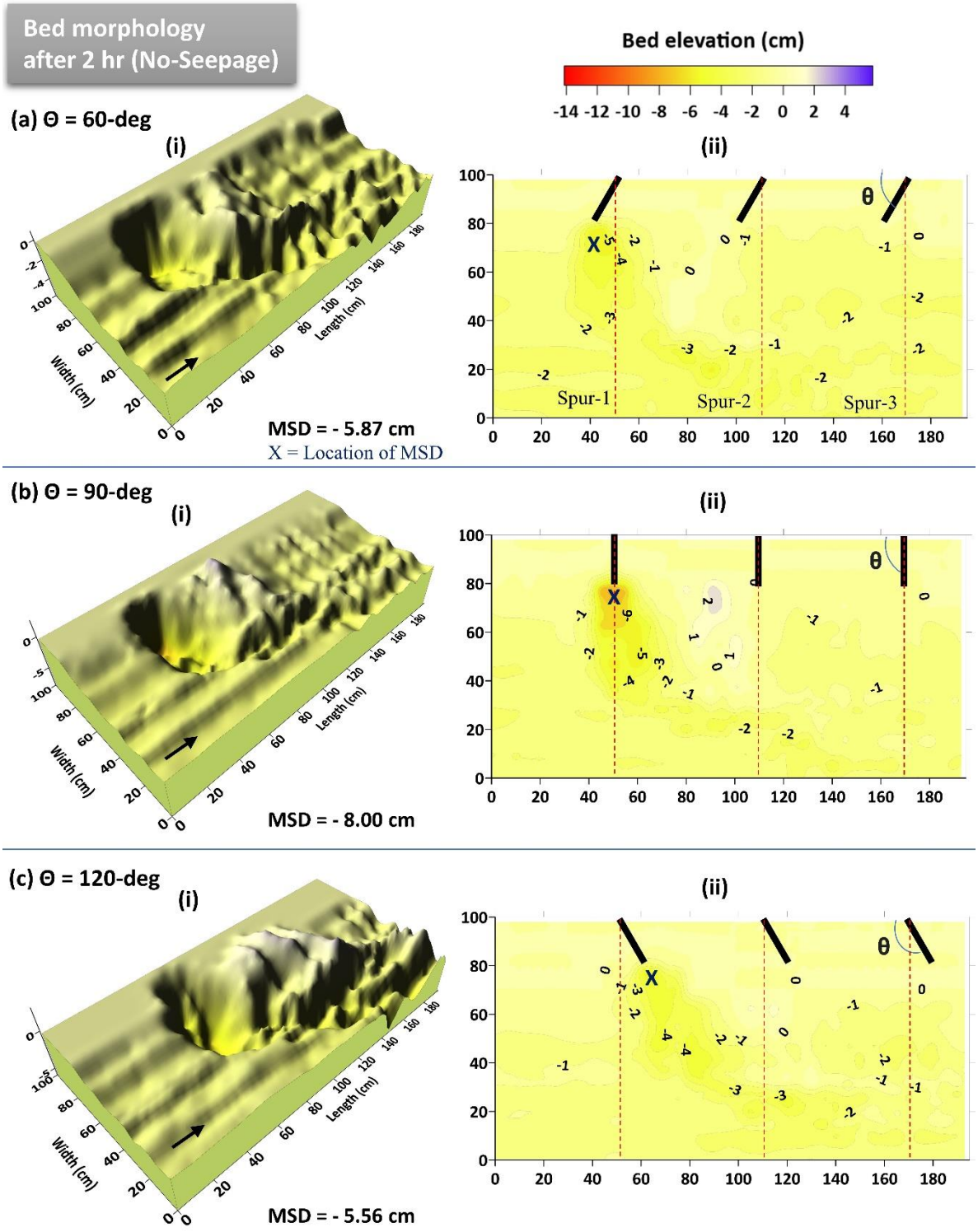

Figure 5.1 Bed morphology with scour depth evolution around oriented spur dikes 60º (a), 90º (b), and 120º (c) after 2 hours and their respective contour plots.

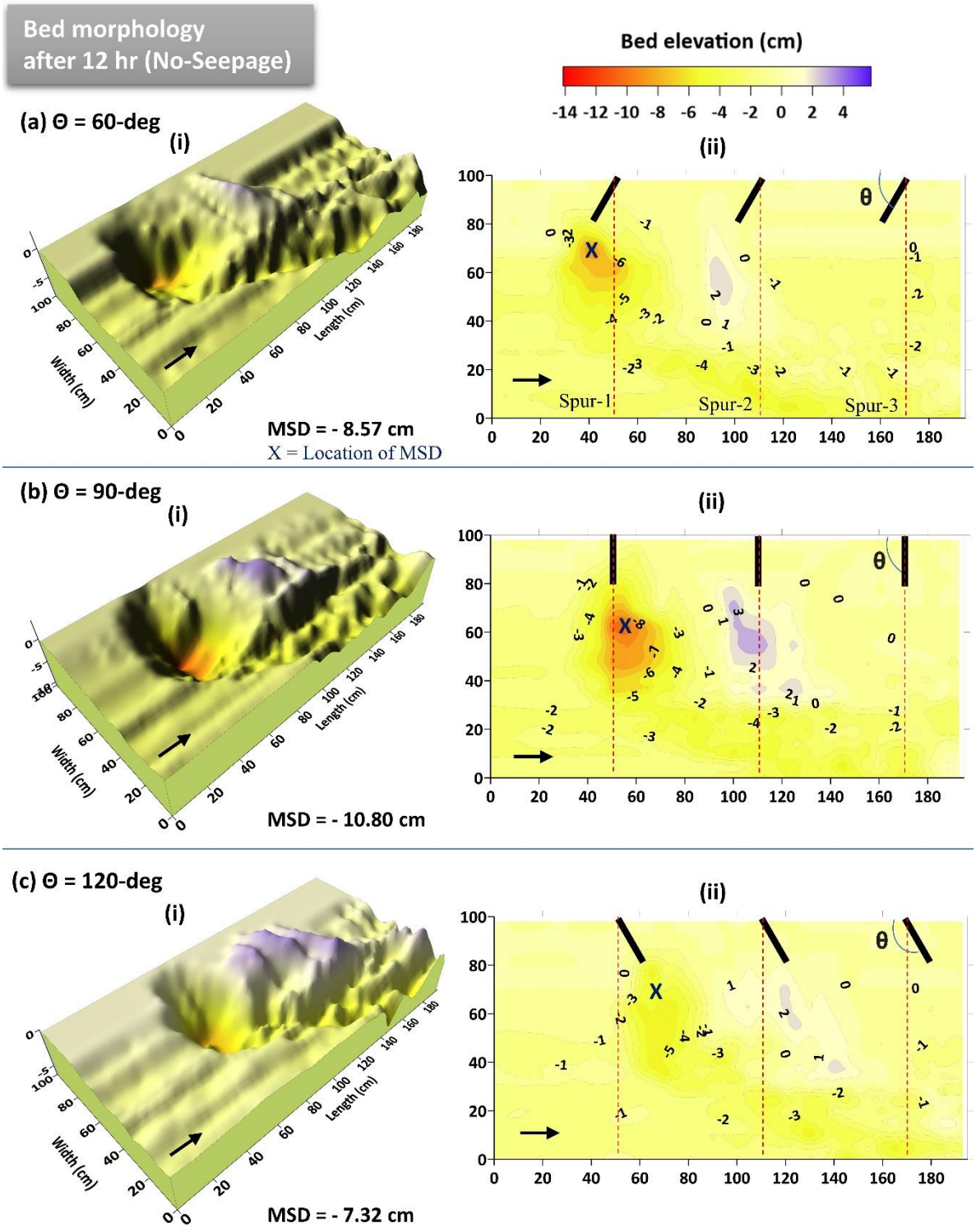

Figure 5.2 Bed morphology with scour depth evolution around oriented spur dikes 60º (a), 90º (b), and 120º (c) after 12 hours and their respective contour plots.

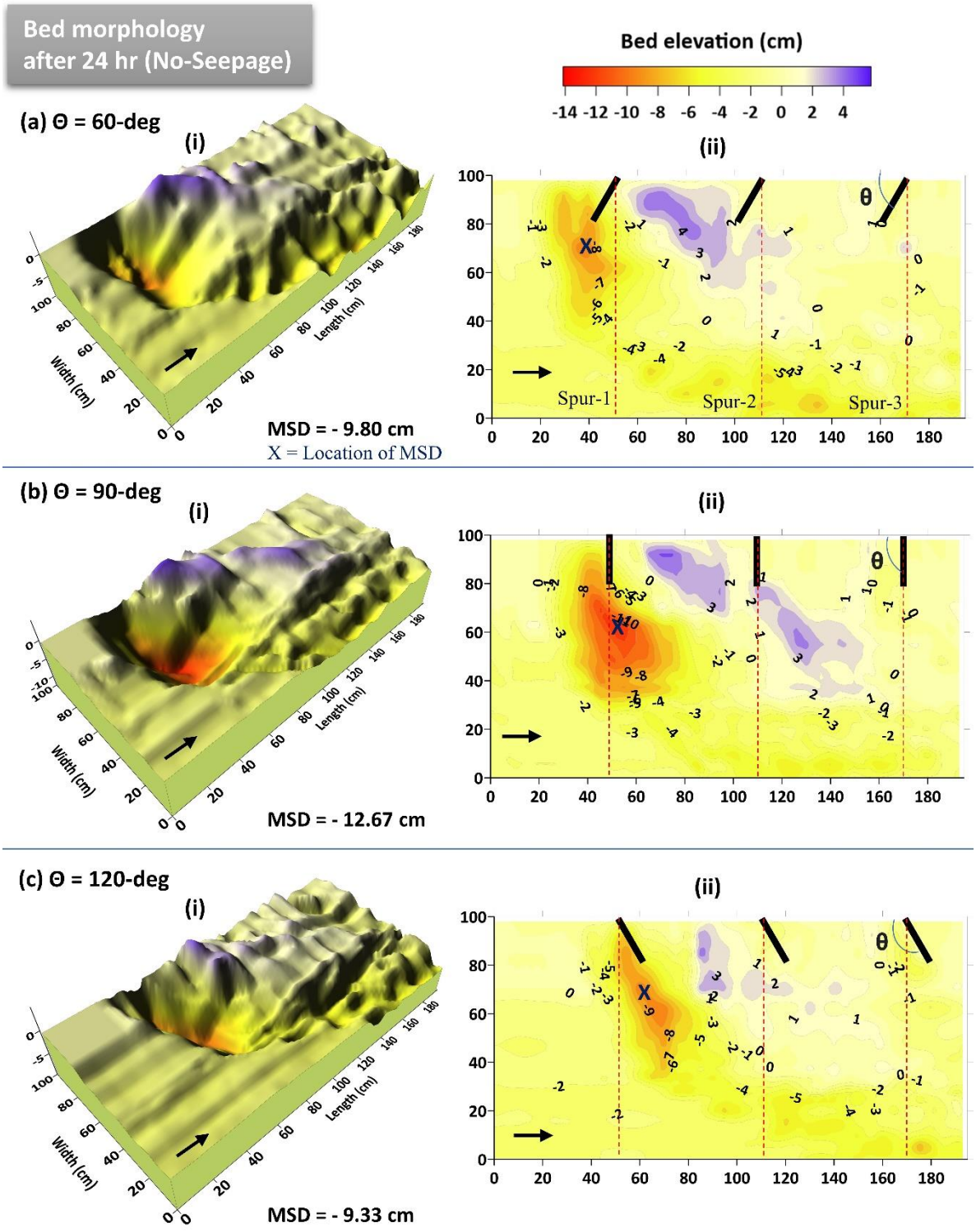

Figure 5.3 Bed morphology with scour depth evolution around oriented spur dikes 60º (a), 90º (b), and 120º (c) after 24 hours and their respective contour plots.

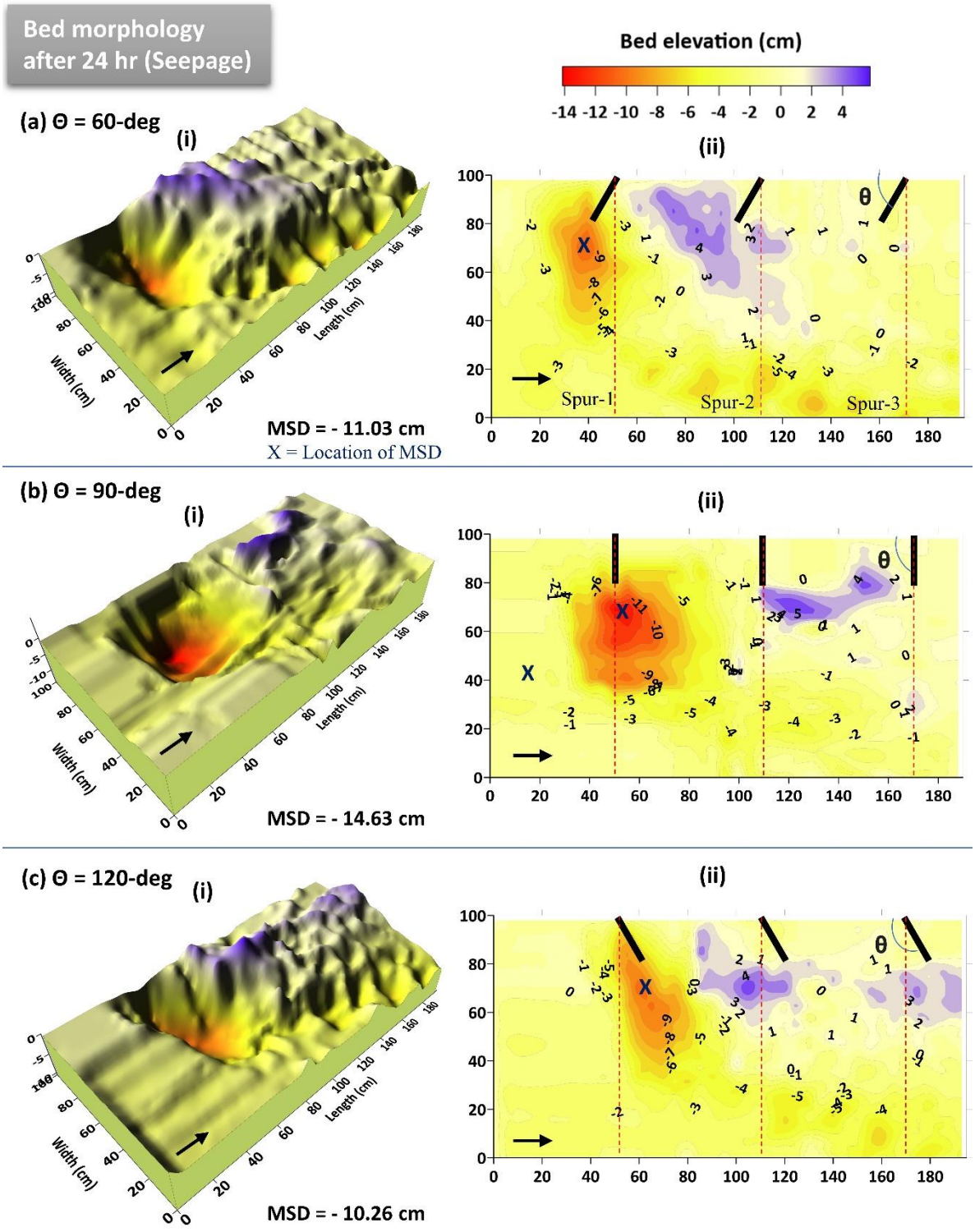

Figure 5.4 Bed morphology with scour depth evolution around oriented spur dikes 60º (a), 90º (b), and 120º (c) after 24 hours (with seepage) and their respective contour plots.

When comparing the effects of different orientations (60º, 90º, and 120º), the research findings revealed notable variations in maximum scour depth. The scour depth at a 90º orientation increased by 36.2 % and 43.8 % after 2 hours, 26 % and 47.5 % after 12 hours, 29.2 % and 35.7 % after 24 hours, and 32.6 % and 42.5 % after 24 hours (with seepage), in comparison to the 60º and 120º orientations, respectively.

Comparing the scour depths with and without seepage (Figure 5.5), it is evident that seepage significantly impacts the scour depth at different orientation angles. For the 60º orientation, the scour depth increased by 12.5% (from 9.80 cm to 11.03 cm) with seepage. For the 90º orientation, the scour depth increased by 15.4% (from 12.67 cm to 14.63 cm) with seepage. For the 120º orientation, the scour depth increased by 9.96% (from 9.33 cm to 10.26 cm) with seepage. This comparison clearly shows that the presence of seepage consistently results in increased scour depths across all orientations, with the highest percentage increase observed at the 90º orientation. This indicates that the effect of seepage is more pronounced at the 90º orientation compared to the 60º and 120º orientations. The least increase in scour depth was observed at the 120º orientation, highlighting a relatively lower impact of seepage at this angle.

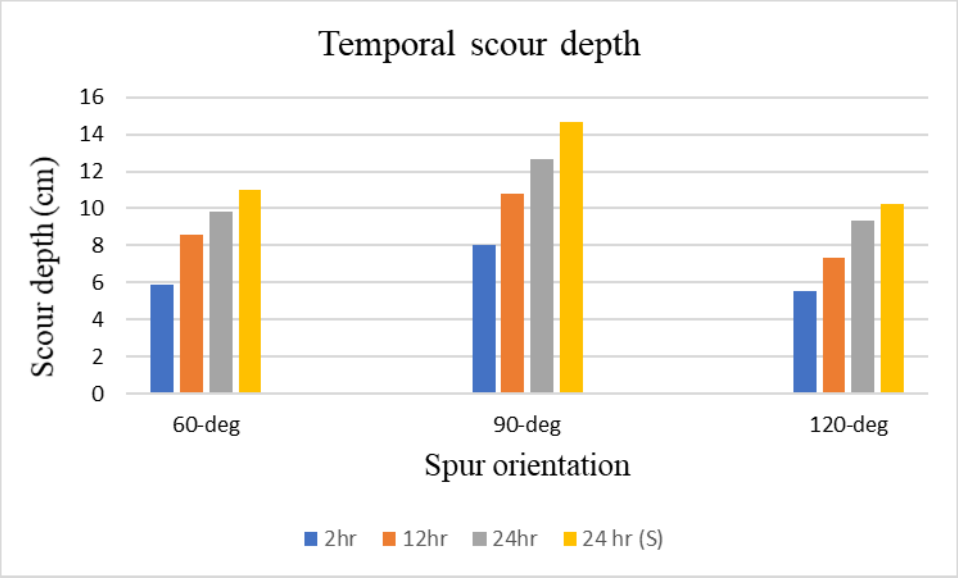

Figure 5.5 Temporal variation of scour depth with and without seepage for different orientations angle

5.3 Scour Hole Characteristics

The longitudinal scour variation depicted in Figure 5.6 shows that the depth of scour formation depends on the orientation provided to divert the flow and the seepage condition. Data for the longitudinal profile were collected at the streamwise section for all orientations (at 0.70 m from the right bank), where the maximum scour depth was observed.

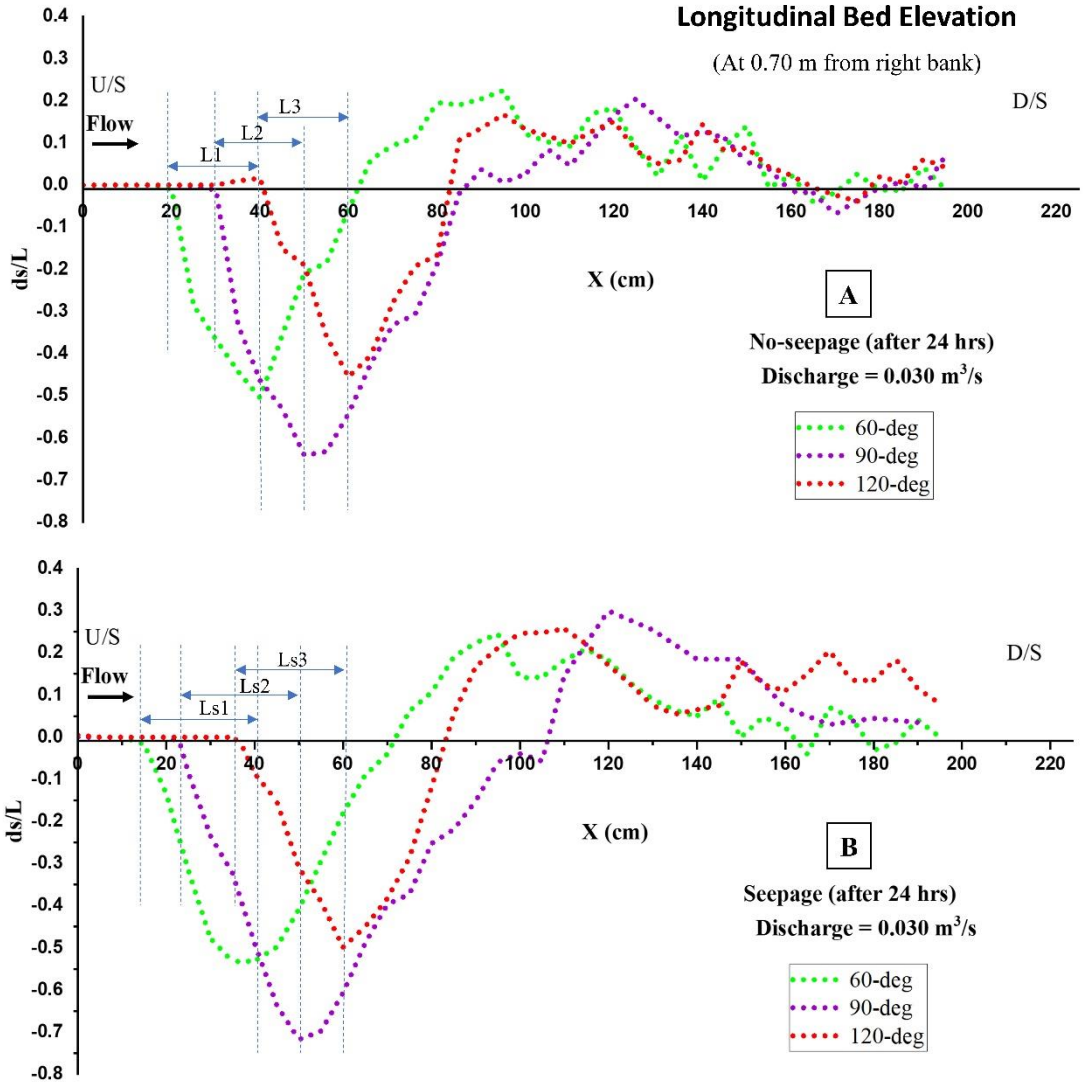

Figure 5.6 Longitudinal variation of scour formation under various spur dike orientations (A) without seepage and (B) with seepage condition. Here, the maximum scour depth (*ds*) is non-dimensionalized with the projected length of the spur dike (*L*).

As the water reached the spur dike zone, the maximum water was diverted through the edge of the spur dike. While the obstructed water stagnated and created a bow vortex at the water's

surface (Norouzi et al., 2023). The developed bow vortex pushes water downward towards the base of the spur dike, where it forms a horseshoe vortex at the base (Zhang & Nakagawa, 2008; Ezzeldin, 2019; Patel & Kumar, 2023; Patel et al., 2023b). This clockwise force of the horseshoe vortex (swirling currents) is crucial for detaching sediments from the base of the structure. The movement of these detached particles creates scour at that position. The detached material is then carried forward through the wake vortex and settles downstream, where lower velocity is achieved. Downstream of the scour hole, a dune-like formation of sand deposition of detached material accumulated, where the flow strength is reduced. This deposition is indicative of the material transported from the scour hole and highlights the dynamic nature of sediment transport and deposition around spur dikes. This dune formation is linked to the findings of Roushangar et al. (2024), who observed that eddy currents created dunes with a height proportional to the scour depth in the spur field.

The increase in scour depth at a 90º orientation can be attributed to the significant obstruction and strong horseshoe vortices formed at this angle, which exacerbate the scouring process. Conversely, the 120º orientation allows for smoother, more streamlined flow with less separation, resulting in weaker horseshoe vortices and reduced turbulence, thereby minimizing scour depth. The study's results showed that the orientation angle of 90º generated the highest scour depth, while the least scour depth was found with an orientation angle of 120º. The orientation of the spur dikes significantly influences flow patterns, leading to sediment detachment, transport, and deposition in particular areas downstream of the spur dike configuration.

The study also examined the characteristics of the scour hole formed at different orientations. The scour hole's diameter gradually extends from the edge of the spur dike. The longitudinal extents of the scour diameter (as shown in Fig. 5.6), which refers to the distance between the

upstream edge of the scour hole to the edge of the spur dike tip, were measured for both no-seepage and seepage conditions. The measurements were found to be 19 cm ($L1$), 21 cm ($L2$), and 16 cm ($L3$) for no-seepage conditions, and 23 cm ($Ls1$), 26 cm ($Ls2$), and 21 cm ($Ls3$) for seepage conditions, at orientations of 60º, 90º, and 120º respectively. The transverse extent of the scour hole from the spur dike tip observed the dimensions of 38 cm, 40 cm, and 26 cm for no-seepage and 39 cm, 42 cm, and 28 cm for seepage condition with an orientation of 60º, 90º, and 120º, respectively.

The measurements indicate that the 90º orientation not only results in the deepest scour depth but also the most extensive scour hole dimensions. These dimensions improved further with downward seepage.

These findings underscore the importance of considering seepage effects in assessing and mitigating scour depth in various orientations. Downward seepage modifies the flow dynamics by disrupting the cohesion between sediment particles and the riverbed, causing their detachment and transport from the riverbed. This increased force results in deeper scour depressions, highlighting the importance of accounting for seepage in spur dike design. Furthermore, the study revealed that the scour hole diameter and entire channel morphology is substantially affected by seepage.

5.4 Conclusion

This experimental investigation explored temporal changes in bed morphology and scour concerning rectangular-shaped dikes' varying orientation angles (60°, 90°, or 120°). It assessed the viability of different spur dike designs by observing scour conditions over time (after 2, 12, and 24 hours) in correlation with downward seepage.

The scour depth initiation starts at the tip of a spur dike, where water flow turbulence forms a horseshoe vortex, detaching bed material. The research findings suggest that a 60º orientation

induces significant flow deflection, as its sharp angle enhances turbulent flow and promotes the formation of horseshoe vortices. This results in substantial scouring due to the high-pressure difference between upstream and downstream. On the other hand, a 90º orientation causes maximum obstruction, leading to strong horseshoe vortices and a large stagnation region, creating a high-pressure zone at the upstream end. This orientation leads to maximum scour depth, characterized by deep, symmetrical and larger scour holes around the base of the dike due to the intense turbulent flow pattern. Meanwhile, a 120º orientation allows for smoother, more streamlined flow with less separation, resulting in weaker horseshoe vortices and reduced turbulence. The low-pressure difference between upstream and downstream observed with this orientation leads to the least scour depth, effectively mitigating scouring.

The downward seepage exerts a stronger force on the sediment particles by altering the flow dynamics and increasing the water velocity near the riverbed. This increased force disrupts the cohesion between particles and the riverbed, facilitating their detachment and transport. Consequently, the deeper scour depressions directly result from this downward seepage phenomenon.

This study highlights the critical importance of accounting for seepage and the orientation of spur dikes in the design process. In the presence of seepage, maximum scour depth increases by 12.5%, 15.4% and 9.96% for 60º, 90º and 120º orientations, respectively, compared to existing guidelines (no-seepage) for different orientations of spur dikes. However, the least increase was observed at the 120º orientation, highlighting a relatively lower impact of seepage at this angle. Therefore, designing about 15% deeper spur dike foundations is recommended to prevent failure risks due to downward seepage. Additionally, a downstream orientation is advised to create smoother flow patterns, minimize scour, and enhance the structural integrity and longevity of the dikes. These considerations are essential for effectively managing and mitigating the detrimental effects of scouring in similar water flow conditions.

6 Conclusions and Future Recommendations

The current study presents the impact of downward seepage to investigate how various shapes of spur dikes, permeability and orientation influence scouring processes, with the ultimate goal of identifying the most efficient spur dike designs and alignment from many potential options. Important conclusions regarding hydrodynamics interaction with varying downward seepage around the spur dikes are given below:

6.1 Experimental Study on the Optimal Spur Dike Shape under Downward Seepage

- T-shaped spur dikes deflect water smoothly, reducing turbulence, while L-shaped dikes provide gradual flow transition, and rectangular-shaped dikes create significant turbulence.
- Seepage significantly affects channel morphology, amplifying sediment transport and deepening scour depth.
- Seepage intensifies scouring around all shapes of spur dikes, with rectangular-shaped dikes experiencing the largest impact.
- T-shaped spur dikes consistently exhibit the least scour depth, with or without seepage.
- Maximum velocity is observed around rectangular-shaped dikes at the water surface, while weaker velocity is near T-shaped dikes, increasing with seepage rate.
- Reynolds shear stress increases due to spur dikes, with seepage amplifying flow disruption and generating flow reversal patterns.

6.2 Channel Morphology with Permeable Spur Dikes under Downward Seepage

- The permeability of spur dikes significantly impacts bed morphology and flow patterns, with porous structures allowing smoother flow and reducing disturbance.
- Permeability reduces mass and momentum exchange, thereby decreasing turbulence and enhancing the stability and hydraulic performance of spur dikes.

- At the base of the spur dike near the channel bed, downward seepage intensifies flow interactions, leading to stronger reversal flows, the formation of horseshoe vortices, and particle detachment.
- Higher seepage rates increase scouring by making sediment particles more detachable, creating deeper scour depressions and altering riverbed morphology.
- These findings highlight that seepage consistently increases scour depth, while permeability can significantly influence both the location and magnitude of scour.
- Impermeable spur dikes are more prone to local scouring, while permeable configurations are more effective at minimizing scour depth and turbulence.
- Implementing permeable spur dikes can be a strategic approach to reducing scouring and improving the overall stability of the structures.

6.3 Optimal spur dike orientation for scour mitigation under downward seepage conditions

- The research indicates that a 60º orientation causes notable flow deflection, as the sharp angle intensifies turbulence and generates horseshoe vortices. This leads to significant scouring.
- In contrast, a 90º orientation creates maximum obstruction, resulting in strong horseshoe vortices and a large stagnation zone with high upstream pressure. This leads to the deepest, symmetrical scour holes around the dike base due to intense turbulent flow.
- A 120º orientation enables smoother, streamlined flow with minimal separation, producing weaker horseshoe vortices and reduced turbulence. The lower pressure difference between upstream and downstream results in minimal scour depth, effectively reducing scouring.

- Altering orientation angle impacts scour depth, with 90° orientation resulting in maximum depth and 120° producing the least.
- Downward seepage increases sediment particle detachment, leading to deeper scour depressions.

6.4 Recommendations for Future Research

Despite several research studies that have been conducted to understand the flow behaviour around a spur dike, many challenges remain for future research:

- More precise knowledge of scouring around a spur dike and its impact on river bank stability is required to analyze for river bank stabilization.
- The study of flow modification in the presence of spur dike under the influence of vegetation is still unexplored. The effect of this factor on the hydro-morphology around spur dikes needs to be studied to achieve better stability and performance of spur dikes in the field.
- Investigating the effects of upward seepage near spur dikes on sediment transport, critical velocity, and turbulence is critical. Understanding these interactions can enhance predictive models and lead to more efficient designs of hydraulic structures, especially in regions where seepage effects are significant.
- Many studies focus on uniform sand when examining the scour depth and turbulent characteristics near spur dike. Still, future research should include non-uniform sediment sizes to better match field conditions.
- Investigating the relative performance of permeable and impermeable spurs in mitigating riverbank erosion is a valuable area for future research. This comparison can help identify the best design for effective erosion control.
- To better understand field conditions and ensure reliable results, more variations in discharge, seepage, spur length, spacing, and sediment size need to be considered.

References

Ahmad, M. (1951). Spacing and protection of spurs for bank protection. *Civil Engineering and Publication Review*, *46*, 3-7.

Akbar, Z., Pasha, G. A., Tanaka, N., Ghani, U., & Hamidifar, H. (2024). Reducing bed scour in meandering channel bends using spur dikes. *International Journal of Sediment Research*, *39*(2), 243-256.

Akbari, M., Vaghefi, M., & Chiew, Y. M. (2021). Effect of T-shaped spur dike length on mean flow characteristics along a 180-degree sharp bend. *Journal of Hydrology and Hydromechanics*, *69*(1), 98-107.. https://doi.org/10.2478/johh-2020-0045.

Alvarez, J. A. M., (1989). Design of groins and spur dikes. In *Proceedings of the 1989 National Conference on Hydraulic Engineering* (pp. 296-301).

Alauddin, M., & Tsujimoto, T. (2012). Optimum configuration of groynes for stabilization of alluvial rivers with fine sediments. *International Journal of Sediment Research*, *27*(2), 158-167. https://doi.org/10.1016/S1001-6279(12)60024-9.

Alvarez, J. M. (1989). State-of-the-art report: Mexico. Design of groins and spur dikes.

Ardiclioglu, M., & Ozturk, O. (2006). Numerical and experimental determination of boundarylayer thickness. *WSEAS Transactions on Systems*, *5*(5), 1186-1189.

Arora, S., Lade, A. D., & Kumar, B. (2023). Higher-order turbulence statistics and multiscale characterization of morphodynamics in a riverbank section with an upstream mining pit. *Physics of Fluids*, *35*(6).

Atarodi, A., Karami, H., Ardeshir, A., Hosseini, K., & Lampert, D. (2021). Experimental investigation of scour reduction around spur dikes by collar using Taguchi method. *Iranian Journal of Science and Technology, Transactions of Civil Engineering*, *45*, 971-983. https://doi.org/10.1007/s40996-020-00373-1.

Attia, K., & Elsaid, G. (2006). The hydraulic performance of oriented spur dike implementation in open channel. In *Journal of International Water Technology Conference, IWTC, Alexandria, Egypt* (No. 10, pp. 281-298).

Aung, H., Onorati, B., Oliveto, G., & Yu, G. (2023). Riverbed morphologies induced by local scour processes at single spur dike and spur dikes in cascade. *Water*, *15*(9), 1746.

Baba, Y., Camenen, B., Peltier, P., Thollet, F., & Zhang, H. (2010, September). Flows and bedload dynamics around spur dyke in a compound channel. In *11th International Symposium on River Sedimentation (ISRS)* (pp. 11-p).

Bahrami-Yarahmadi, M., Pagliara, S., Yabarehpour, E., & Najafi, N. (2020). Study of scour and flow patterns around triangular-shaped spur dikes. *KSCE Journal of Civil Engineering*, *24*(11), 3279-3288. https://doi.org/10.1007/s12205-020-2261-x.

Barman, K., Roy, S., Das, V. K., & Debnath, K. (2019). Effect of clay fraction on turbulence characteristics of flow near an eroded bank. *Journal of hydrology*, *571*, 87-102. https://doi.org/10.1016/j.jhydrol.2019.01.061.

Berenbrock, C. (1999). *Streamflow gains and losses in the lower Boise River basin, Idaho, 1996-97* (No. 99-4105). US Geological Survey.

Blanckaert, K., Duarte, A., Chen, Q., & Schleiss, A. J. (2012). Flow processes near smooth and rough (concave) outer banks in curved open channels. *Journal of Geophysical Research: Earth Surface*, *117*(F4). https://doi.org/10.1029/2012JF002414.

Brown, S. A. (1985). *Design of spur-type streambank stabilization structures* (No. FHWA-RD-84-101). United States. Department of Transportation. Federal Highway Administration. https://rosap.ntl.bts.gov/view/dot/25321/dot_25321_DS1.pdf

Cao, D., & Chiew, Y. M. (2014). Suction effects on sediment transport in closed-conduit flows. *Journal of Hydraulic Engineering*, *140*(5), 04014008. https://doi.org/10.1061/(ASCE)HY.1943-7900.0000833

Chabert, J. (1956). Etude des affouillements autour des piles de ponts. *Rep. Natl. Hydraul Lab., Chatou*.

Chavan, R., Kumar, B., 2017. Experimental investigation on flow and scour characteristics around tandem piers in sandy channel with downward seepage. *Journal of Marine Science and Application*, *16*(313-322). https://doi:10.1007/s11804-017-1426-6

Chavan, R., & Kumar, B. (2020). Downward seepage effects on dynamics of scour depth and migrating dune-like bedforms at tandem piers. *Canadian Journal of Civil Engineering*, *47*(1), 13-24. https://doi.org/10.1139/cjce-2017-0640

Chen, Z., Jiang, C., & Nepf, H. (2013). Flow adjustment at the leading edge of a submerged aquatic canopy. *Water Resources Research*, *49*(9), 5537-5551.

Chen, Y., Lu, Y., Yang, S., Mao, J., Gong, Y., Muhammad, W. I., & Yin, S. (2022). Numerical investigation of flow structure and turbulence characteristic around a spur dike using large-eddy simulation. *Water*, *14*(19), 3158. https://doi.org/10.3390/w14193158.

Cheng, N. S., & Chiew, Y. M. (1999). Incipient sediment motion with upward seepage. *Journal of Hydraulic Research*, *37*(5), 665-681.

Chu-Agor, M. L., Fox, G. A., & Wilson, G. V. (2009). Empirical sediment transport function predicting seepage erosion undercutting for cohesive bank failure prediction. *Journal of hydrology*, *377*(1-2), 155-164. https://doi.org/10.1016/j.jhydrol.2009.08.020.

Daneshfaraz, R., Norouzi, R., Abbaszadeh, H., Kuriqi, A., & Di Francesco, S. (2022). Influence of sill on the hydraulic regime in sluice gates: an experimental and numerical analysis. *Fluids*, *7*(7), 244.

Darby, S. E., & Thorne, C. R. (1996). Development and testing of riverbank-stability analysis. *Journal of hydraulic engineering*, *122*(8), 443-454.

Dawood, A. M. (2013). A study of Scour and Deposition around Groynes. *unpublished M. Sc. Thesis, Civil Department, Faculty of Engineering, University of Kufa, Iraq*.

Dehghani, A. A., Azamathulla, H. M., Najafi, S. H., & Ayyoubzadeh, S. A. (2013). Local scouring around L-head groynes. *Journal of hydrology*, *504*, 125-131. https://doi: 10.1016/j.jhydrol.2013.09.020

Deshpande, V., & Kumar, B. (2017). Effect of downward seepage on the shape of an alluvial channel. In *Proceedings of the Institution of Civil Engineers-Water Management* (Vol. 170, No. 1, pp. 3-14). Thomas Telford Ltd.

Devi, T.B., Sharma, A., Kumar, B. (2016). Turbulence characteristics of vegetated channel with downward seepage. *Journal of Fluids Engineering*, *138*(12), 121102. https://doi. org/ 10. 1115/1. 40338 14 (2016).

Devi, T. B., & Kumar, B. (2016). Channel hydrodynamics of submerged, flexible vegetation with seepage. *Journal of Hydraulic Engineering*, *142*(11), 04016053.https://doi. org/ 10. 1061/ (ASCE) HY. 1943- 7900. 00011 80 (2016).

Dey, S., & Raikar, R. V. (2005). Scour in long contractions. *Journal of Hydraulic Engineering*, *131*(12), 1036-1049.

Dey, S., Sarkar, S., & Ballio, F. (2011). Double-averaging turbulence characteristics in seeping rough-bed streams. *Journal of Geophysical Research: Earth Surface*, *116*(F3). https://doi.org/10.1029/2010JF001832

Dingorkar, N. A., Kulkarni, D., & Hirave, P. (2017). Study of river training work on permeable groynes. *International Journal of Civil Engineering and Technology*, *8*(6), 262-270.

Duan, J. G. (2009). Mean flow and turbulence around a laboratory spur dike. *Journal of Hydraulic Engineering*, *135*(10), 803-811. https://doi.org/10.1061/ASCEHY.1943-7900.0000077.

Duan, J., He, L., Wang, G. & Fu, X. (2011). Turbulent burst around experimental spur dike. *International Journal of Sediment Research*, *26*(4), 471-523. https://doi.org/10.1016/S1001-6279(12)60006-7.

Elawady, E., Michiue, M., & Hinokidani, O. (2001). Movable bed scour around submerged spur-dikes. *Proceedings of Hydraulic Engineering*, *45*, 373-378.

El-Rashedy, S. F., Ezzeldin, M. M., & Sarhan, T. A. (2018). Influence of spur dikes shapes on scour characteristics. *International Journal of Scientific & Engineering Research*, *9*(6), 1285-1301.

Elsaiad, A. A., & Elnikhely, E. A. (2016). Exploration of scour characteristics around spur dike in a straight wide channel. *International Water Technology Journal, IWTJ*, *6*(2), 130-143.

Engel, F. L., & Rhoads, B. L. (2017). Velocity profiles and the structure of turbulence at the outer bank of a compound meander bend. *Geomorphology*, *295*, 191-201. https://doi.org/10.1016/j.geomorph.2017.06.018.

Esmaeli, P., Boudaghpour, S., Rostami, M., & Mirzaee, M. (2022). Experimental investigation of permeability and length of a series of spur dikes effects on the control of bank erosion in the meandering channel. *Ain Shams Engineering Journal*, *13*(4), 101701. https://doi.org/ https://doi.org/10.1016/j.asej.2022.101701.

Ettema, R. (1980). Scour at bridge piers.

Ezzeldin, R. M. (2019). Numerical and experimental investigation for the effect of permeability of spur dikes on local scour. *Journal of Hydroinformatics*, *21*(2), 335-342.

Ezzeldin, M. M., Saafan, T. A., Rageh, O. S., Nejm, L. M., & Assistant, T. (2007, March). Local scour around spur dikes. In *Eleventh International Water Technology Conference, IWTC11. Sharm El-Sheikh* (pp. 779-795).

Farshad, R., Kashefipour, S. M., Ghomeshi, M., & Oliveto, G. (2022). Temporal scour variations at permeable and angled spur dikes under steady and unsteady flows. *Water*, *14*(20), 3310. https://doi.org/10.3390/w14203310.

Faruque, M. A. A., & Balachandar, R. (2011). Seepage effects on turbulence characteristics in an open channel flow. *Canadian Journal of Civil Engineering*, *38*(7), 785-799. https://doi.org/10.1139/l11-04

Fei-Yong, C., & Syunsuke, I. (1997). Horizontal separation flows in shallow open channels with spur dikes. *Journal of Hydroscience and hydraulic Engineering*, *15*(2), 15-30.

Fenwick, G. B. (1969). State of knowledge of channel stahilization in major alluvial rivers. US Corps of Eng. Comm. on Channel stabilization. *Techn. report*, (7).

Fipps, G. (2000). Potential water savings in irrigated agriculture for the Rio Grande Planning Region (Region M). *Texas Cooperative Extension, Texas A&M University System*.

Francalanci, S., Parker, G., & Solari, L. (2008). Effect of seepage-induced nonhydrostatic pressure distribution on bed-load transport and bed morphodynamics. *Journal of Hydraulic Engineering*, *134*(4), 378-389.

Fuladipanah, M., Azamathulla, H. M., Tota-Maharaj, K., Mandala, V., & Chadee, A. (2023). Precise forecasting of scour depth downstream of flip bucket spillway through data-driven models. *Results in Engineering*, *20*, 101604.

Gao, Y., Yang, H., Wang, L., & Zhao, M. (2022). Three-dimensional numerical investigation on flow behaviors around a diversion dike. *Physics of Fluids*, *34*(12).

Garde, R. J., Subramanya, K., & Nambudripad, K. D. (1961). Study of scour around spur-dikes. *Journal of the Hydraulics Division*, *87*(6), 23-37.

Garg, S. P., Singhal, M. K., & Jain, S. K. (1980). Training of rivers. In *Proceedings of the International Workshop on Alluvial River Problems Held at Roorkee*.

Gholami, V. & Khaleghi, M. R. (2013). The impact of vegetation on the bank erosion (case study: the Haraz river). *Soil and Water Research 8* (4), 158–164. https://doi.org/10.17221/13/2012-swr.

Giri, S., Shimizu, Y., & Surajate, B. (2004). Laboratory measurement and numerical simulation of flow and turbulence in a meandering-like flume with spurs. *Flow Measurement and Instrumentation*, *15*(5-6), 301-309. https://doi.org/10.1016/j.flowmeasinst.2004.05.002.

Gisonni, C., & Hager, W. H. (2008). Spur failure in river engineering. *Journal of hydraulic engineering*, *134*(2), 135-145.

Goring, D. G., & Nikora, V. I. (2002). Despiking acoustic Doppler velocimeter data. *Journal of hydraulic engineering*, *128*(1), 117-126. https:// doi. org/ 10.1061/ (ASCE) 0733-9429(2002) 128: 1(117) (2002).

Gu ZuPeng, G. Z., Akahori, R., & Ikeda, S. (2011). Study on the transport of suspended sediment in an open channel flow with permeable spur dikes. *International Journal of Sediment Research*, *26*(1), 96-111.

Haider, R., Qiao, D., Yan, J., Ning, D., Pasha, G. A., & Iqbal, S. (2022a). Flow characteristics around permeable spur dike with different staggered pores at varying angles. *Arabian Journal for Science and Engineering*, *47*(4), 5219-5236.

Haider, R., Qiao, D., Wang, X., Yan, J., & Ning, D. (2022b). Role of grouped piles on flow characteristics around impermeable spur dike. *International Journal of Civil Engineering*, *20*(8), 869-883. https://doi.org/10.1007/s40999-022-00706-3.

Hajibehzad, M. S., Bejestan, M. S. & Ferro, V. (2020). Investigating the performance of enhanced permeable groins in series. *Water*, *12*(12), 3531. https://doi.org/10.3390/w12123531.

Hakim, M., Yarahmadi, M. B., & Kashefipour, S. M. (2022). Use of spur dikes with different permeability levels for protecting bridge abutment against local scour under unsteady flow conditions. *Canadian Journal of Civil Engineering*, *49*(12), 1842-1854. https://doi.org/10.1139/cjce-2021- 0476.

Hasan, M. Z., & Toda, Y. (2024). Enhancing Riverbank Protection along the Jamuna River, Bangladesh: Review of Previous Countermeasures and Morphological Assessment through Groyne-Based Solutions Using Numerical Modeling. *Water*, *16*(2), 297.

HASHEMI, N. S., AYOUBZADEH, S. A., & DEHGHANI, A. A. (2008). Experimental investigation of scour depth around L-head groynes under clear water condition.

Ho, J., Yeo, H. K., Coonrod, J., & Ahn, W. (2007). Numerical modeling study for flow pattern changes induced by single groyne. In *Proceedings of the Congress-International Association for Hydraulic Research* (Vol. 32, No. 2, p. 662).

Hu, J., Wang, G., Wang, P., Yu, T., & Chen, H. (2022). Experimental study on the influence of new permeable spur dikes on local scour of navigation channel. *Sustainability*, *15*(1), 570.

Indulekha, K. P., Jayasree, P. K., & Sachin, S. (2021, March). Simulation of flow pattern around series of groynes with different orientations in meandering channels. In *IOP Conference Series: Materials Science and Engineering* (Vol. 1114, No. 1, p. 012024). IOP Publishing. https://doi.org/10.1088/1757-899x/ 1114/1/012024.

Iqbal, S., Pasha, G. A., Ghani, U., Ullah, M. K., & Ahmed, A. (2021). Flow dynamics around permeable spur dike in a rectangular channel. *Arabian Journal for Science and Engineering*, *46*(5), 4999-5011.

Jafari, R., & Sui, J. (2021). Velocity field and turbulence structure around spur dikes with different angles of orientation under ice covered flow conditions. *Water*, *13*(13), 1844. https://doi.org/10.3390/w13131844.

Jahan M. (2014). Effect of suction on local scour around circular bridge piers [MSc dissertation], Department of Civil and Environmental Engineering, University of Windsor. https://scholar.uwindsor.ca/etd/5136/

Jeon, J., Lee, J. Y., & Kang, S. (2018). Experimental investigation of three-dimensional flow structure and turbulent flow mechanisms around a nonsubmerged spur dike with a low length-to-depth ratio. *Water Resources Research, 54*(5), 3530-3556. https://doi.org/10.1029/ 2017WR021582.

Ji1a, H. J. S. & Karmacharya, B. (2000). Flood Control Measures Best Practices Report an Approach for Community-Based Flood Control Measures in the Terai River. German Technical Cooperation, Kathmandu, Nepal.

Kadota, A., Suzuki, K., & Kojima, E. (2010). Flow visualization of mean and coherent flow structures around T-type and L-type groynes. In *River Flow* (Vol. 2010, pp. 203-210). https://hdl.handle.net/20.500.11970/99647

Kafle, M. R. (2021). Numerical simulation of flow pattern in series of impermeable groynes in fixed bed. *Journal of Advanced College of Engineering and Management, 6*, 83-88.

Kang, S. (2018). Large-eddy simulation study of turbulent flow around a rectangular spur dike. In *E3S web of conferences* (Vol. 40, pp. 1-8). EDP Sciences. https:// doi.org/10.1051/e3sconf/20184005013.

Kang, S., & Sotiropoulos, F. (2011). Flow phenomena and mechanisms in a field-scale experimental meandering channel with a pool-riffle sequence: Insights gained via numerical simulation. *Journal of Geophysical Research: Earth Surface*, *116*(F3). https://doi.org/ 10.1029/2010JF001814.

Kang, S., Khosronejad, A., Hill, C., & Sotiropoulos, F. (2021). Mean flow and turbulence characteristics around single-arm instream structures. *Journal of Hydraulic Research*, *59*(3), 404-419. https://doi.org/10.1080/00221686.2020.1780494.

Kang, S., Khosronejad, A., & Yang, X. (2021). Turbulent flow characteristics around a non-submerged rectangular obstacle on the side of an open channel. *Physics of Fluids*, *33*(4). https://doi.org/10.1063/5.0042914.

Kanungo, K. (1956). Central Board of Irrigation and Power" Symposium on Determination of Costs and Benefits of River Valley Projects, 1953"(Book Review). *Indian Journal of Agricultural Economics*, *11*(1), 101.

Khajavi, M., Kashefipour, S. M., & Bejestan, M. S. (2022). Bridge abutment protection against scouring for unsteady flow conditions. *Periodica Polytechnica Civil Engineering*, *66*(1), 310-322. https://doi.org/10.3311/PPci.18892.

Kim, S. J., Kang, J. G., & Yeo, H. K. (2014). An experimental study on flow characteristics for optimal spacing suggestion of 45 upward groynes. *Journal of Korea Water Resources Association*, *47*(5), 459-468.

King, H. (2009). *The use of groynes for riverbank erosion protection*.

Kinzli, K. D., Martinez, M., Oad, R., Prior, A., & Gensler, D. (2010). Using an ADCP to determine canal seepage loss in an irrigation district. *Agricultural water management*, *97*(6), 801-810.

Kirkgöz, M. S., & Ardiçlioğlu, M. (1997). Velocity profiles of developing and developed open channel flow. *Journal of hydraulic engineering*, *123*(12), 1099-1105.

Koken, M. (2011). Coherent structures around isolated spur dikes at various approach flow angles. *Journal of Hydraulic Research*, *49*(6), 736-743.

Koken, M., & Gogus, M. (2015). Effect of spur dike length on the horseshoe vortex system and the bed shear stress distribution. *Journal of Hydraulic Research*, *53*(2), 196-206. https://doi.org/10.1080/00221686.2014.967819.

Krishna Prasad, S., Indulekha, K. P. & Balan, K. (2016). Analysis of groyne placement on minimising river bank erosion. *Procedia Technology 24* (47–53). https://doi.org/10.1016/j.protcy.2016.05.008.

Kuhnle, R. A., Alonso, C. V., & Shields Jr, F. D. (2002). Local scour associated with angled spur dikes. *Journal of Hydraulic Engineering*, *128*(12), 1087-1093.

Kuhnle, R. A., Jia, Y., & Alonso, C. V. (2008). Measured and simulated flow near a submerged spur dike. *Journal of Hydraulic Engineering*, *134*(7), 916-924. https://doi.org/10.1061/(asce)0733-9429(2008)134:7(916).

Kumar, A., & Ojha, C. S. P. (2019). Effect of different compositions in unsubmerged L-head groynes to mean and turbulent flow characteristics. *KSCE Journal of Civil Engineering*, *23*(10), 4327-4338. https://doi.org/10.1007/s12205-019-5343-x.

Kumar, A., & Ojha, C. S. P. (2021). Near-bed turbulence around an unsubmerged L-head groyne. *ISH Journal of Hydraulic Engineering*, *27*(sup1), 182-189. https://doi.org/10.1080/09715010.2019.1609380.

Das, V. K., Barman, K., Roy, S., Chaudhuri, S., & Debnath, K. (2020). Near bank turbulence of a river bend with self similar morphological structures. *Catena*, *191*, 104582. https://doi.org/10.1016/j.catena.2020.104582.

Langhoff, J. H., Rasmussen, K. R., & Christensen, S. (2006). Quantification and regionalization of groundwater–surface water interaction along an alluvial stream. *Journal of Hydrology*, *320*(3-4), 342-358

Launder, B. E., & Sharma, B. I. (1974). Application of the energy-dissipation model of turbulence to the calculation of flow near a spinning disc. *Letters in heat and mass transfer*, *1*(2), 131-137. https://doi.org/10.1016/0094-4548(74)90150-7.

Launder, B. E., & Spalding, D. B. (1983). The numerical computation of turbulent flows. In *Numerical prediction of flow, heat transfer, turbulence and combustion* (pp. 96-116). Pergamon. https://doi.org/10.1016/b978-0-08-030937-8.50016-7.

Li, Y., & Altinakar, M. (2016, May). Effects of a Permeable Hydraulic Flashboard Spur Dike on Scour and Deposition. In *World Environmental and Water Resources Congress 2016* (pp. 399-409).

Liu, X. X., & Chiew, Y. M. (2012). Effect of seepage on initiation of cohesionless sediment transport. *Acta Geophysica*, *60*, 1778-1796. https:// doi. org/ 10. 2478/ s11600- 012-0043-7 (2012).

Lu, Y., Chiew, Y. M., & Cheng, N. S. (2008). Review of seepage effects on turbulent open-channel flow and sediment entrainment. *Journal of Hydraulic Research*, *46*(4), 476-488. https:// doi. org/ 10. 3826/ jhr. 2008. 2942 (2008).

Lodhi, A. S., Jain, R. K., & Sharma, P. K. (2021, February). Flow behaviour around spur dyke founded in cohesive sediment mixtures. In *Proceedings of the Institution of Civil Engineers-Water Management* (Vol. 174, No. 1, pp. 1-14). Thomas Telford Ltd. https://doi.org/10.1680/jwama.19.00022.

Mamak, W. (1964). River regulation (Vol. 61, No. 31301). Arkady, Poland; 1964; 415 pp.

Marsh, N. A., Western, A. W., & Grayson, R. B. (2004). Comparison of methods for predicting incipient motion for sand beds. *Journal of hydraulic engineering*, *130*(7), 616-621.

Martin, C. A., & Gates, T. K. (2014). Uncertainty of canal seepage losses estimated using flowing water balance with acoustic Doppler devices. *Journal of Hydrology*, *517*, 746-761.

Masjedi, A., Bejestan, M. S., & Rahnavard, P. (2010). Reduction of local scour at single T-shape spur dike with wing shape in a 180 degree flume bend. *World Applied Sciences Journal*, *8*(9), 1122-1128.

Masjedi, A., Akbari, I., & Abyar, H. (2011). Evaluating scour at L-shape spur dike in a 180 degree bend. *World Applied Sciences Journal*, *15*(12), 1740-1745.

Mehraein, M., & Ghodsian, M. (2017). Experimental study on relation between scour and complex 3D flow field. *Scientia Iranica*, *24*(6), 2696-2711. https://doi.org/10.24200/sci.2017.4165.

Mehraein, M., Ghodsian, M., Khosravi Mashizi, M., & Vaghefi, M. (2017). Experimental study on flow pattern and scour hole dimensions around a T-shaped spur dike in a channel bend under emerged and submerged conditions. *International Journal of Civil Engineering*, *15*, 1019-1034. https://doi.org/10.1007/s40999-017-0175-x.

Mehta, D. J., & Yadav, S. M. (2020). Analysis of scour depth in the case of parallel bridges using HEC-RAS. *Water Supply*, *20*(8), 3419-3432.

Mioduszewski, T., Maeno, S., & Uema, Y. (2003). Influence of the spur dike permeability on flow and scouring during a surge pass. In *International Conf. on Estuaries and Coasts, Hangshou, China* (pp. 380-388).

Mirzaei, H., Asadi, M., Tootoonchi, H., & Ramezani, A. (2021). Numerical simulation of secondary flow around the open and close groins in channel with movable bed. *Modeling Earth Systems and Environment*, 1-12. https://doi.org/10.1007/s40808-021-01331-0.

Mohammadpour, R., Ghani, A. A., Vakili, M., & Sabzevari, T. (2016). Prediction of temporal scour hazard at bridge abutment. *Natural Hazards*, *80*, 1891-1911. https://doi:10.1007/s11069-015-2044-8

Mojtahedi, A., & Basmenji, A. B. (2017). Numerical and field investigation of the impacts of the bank protection projects on the fluvial hydrodynamics (case study: Ghezel Ozan River). *International Journal of Engineering and Technology*, *9*(6), 492. https://doi:10.7763/IJET.2017.V9.1022

Molinas, A., Kheireldin, K., & Wu, B. (1998). Shear stress around vertical wall abutments. *Journal of Hydraulic Engineering*, *124*(8), 822-830.

Mulahasan, S., Al-Osmy, S., & Alhashimi, S. (2021, March). Modelling of flow pattern in an open channel with sidewall obstruction. In *IOP Conference Series: Materials Science and Engineering* (Vol. 1090, No. 1, p. 012097). IOP Publishing. https://doi.org/10.1088/1757-899x/1090/1/012097.

Naranjo, R., Smith, D., & Lindenbach, E. (2023). Incorporating temperature into seepage loss estimates for a large unlined irrigation canal. *Journal of Hydrology*, *617*, 129117. https://doi: 10.1016/j.jhydrol.2023.129117

Nasrollahi, A., Ghodsian, M., Neyshabour, SAAS. (2008). Local scour at permeable spur dikes. *Journal of Applied Sciences 8*(19):3398–406.

Nath, D., & Misra, U. K. (2017). Experimental study of local scour around single spur dike in an open channel. *International Research Journal of Engineering and Technology*, *4*(6), 2728-2734.

Nayyer, S., Farzin, S., Karami, H., & Rostami, M. (2019). A numerical and experimental investigation of the effects of combination of spur dikes in series on a flow field. *Journal of the Brazilian Society of Mechanical Sciences and Engineering*, *41*(6), 256. https://doi:10.1007/s40430-019-1757-0

Niles, J. M., & Hartman, K. J. (2011). Temporal distribution and taxonomic composition differences of larval fish in a large navigable river: a comparison of artificial dike structures and natural habitat. *River Research and Applications*, *27*(1), 23-32.

Norouzi, R., Ebadzadeh, P., Sume, V., & Daneshfaraz, R. (2023). Upstream vortices of a sluice gate: An experimental and numerical study. *AQUA—Water Infrastructure, Ecosystems and Society*, *72*(10), 1906-1919.

Oliveto, G., & Hager, W. H. (2002). Temporal evolution of clear-water pier and abutment scour. *Journal of Hydraulic Engineering*, *128*(9), 811-820.

Oliveto, G., & Hager, W. H. (2005). Further results to time-dependent local scour at bridge elements. *Journal of Hydraulic Engineering*, *131*(2), 97-105.

Osman, M. A., & Saeed, H. N. (2012). Local scour depth at the nose of permeable and impermeable spur dykes. *University Of Khartoum Engineering Journal*, *2*(1).

Ouillon, S., & Dartus, D. (1997). Three-dimensional computation of flow around groyne. *Journal of hydraulic Engineering*, *123*(11), 962-970.

Pandey, M., Ahmad, Z., & Sharma, P. K. (2016). Estimation of maximum scour depth near a spur dike. *Canadian Journal of Civil Engineering*, *43*(3), 270-278. https://doi.org/10.1139/cjce-2015-0280

Pandey, M., Ahmad, Z., & Sharma, P. K. (2018). Scour around impermeable spur dikes: a review. *ISH journal of hydraulic engineering*, *24*(1), 25-44. https://doi.org/10.1080/09715010.2017.1342571

Pandey, M., Lam, W. H., Cui, Y., Khan, M. A., Singh, U. K., & Ahmad, Z. (2019). Scour around spur dike in sand–gravel mixture bed. *Water*, *11*(7), 1417. https://doi.org/10.3390/w11071417.

Pandey, M., Jamei, M., Karbasi, M., Ahmadianfar, I., & Chu, X. (2021a). Prediction of maximum scour depth near spur dikes in uniform bed sediment using stacked generalization ensemble tree-based frameworks. *Journal of Irrigation and Drainage Engineering*, *147*(11), 04021050.

Pandey, M., Valyrakis, M., Qi, M., Sharma, A., & Lodhi, A. S. (2021b). Experimental assessment and prediction of temporal scour depth around a spur dike. *International Journal of Sediment Research*, *36*(1), 17-28. https://doi.org/10.1016/j.ijsrc.2020.03.015

Pandey, M., Jamei, M., Ahmadianfar, I., Karbasi, M., Lodhi, A. S., & Chu, X. (2022). Assessment of scouring around spur dike in cohesive sediment mixtures: A comparative study on three rigorous machine learning models. *Journal of Hydrology*, *606*, 127330.

Pandey, M. (2014). Flow pattern and scour around multiple spur-dikes in channels. *M. Tech Thesis*., Department of Civil Engineering, IIT Roorkee, Roorkee, India.

Patel, H. K., Arora, S., Lade, A. D., Kumar, B., & Azamathulla, H. M. (2023a). Flow behaviour concerning bank stability in the presence of spur dike–A review. *Water Supply*, *23*(1), 237-258. https://doi.org/10.2166/ws.2022.418

Patel, H. K., & Kumar, B. (2023). Hydro-morphological behavior around T-shaped spur dikes with downward seepage. *Scientific Reports*, *13*(1), 10454. https://doi.org/10.1038/s41598-023-37694-w

Patel, H. K., & Kumar, B. (2024). Experimental study on the optimal spur dike shape under downward seepage. *Water Science*, *38*(1), 172-191.

Patel, H. K., Arora, S., Chavan, R., & Kumar, B. (2023b). Migrating scour depth around a spur dike with downward seepage using multiscale characterizations. Experimental Thermal and Fluid Science, 151, 111071. https://doi.org/10.1016/j.expthermflusci.2023.111071

Pourshahbaz, H., Abbasi, S., Pandey, M., Pu, J. H., Taghvaei, P., & Tofangdar, N. (2022). Morphology and hydrodynamics numerical simulation around groynes. *ISH Journal of Hydraulic Engineering*, *28*(1), 53-61.

Prinos, P. (1995). Bed-suction effects on structure of turbulent open-channel flow. *Journal of Hydraulic Engineering*, *121*(5), 404-412. https://doi:10.1061/(ASCE)0733-9429(1995)121:5(404)

Qi, M., Chiew, Y. M., & Hong, J. H. (2013). Suction effects on bridge pier scour under clear-water conditions. *Journal of Hydraulic Engineering*, *139*(6), 621-629.

Rahman, M., & Muramoto, Y. (1999). Prediction of maximum scour depth around spur-dike-like structures. *Proceedings of Hydraulic Engineering*, *43*, 623-628. https://doi:10.2208/prohe.43.623

Rao, A. R., Sreenivasulu, G., & Kumar, B. (2011). Geometry of sand-bed channels with seepage. *Geomorphology*, *128*(3-4), 171-177. https:// doi. org/ 10. 1016/j. geomorph. 2011. 01. 003 (2011).

Richardson, E. V., & Simons, D. B. (1984). Use of spurs and guidebanks for highway crossings. *Transportation Research Record Vol. 950*, (2), 184-193.

Richardson, E. V., Stevens, M. A., & Simons, D. B. (1975). The design of spurs for river training. In *XVIth, IAHR congress* (pp. 382-388).

Roushangar, K., Goodarzi, S., & Abbaszadeh, H. (2024). Numerical investigation of the performance of blade groynes on scouring and its effect on hydraulic parameters of sediment and flow. *Environment and Water Engineering*, *10*(1), 121-136.

Roy, S., Das, V. K., & Debnath, K. (2019). Characteristics of intermittent turbulent structures for river bank undercut depth increment. *Catena*, *172*, 356-368. https://doi.org/10.1016/j.catena.2018.09.008.

Safarzadeh, A., Salehi Neyshabouri, S. A. A., & Zarrati, A. R. (2016). Experimental investigation on 3D turbulent flow around straight and T-shaped groynes in a flat bed channel. *Journal of Hydraulic Engineering*, *142*(8), 04016021. https://doi.org/10.1061/(asce)hy.1943-7900.0001144.

Shahabi, M., & Kashefipour, S. M. (2017). Experimental Investigation of The Effect of The Permeable Spur Dikes on Scour Hole Dimensions in a Mild 90 Degree Bend. *Irrigation Sciences and Engineering*, *39*(4), 13-21.

Shampa, Hasegawa, Y., Nakagawa, H., Takebayashi, H., & Kawaike, K. (2020). Three-dimensional flow characteristics in slit-type permeable spur dike fields: efficacy in riverbank protection. *Water*, *12*(4), 964. https://doi.org/10.3390/W12040964

Sharma, H. D., & Chawla, A. S. (1975). Manual of canal lining. *Central Board of Irrigation and Power, New Delhi*.

Sharma, A., Chavan, R., & Kumar, B. (2017). Multi-scale statistical characterization of migrating pier scour depth in non-uniform sand bed channel. *International Journal of River Basin Management*, *15*(3), 265-276. https://doi.org/10.1080/15715124.2017.1298606

Sharma, A., & Kumar, B. (2018). High-order velocity moments of turbulent boundary layers in seepage affected alluvial channel. *Journal of Fluids Engineering*, *140*(8), 081204. https://doi:10.1115/1.4039253

Sharma, A., Kumar, B., & Balachandar, R. (2020). Comparison of flow and morphological characteristics in uniform and non-uniform sand bed channel. *Canadian Journal of Civil Engineering*, *47*(6), 678-690. https:// doi. org/ 10. 1139/ cjce- 2017- 0627 (2020).

Sharma, A., Kumar, B., & Oliveto, G. (2021). Experimental study on the near-bed flow characteristics of alluvial channel with seepage. *Applied Sciences*, *11*(20), 9619.

Sreenivasulu, G., Kumar, B., & Rao, A. R. (2011). Variation of stream power with seepage in sand-bed channels. *Water SA*, *37*(1). https:// doi. org/10. 4314/ wsa. v37i1. 64115 (2011).

Stamou, A., Polydera, A., Papadonikolaki, G., Martinez-Capel, F., Muñoz-Mas, R., Papadaki, C., ... & Dimitriou, E. (2018). Determination of environmental flows in rivers using an integrated hydrological-hydrodynamic-habitat modelling approach. *Journal of environmental management*, *209*, 273-285. https://doi.org/10.1016/j.jenvman.2017.12.038.

Stapleton, K. R., & Huntley, D. A. (1995). Seabed stress determinations using the inertial dissipation method and the turbulent kinetic energy method. *Earth surface processes and landforms*, *20*(9), 807-815.

Tanji, K. K., & Kielen, N. C. (2002). *Agricultural drainage water management in arid and semi-arid areas* (No. 61, pp. xiv+-188).

Taye, J., & Kumar, B. (2021). Experimental study on near-bed flow turbulence of sinuous channel with downward seepage. In *Proceedings of the Institution of Civil Engineers-Water Management* (Vol. 174, No. 4, pp. 173-186). Thomas Telford Ltd. https:// doi. org/ 10.1680/ jwama. 19. 00094.

Taye, J., Sharma, A., & Kumar, B. (2023). Effect of downward seepage on turbulence and morphology in mobile boundary sinuous channel. *Physics of Fluids*, *35*(1).

Thompson, C. E., Amos, C. L., Jones, T. E. R., & Chaplin, J. (2003). The manifestation of fluid-transmitted bed shear stress in a smooth annular flume-a comparison of methods. *Journal of Coastal Research*, 1094-1103.

Tison Jr, G. (1962). Discussion of "Study of Scour Around Spur-Dikes". *Journal of the Hydraulics Division*, *88*(4), 301-306.

Tripathi, R. P., & Pandey, K. K. (2021). Experimental study of local scour around T-shaped spur dike in a meandering channel. *Water Supply*, *21*(2), 542-552. https://doi.org/10.2166/ws.2020.331

Tripathi, R. P., & Pandey, K. K. (2022). Scour around spur dike in curved channel: a review. *Acta Geophysica*, *70*(5), 2469-2485. https://doi.org/10.1007/s11600-022-00795-7.

United Nations (1953). River Training and Bank Protection.

USACE (1980). Engineering and Design: Layout and Desing of Shallow-Draft Waterways.

Carr, J. E. (1990). *National water summary 1987: Hydrologic events and water supply and use* (Vol. 2350). US Government Printing Office.

Vaghefi, M., Ghodsian, M., & Salehi Neyshaboori, S. A. A. (2009). Experimental study on the effect of a T-shaped spur dike length on scour in a 90 channel bend. *Arabian Journal for Science and Engineering*, *34*(2), 337.

Vaghefi, M., Ghodsian, M., & Neyshabouri, S. A. A. S. (2012). Experimental study on scour around a T-shaped spur dike in a channel bend. *Journal of Hydraulic Engineering*, *138*(5), 471-474. https://doi.org/10.1061/(asce)hy.1943-7900.0000536.

Vaghefi, M., Ahmadi, A., & Faraji, B. (2015). The effect of support structure on flow patterns around T-shape spur dike in 90 bend channel. *Arabian Journal for Science and Engineering*, *40*, 1299-1307. https://doi.org/10.1007/s13369-015-1604-2.

Vaghefi, M., Alavinezhad, M., & Akbari, M. (2016a). The effect of submergence ratio on flow pattern around short T-head spur dike in a mild bend with rigid bed using numerical model. *Journal of the Chinese Institute of Engineers*, *39*(6), 666-674. https://doi.org/10.1080/02533839.2016.1187084.

Vaghefi, M., Safarpoor, Y., & Akbari, M. (2016). Numerical investigation of flow pattern and components of three-dimensional velocity around a submerged T-shaped spur dike in a 90 bend. *Journal of Central South University*, *23*, 2984-2998. https://doi.org/10.1007/s11771-016-3362-z.

Vaghefi, M., Faraji, B., Akbari, M., & Eghbalzadeh, A. (2018). Numerical investigation of flow pattern around a T-shaped spur dike in the vicinity of attractive and repelling protective structures. *Journal of the Brazilian Society of Mechanical Sciences and Engineering*, *40*, 1-15. https://doi.org/10.1007/s40430-017-0954-y.

Vaghefi, M., Radan, P., & Akbari, M. (2019). Flow pattern around attractive, vertical, and repelling T-shaped spur dikes in a mild bend using CFD modeling. *International Journal of Civil Engineering*, *17*, 607-617. https://doi.org/10.1007/s40999-018-0340-x.

Van Balen, W., Blanckaert, K., & Uijttewaal, W. S. (2010). Analysis of the role of turbulence in curved open-channel flow at different water depths by means of experiments, LES and RANS. *Journal of Turbulence*, (11), N12. https://doi.org/10.1080/14685241003789404.

Van der Lely, A. (1994). Coleambally Draft Land and Water Management Plan. RW 3127-s3-062. July 1994.

Wang, C., Yu, X., & Liang, F. (2017). A review of bridge scour: mechanism, estimation, monitoring and countermeasures. *Natural Hazards*, *87*, 1881-1906. https://doi.org/10.1007/s11069-017-2842-2

Wang, M., Tian, Y., & Li, X. (2022). Experimental study on pressure distribution of spur dike under the combined action of landslide surge and water flow. *AIP Advances*, *12*(7). https://doi.org/10.1063/5.0099656.

Watters, G. Z., & Rao, M. V. (1971). Hydrodynamic effects of seepage on bed particles. *Journal of the Hydraulics Division*, *97*(3), 421-439.

Yang, J., Shen, Z., Zhang, J., Teng, X., Zhang, W., & Dai, J. (2022a). Experimental and numerical investigation of flow over a spillway bend with different combinations of permeable spur dikes. *Water Supply*, *22*(2), 1557-1574. https://doi.org/10.2166/ws.2021.335.

Yang, X., Zhang, S., Li, W., Tang, C., Zhang, J., Schwindt, S., ... & Wang, T. (2022b). Impact of the construction of a dam and spur dikes on the hydraulic habitat of Megalobrama terminalis spawning sites: a case study in the Beijiang River (China). *Ecological Indicators*, *143*, 109361. https://doi.org/https://doi.org/10.1016/j.ecolind.2022.109361.

Shiming, Y., Hongyan, Y., & Ligang, L. (2012). Analysis on current situation and development trend of ecological revetment works in middle and lower reaches of Yangtze River. *Procedia Engineering*, *28*, 307-313.

Yao, W., & Rutschmann, P. (2015). Three high flow experiment releases from Glen Canyon Dam on rainbow trout and flannelmouth sucker habitat in Colorado River. *Ecological Engineering*, *75*, 278-290.

Yazdi, J., Sarkardeh, H., Azamathulla, H. M., & Ghani, A. A. (2010). 3D simulation of flow around a single spur dike with free-surface flow. *Intl. J. River Basin Management*, *8*(1), 55-62. https://doi.org/10.1080/15715121003715107.

Yi, Y., Wang, Z., & Yang, Z. (2010). Two-dimensional habitat modeling of Chinese sturgeon spawning sites. *Ecological Modelling*, *221*(5), 864-875.

Yossef, M. (2002). The Effect of Groynes on Rivers: *Literature Review*; Cluster Publicatienummer 03.03.04; Delft University of Technology: Delft, The Netherlands. http://resolver.tudelft.nl/uuid:b9545ba7-2423-4c20-ace2-0e1cd799d18a

Yussuff, S. M., Chauhan, H. S., Kumar, M., & Srivastava, V. K. (1994). Transient canal seepage to sloping aquifer. *Journal of irrigation and drainage engineering*, *120*(1), 97-109.

Yu, T., Duan, Q., Wang, P., Meng, C., & Lu, R. (2021). Experimental study on flow structure around spur dikes of different types. *Converter*, *2021*(3), 778-788.

Yu, T., Yun, B., Wang, P., & Han, L. (2022). Turbulent kinetic energy distribution around experimental permeable spur dike. *Sustainability*, *14*(10), 6250. https://doi.org/10.3390/su14106250.

Zhang, H., Nakagawa, H. (2008). Scour around spur dykes: *Recent advances and future studies*, Annuals of the Disaster Prevention Research Institute, Kyoto University, 51B:171-188.

Zhou, Y. J., Qian, S., & Sun, N. N. (2014). Application of permeable spur dike in mountain river training. *Applied Mechanics and Materials*, *641*, 236-240.

Zolghadr, M., Zomorodian, S. M. A., Fathi, A., Tripathi, R. P., Jafari, N., Mehta, D., ... & Azamathulla, H. M. (2023). Experimental study on the optimum installation depth and dimensions of roughening elements on abutment as scour countermeasures. *Fluids*, *8*(6), 175.